Freezing and melting in binary mixtures of superparamagnetic particles

Inaugural-Dissertation

zur Erlangung des Doktorgrades
der Mathematisch-Naturwissenschaftlichen Fakultät
der Heinrich-Heine-Universität Düsseldorf

vorgelegt von

Tobias Horn

aus Solingen

Düsseldorf, Januar 2015

aus dem Institut für Theoretische Physik II: Weiche Materie
der Heinrich-Heine-Universität Düsseldorf

Gedruckt mit der Genehmigung der
Mathematisch-Naturwissenschaftlichen Fakultät der
Heinrich-Heine-Universität Düsseldorf

Referent: Prof. Dr. Hartmut Löwen
Korreferent: Prof. Dr. Jürgen Horbach

Tag der mündlichen Prüfung: 09. März 2015

Contents

Summary

This thesis contains an analysis of freezing and melting processes in two-dimensional binary colloidal mixtures of superparamagnetic particles. The analysis is divided into four parts, which are constituted by independent scientific journal articles. These have been published in the years 2013 and 2014 following a peer-review process.
The first part of this work is dedicated to the study of two-dimensional melting in the presence of quenched disorder. This study is based on video-microscopy data of superparamagnetic colloidal particles and computer simulations of repulsive dipoles. Quenched disorder is introduced in this approach by pinning a fraction of the particles to an underlying substrate, by which a matrix of frozen-in obstacles is formed. The occurrence of the Kosterlitz-Thouless-Halperin-Nelson-Young (KTHNY) scenario is confirmed and an intermediate hexatic phase is observed. While the fluid-hexatic transition remains largely unaffected by disorder, the hexatic-solid transition shifts to lower temperatures with increasing disorder. This results in a significantly broadened stability range of the hexatic phase. Characteristics of first order transitions are not observed.
In the second part of this work, the formation of fluctuating orientational clusters and topological defects is studied in the context of the KTHNY-like melting scenario under quenched disorder. Statistical properties of these clusters as well as the development of defects are assessed as a function of system temperature and disorder strength. Thus, evidence is provided that the disorder-induced widening of the hexatic phase can be traced back to the distinct characteristics of clusters and defects along the melting transitions.
The third part of this work contains a review of the crystallization effects and the melting mechanism in systems with an immobilized particle species.
In the fourth part of this work, the shear-induced destabilization of an equimolar two-dimensional binary model crystal is explored. The two particle species exhibit a high interaction asymmetry such that the initial crystal has an intersecting square sublattice of the two constituents. The combination of shear and thermal fluctuations is found to induce a characteristic hierarchical breaking scenario where initially, the more strongly coupled particles are thermally distorted, paving the way for the weakly coupled particles to escape from their cages. This in turn leads to mobile defects which may finally merge, proliferating a cascade of defects, which triggers the final breakage of the crystal. This scenario is in marked contrast to the breakage of one-component crystals close to melting. These results are verifiable in real-space experiments of superparamagnetic colloidal mixtures at a pending air-water interface in an external magnetic field where the shear can be induced by an external laser field.

Zusammenfassung

Diese Dissertationsschrift enthält eine Analyse von Gefrier- und Schmelzprozessen in zweidimensionalen, binären Kolloidgemischen aus superparamagnetischen Teilchen. Die Untersuchung ist in vier Teile gegliedert, die in Form von eigenständigen wissenschaftlichen Fachartikeln vorliegen. Diese wurden nach Durchlaufen eines Peer-Review Verfahrens in den Jahren 2013 und 2014 veröffentlicht.
Der erste Teil dieser Arbeit ist der Untersuchung des zweidimensionalen Schmelzprozesses in der Gegenwart von topologischer Unordnung gewidmet. Diese Untersuchung basiert auf Videomikroskopiedaten von superparamagnetischen Kolloiden und Computersimulationen von repulsiven Dipolen. Topologische Unordnung wird durch das Haften einzelner Teilchen an einem unterliegenden Substrat hervorgerufen, wodurch ein Arrangement von eingefrorenen Hindernissen entsteht.
Das Auftreten des Kosterlitz-Thouless-Halperin-Nelson-Young (KTHNY) Szenarios wird bestätigt und eine zwischenliegende hexatische Phase beobachtet. Während der flüssig-hexatisch Phasenübergang kaum durch Unordnung beeinflusst wird, verschiebt sich der hexatisch-fest Übergang mit steigender Unordnung in Richtung tieferer Temperaturen. Dies bedingt einen deutlich verbreiterten Stabilitätsbereich der hexatischen Phase. Merkmale eines Phasenübergangs erster Ordnung werden nicht beobachtet.
Im zweiten Teil dieser Arbeit wird die Entstehung fluktuierender Orientierungscluster und topologischer Defekte vor dem Hintergrund des KTHNY Schmelzszenarios in der Gegenwart von Unordnung untersucht. Statistische Merkmale dieser Cluster sowie die Entstehung von topologischen Defekten werden in Abhängigkeit der Systemtemperatur und der Stärke der Unordnung untersucht. Somit wird der Nachweis erbracht, dass die durch Unordnung hervorgerufene Verbreiterung der hexatischen Phase auf die Eigenschaften von Orientierungsclustern und topologischen Defekten während des Schmelzprozesses zurückgeführt werden kann.
Der dritte Teil dieser Arbeit enthält einen zusammenfassenden Rückblick über die Kristallisationseffekte und den Schmelzmechanismus in Systemen mit einer eingefrorenen Teilchenspezies.
Im vierten Teil dieser Arbeit wird das Schmelzen eines äquimolaren, zweidimensionalen, binären Modellkristalls unter Scherung analysiert. Die zwei Partikelspezies weisen eine starke Asymmetrie hinsichtlich ihrer Wechselwirkung auf, so dass die Kristallstruktur anfangs zwei versetzten, quadratischen Gittern entspricht, die von den beiden Spezies gebildet werden. Die Kombination aus Scherung und thermischer Fluktuation erzeugt ein charakteristisches, hierarchiches Bruchszenario, in dem die stärker wechselwirkenden Teilchen zunächst thermisch abgelenkt werden und dadurch die Bewegung des eingeschlossenen, schwächer wechselwirkenden Teilchens fort von seinem Gitterplatz begünstigen.
Dies wiederum führt zu der Entstehung beweglicher Defekte, die sich schließlich verbinden

und eine Kaskade von Defekten hervorrufen, durch die der Kristall zu Bruch geht. Dieser Vorgang weist deutliche Unterschiede zum Bruch eines einkomponentigen Kristalls in der Nähe des Schmelzpunktes auf. Diese Ergebnisse sind verifizierbar im Rahmen von Experimenten mit superparamagnetischen kolloidalen Gemischen in einer hängenden Luft-Wasser Grenzfläche, die einem externen magnetischen Feld ausgesetzt sind. Die Scherung kann mithilfe von einem externen Laserfeld erzeugt werden.

Preface

Arguably, the most well-known instance of freezing is the solidification of water into ice upon decreasing temperature: The brittle surface of a frozen lake comes to mind or the layer of frost covering windshields on a winter's morning. Despite its ubiquity, the peculiar changes inherent in this freezing process are bound to astonish the observer. After all, the visible crystalline structure of ice, its palpable rigidity and the occasional formation of cracks in the material are in striking contrast to the apparent shapelessness and smooth elusiveness of water. It is intriguing to ask what intricate mechanism mediates the transition from the one state into the other. In fact, there is not a single mechanism governing the transformation from a liquid into a solid - or the reverse way. Instead, the broad array of settings in which such transitions may be observed entails multiple, qualitatively different freezing and melting mechanisms. Thus, the freezing of a liquid under bulk conditions is qualitatively different from freezing at a surface or in the presence of impurities. Fluidization and solidification may also be induced by mechanical conditions to which a material is subjected, and further freezing and melting mechanisms follow from that. In this preface, an account on freezing and melting processes shall be given, which have been adressed in physical studies throughout the past decades. In particular, the pivotal impact of colloid science on our current understanding of freezing and melting mechanics shall be highlighted and important cornerstones of this understanding will be portrayed. Thus, the results presented in the journal articles constituting this work will be embedded into the scope of current research.

Reflecting the different states of matter, the ancient greek philosopher Plato was lead to assume that all materials - in specific, the mystical classical elements, on which Plato focussed his considerations - are composed of polyhedrally shaped, elemental particles, which are referred to as the platonic solids [1]. Based on the geometric properties of these alleged building blocks of matter, Plato deduced a coarse explanation for the properties of matter as perceived in everyday occurrences, i.e., the rigidity or flexibility, the roughness or softness of a material [1]. While plato's contemplation may fall short of today's scientific insight, it does serve as an example for humankind's long-standing desire to understand the laws controlling the states of matter, and for the prevailing of the idea that *microscopic* features far from human perception determine the *macroscopic* properties of a material as perceived by the human sensorium.
On the macroscopic scale, a powerful and exhaustive means to characterize and understand phase transitions such as freezing and melting has been provided in modern times within the laws of thermodynamics and statistical mechanics [2, 3]. Utilizing macroscopic observables to reflect the state of a bulk material such as pressure, volume or entropy, thermodynamics allow to analyze changes in the state of a material with respect to energy,

temperature, work or heat exchange. While the analysis of individual particle dynamics is bypassed in this approach, thermodynamics have enabled the vast expansion of technical applications exploiting the macroscopic laws governing phase transitions. The success of this approach may be witnessed in prominent applications such as combustion engines, cooling circuits or most kinds of power plants [4].
Nonetheless, the microscopic processes governing phase transitions have been the subject of sustained scientific interest. In particular, this is true for freezing and melting. During the past decades, numerous phenomena which revolve around the solidification or fluidization of matter induced, e.g., by temperature or mechanical strain have been vitally discussed with respect to the microscopic mechanisms governing these transitions. Starting from analytical theories, the development of microscopic descriptions of these phenomena has been crucially propelled by the availability of suitable model systems, which enable the deduction of particle-resolved information. In addition to the development of sophisticated experimental setups and methods, this also includes the investigation of physical model systems via computer simulations.
Throughout the past decades, the scope of computer simulations has substantially expanded as the capability of computing equipment has grown exponentially [5]. Thus, the analysis of phase transitions on the microscopic scale, i.e., via the observation of individual particle trajectories, did not only enhance the understanding of freezing and melting on a fundamental level. Moreover, the diagnosis of microscopic defects, which, in general, mediate freezing and melting on a microscopic level, provides a connection between collective patterns of particle rearrangement and macroscopic transitions, which continues to bring forth significant implications for material science and engineering [6].
Naturally, the direct observation of microscopic particle motion is strictly limited by the laws of quantum mechanics, which, irrespective of the probing device, prohibit the simultaneous measurement of location and impetus of a particle at an arbitrary precision [7]. Thus, the necessity of a model system arises, which, while hosting a wealth of fundamental processes, can be accessed by direct probing methods at the "atomic" resolution of individual particles [8]. In this sense, a class of particularly favorable model systems for the microscopic investigation of phase transitions is found in the field of *soft condensed matter* or, in short, *soft matter* [9]. These include polymeric solutions, gels, foams, surfactants or liquid crystals. The unique set of properties unifying this versatile class of materials and enabling their model properties for both fundamental research and material science shall be illustrated by focussing on a further example of soft matter, that is, colloidal suspensions [10, 11].
Colloidal suspensions are composed of two constituents: The solvent particles, which form a solvent medium, and the much larger colloidal particles, which form a dispersed phase within the solvent. While the solvent particles are characterized by a structural size comparable to the typical diameter of an atom, i.e., on the scale of one Ångstrom (Å = 10^{-10}m), colloidal particles typically have sizes ranging from nano- to micrometers (10^{-9}–10^{-6}m). Thus, colloidal particles can be directly observed by optical methods, e.g. confocal microscopy [12], confocal laser scanning microscopy [13] or fluorescence microscopy [14]. Based on these direct observation techniques, a profound analysis of colloidal systems on the particle-scale can be obtained via digital processing of video microscopy data [15]. Additionally, structural properties of colloidal samples may be deduced by scattering methods

such as small-angle x-ray scattering, neutron scattering [16] or light scattering [17], which require the sample material to have structural features larger than the wavelength of the radiation used to probe the material.
The separation of length scales present in colloidal suspensions also implies a separation of time scales, which is reflected by the typical diffusion time of the two constituents. The diffusive timescale of solvent particles corresponds to picoseconds (10^{-9}s). The dynamics of the colloidal particles, on the other hand, is governed by Brownian motion, i.e., thermally induced and randomly directed kicks of the solvent particles adding up to a random displacement. The diffusive timescale is defined by the Brownian time, during which a colloidal particle diffuses over an area comparable to the square of its characteristic linear extension – for colloids, the Brownian time may well be in the range of microseconds to seconds, which enables real-time monitoring of the particle motion in experimental setups and the assessment of structural transitions within the time windows accessible to experimental observation. Typically, the energy scale of the interaction between colloidal particles is comparable to the thermal energy at room temperature.
Thus, the existence of a *mesoscopic* structural constituent, which is separated from the solvent medium by several orders of magnitude with respect to the length- and timescales and only indirectly affected by the innate dynamics of the solvent medium allows to monitor phase transitions of the dispersed phase at particle resolution by means of direct observation. In many cases, the discoveries made in such mesoscopic model systems are of fundamental character and apply to atomic systems, too [18].
The use of colloidal suspensions as a model system is promoted by the fact that experimentally, the interaction between the colloidal particles can be tailored to conform to different requirements. By utilizing a wide array of chemical synthetization techniques, colloidal particles can be prepared in various geometrical shapes, such as disks, polygonal platelets, rods, spherocylinders, spherocubes, cubes or spheres [9]. In many cases, seminal discoveries on microscopic mechanisms could be disclosed by studying the fundamental case in which the colloidal particles interact solely via the hard repulsion imposed by the principle of volume exclusion (e.g., "hard spheres") [19]. By adding non-absorbent polymeric chains to the solvent, depletion forces induce an entropic attraction between the colloidal particles [20]. When utilizing charged colloids, the electrical charge of the particles and the screening length of the interaction can be controlled by adding salt to the suspension [11].
Further possibilities to control colloidal suspensions arise from the application of external fields [21]: Colloidal particles doted with iron oxide become susceptible to external magnetic fields [8,22,23]. Thus, aligned dipole moments can be induced, leading to long-ranged, soft repulsive interactions, which can be externally tuned and controlled in real-time via the magnetic field [22, 24–27]. Optical tweezers allow to pinpoint colloidal particles to a given position [28–30], manufacture particle arrangements [31] or drag individual particles through a dense suspension [32]. Collective flow can be induced in suspension of colloidal particles via electric [33, 34], magnetic [23], or light fields [35]. Utilizing these possibilities for the synthesis and external control of colloidal suspensions, the structural properties of colloidal liquids and solids can be experimentally accessed and the transition between these stages can be steered and monitored in detail.
With soft condensed matter, the interplay between the particles constituting a solid is typically very weak compared to atomic solids [9]. Accordingly, samples of soft matter are

very easily deformed by external forces, which is expressed by small values of the Young's modulus and the shear modulus [9]. Considering their rheological properties, the materials summarized in the field of soft matter frequently exhibit viscoelastic behavior: The material response to mechanical stress is typically elastic, i.e., solid-like on short timescales but exhibits flowing, fluid-like behavior on long timescales. Thus, even very small external forces may alter the rheologic response and eventually deform samples of soft matter. Colloidal suspensions have been widely employed to sample and analyze rheological properties such as the yielding of viscous complex fluids, ageing and vitrification of amorphous media, thinning and thickening of flowing suspensions or the propagation of structural distortions within strained materials [36].
Many intriguing phenomena can be explored in binary colloidal mixtures, which are composed of two particle species and exhibit a rich base behavior under equilibrium and non-equilibrium conditions [37,38]. Examples include heterogeneous crystallization [39], demixing and layering effects under sedimentation [40–43], shaking [44, 45] or driven flow [46]. Additionally, binary mixtures play a vital role as a model system for vitreous media [47,48] or setups with frozen-in disorder [49,50].

A broad array of particle-resolved computer simulation techniques has been employed to model and analyze the behavior of colloidal suspensions, such as Monte Carlo simulations [51–54], Molecular dynamics simulations [54, 55] or Brownian dynamics simulations [56,57]. Computer simulation techniques have undergone continuous development throughout the past decades and many innovative numerical approaches have been devised to assess the dynamical and statical properties of large colloidal systems on the particle scale [58]. Up to the day, new, more efficient simulation approaches building on existing models are being developed in order to expand the system sizes and time scales accessible in computer simulations [59]. In many cases, the data deduced from computer simulations is crucial for the interpretation of phase transitions and the underlying mechanisms [60] – in the field of colloids, the interplay between experiments and computer simulations has proven to be particularly fruitful [11].

It may be remarked here that in addition to its fundamentally intriguing qualities from the standpoint of science, the class of materials denoted as soft matter is also highly ubiquitous. Not only does this apply to comparably recent, artificial examples like polymeric compound materials, cosmetic products like toothpaste, shaving cream or shower gel, paint or liquid crystals as utilized in contemporary digital displays [61]. Moreover, examples of soft matter include food products like milk or honey, elemental materials like clay, glue, ink or wax [61] but also very fundamental biological structures such as proteins, membranes or even lifeforms such as bacteria or cells [62,63].

Freezing and melting have been explored in experimental studies on colloidal dispersions and computer simulations modeling the many-body dynamics of colloids. Intriguingly, freezing and melting occur in a wide variety of situations and may be triggered, e.g., by changes in temperature or pressure, but may also be induced by mechanical strain or the presence of structural distortions. In general, the microscopic mechanism governing freezing and melting depends on the spatial topology and the external stimuli inducing the

transition, but also on the nature of the interaction which governs the arrangement of particles.
In three-dimensional space (3D), freezing can be described as a phase transition of *first order*. Thereby, the liquid releases large amounts of latent heat while maintaining a constant temperature close to the melting point [64]. During this process, localized crystalline regions emerge within the liquid. The formation of these *nuclei* of the solid phase can either occur in the bulk material, in which case it is denoted as homogeneous nucleation, or at the surface of container walls or impurities, in which case one refers to heterogeneous nucleation. The growth of crystalline nuclei into super-critical clusters triggers the expansion of the crystalline phase throughout the remaining liquid regions. The initial phase-coexistence between liquid and solid regions within the material is a distinct feature of a first order phase transition, which can be commonly witnessed in the freezing of water and in the reversal of this process. When the material is heated and cooled in a thermal loop, hysteresis may be observed with respect to the transition temperature when the transition is of first order. According to a dated definition, a phase transition of first order is identified by a discontinuity in the *first* derivative of the thermodynamic free energy with respect to a thermodynamic variable [64]. A qualitatively different type of transformation is the *continuous* phase transition, which is also denoted as phase transition of *second order*. Typical features of such a transition are a divergence of the correlation length and the susceptibility of the order parameter close to the phase transition [65].

In spite of its apparent simplicity when compared to the three-dimensional case, freezing in two spatial dimensions (2D) has eluded an explanation for a long time [1]. This elusiveness originates in a fundamental difference between two- and three-dimensional crystals with respect to the persistence of their order. This difference can be illustrated in terms of the XY model, where freely rotatable two-dimensional spins are arranged on a lattice of arbitrary dimension [67]. In this model, one may consider a disturbance of the spin direction which propagates through the lattice in a wave-like fashion. When for small angular differences, the interaction between neighboring spins is assumed to be harmonic, the energy of the wave corresponds to $L^d/(2\pi/L)^2$, where L denotes the linear extension and d the dimension of the system [66]. Thus, in the thermodynamic limit, the occurrence of such wave-like distortions is energetically favorable in one dimension and impossible in three dimension. Accordingly, the three-dimensional solid exhibits long-range order, where the correlation of the spin directions decays to a finite nonzero value even at long distances. Conversely, no ordered phase exists in the one-dimensional XY model [67]. In the Mermin-Wagner theorem [68], it was shown in detail that in two dimensions, the presence of wave-like distortions prohibits long-range order in this lattice model. Instead, the solid phase is characterized by *quasi* long-range order, where the spin-spin correlation function decays algebraically to zero.
Building on this principle, Kosterlitz and Thouless derived a methodology for the description of ordering transitions in 2D lattice systems such as 2D superfluids [69], type II

[1] A detailed account of the origins of the KTHNY melting scenario and the scientific controversy revolving around it is given in K. J. Strandburg, Rev. Mod. Phys. **60**, 161 (1988) [66]. Following the general outline depicted in this review, a brief summary of the development of the KTHNY melting scenario shall be given at this point.

superconductors [70, 71] or XY models [71]. Key to their description is the identification of topological defects, i.e. spin vortices, which mediate the transition from an ordered into a disordered state [72, 73]. In the ordered state, oppositely "charged" vortices prevail in pairs such that the topological disturbance induced by the vortices is effectively "screened" over long distances [72, 73]. Even in the crystalline phase, these bound pairs may spontaneously emerge due to thermal excitation. A disordered state is entered when the defect pairs unbind into isolated topological defects which then affect the long-range order of the system. Kosterlitz and Thouless determined an expression for the free energy related to the unbinding of a defect pair into a set of isolated topological defects and thus predicted the transition temperature above which a disordered phase emerges [73]. Utilizing renormalization group theory, the picture of two-dimensional melting presented by Kosterlitz and Thouless also implies a continuous transition from the ordered into the disordered phase [72].
When considering a 3D crystal in an off-lattice approach, the density-density correlation function corresponds to a series of δ-peaks which characterizes the long-range positional order [74]. In analogy to the previous discussion of the XY model, positional order cannot be sustained in a 2D solid due to long-wavelength fluctuations as predicted by a generalization of the Mermin-Wagner theorem to the continuous case, which was brought forth by Mermin in 1968 [75]. Instead, the density-density correlation function exhibits an algebraic decay to zero and one refers to quasi long-range positional order [75]. Simultaneously, Mermin indicated that a 2D crystal may be characterized by a qualitatively different kind of order, which is denoted as "bond orientational order" [75, 76]. Instead of focussing on the lattice positions of the particles constituting the solid, this type of order accounts for the angles between an arbitrary reference axis and the lines connecting two neighboring particles (i.e, the "bonds"). In a 2D crystal, these angles are correlated over arbitrarily long distances and one refers to long-range bond orientational order. Equivalently, bond orientational order may also be expressed via the correlation of the bond orientational order parameter, which, for a given particle, comprises the local values of the angles between neighbor bonds and reference axis.

The further progress of the theory of freezing and melting in two dimensions was driven by the subsequent works of Halperin and Nelson [77, 78] and, independently, Young [79], who presented an approach to off-lattice freezing and melting transitions based on the concept of defect-unbinding proposed by Kosterlitz and Thouless. In this case, the transition from an ordered into a disordered phase is driven by the unbinding of *dislocations*. This topological defect can be described as a deviation from the periodic crystalline structure due to the local insertion of an additional lattice line [67]. In the vicinity of a dislocation, a circular loop along the lattice segments cannot be closed - the missing segment completing the loop is quantified by the magnitude and direction of the Burgers vector [67]. Thus, the Burgers vector characterizes the topological distortion induced by the presence of a dislocation in a crystalline lattice and may be seen analogous to the "charges" of vortical defects in the lattice model [66]. An alternative illustration of dislocations may be provided by utilizing Voronoi tesselation [80]. This geometric construction derives a partition of space into cells based on a distribution of particles. The Voronoi cell attributed to a given particle is composed of all points which are closer to the respective particle than to

any other particles (in the special case of three dimensions, the Voronoi cell is also known as the Wigner-Seitz cell [67]). This concept introduces the notion of neighborhood, as the number of edges, or faces, respectively, of the Voronoi cell corresponds to the number of nearest neighbors of a given particle. In the common example of a triangular crystal in two dimensions, every particle has six nearest neighbors. A dislocation is composed of two particles, one of which has five and one of which has seven nearest neighbors.
Similar to the case discussed by Kosterlitz and Thouless, Halperin, Nelson and Young proposed that bound dislocation pairs with opposite Burgers vector emerge in the crystalline state following thermal excitation [66,77–79]. Due to a similar screening effect as discussed above, the long-range orientational order of the 2D crystal persists in the presence of such bound dislocation pairs. Above the temperature T_m, the dislocation pairs dissociate into unbound defects. The presence of isolated dislocations destroys the positional order, i.e., the density-density correlation function decays exponentially to zero. However, orientational order remains quasi long-range, that is, the bond orientational correlation function exhibits an algebraic decay [67].
Thus, a novel intermediate phase between the 2D solid and fluid phase has been characterized, in which quasi long-range orientational order persists without positional order. This anisotropic fluid phase was christened the *hexatic* phase. At the transition temperature $T_i > T_m$, isolated dislocations unbind into pairs of disclinations, which are constituted by single five- or sevenfolded defects, upon which positional and orientational order are destroyed and the system enters the disordered, i.e. fluid phase. In this phase, both orientational and positional order exhibit short range behavior and decay exponentially to zero. The theory devised by Halperin, Nelson and Young predicts that both the transition from the solid to the hexatic phase as well as the subsequent transformation from the hexatic into the isotropic fluid phase take place in a *continuous* manner, i.e., are of second order [66]. Intriguingly, the authors also establish a connection between the existence of the newly found anisotropic fluid phase and distinct alterations of the mechanical properties during melting. This is expressed by Frank's constant K_A, which represents the modulus of rotational stiffness [74]. While this magnitude is infinite in the translationally ordered solid and zero in the isotropic fluid phase, it assumes a finite, nonzero value in the hexatic phase [66]. Halperin and Nelson have also conducted a formal comparison of the Hamiltonian governing the screened interaction of free dislocations in the hexatic phase and the Hamiltonian employed by Kosterlitz and Thouless to express the interaction of vortices in their treatment of the XY model. Via this comparison, a prediction has been made concerning the behavior of Frank's constant at the transition from the hexatic to the isotropic fluid phase, according to which K_A assumes the value $72/\pi$ as T_i is approached from below and then jumps discontinuously to zero at higher temperatures [66]. The microscopic description of the two-dimensional melting process provided by these efforts has come to be known as the Kosterlitz-Thouless-Halperin-Nelson-Young (KTHNY) theory.
Besides the KTHNY melting scenario, in which 2D melting is depicted as a sequence of two continuous phase transitions, further theoretical approaches to 2D melting emerged which predict a single melting transition of first order in the fashion of a 3D crystal. These competing theories include a disordering transition mediated by grain boundaries or a simultaneous occurrence of the two-step defect unbinding proposed in the KTHNY scenario [66,81–84].

The emergence of the KTHNY theory has stimulated a multitude of experimental and computer simulation studies of the two-dimensional melting process. A detailed account of the early works probing the two-stage melting scenario may be followed in Refs. [60,76,85,86]. Despite the vast number of studies which revolve around the topic of 2D melting, up to the day, the predictions of the KTHNY theory could not be confirmed as a universally applicable principle, and neither could the theory be consistently refuted [66]. Rather than extending to all examples of 2D solids known, the validity of the KTHNY theory is evidently dependent on the type of interaction by which the system of interest is governed [87]. In particular, the fundamental case of a 2D hard disk solid played the role of an empirical test-bed, which, continuously revisited over decades, produced a wealth of controversial findings with respect to the validity of the KTHNY theory [2]. Early evidence for a first-order transition in a hard disk system was reported in a computer simulation study by Strandburg et al. in 1984 [88]. Through continuous refinement and expansion of the computer simulation approach in the subsequent years, further indications for this first-order transition surfaced [89, 90]. In 1995, these indications were manifested by a rigorous numerical analysis of the finite-size scaling of the bond orientational order parameter [60]. Simultaneously, a study based on density functional theory suggested the fundamental impossibility of a hexatic phase in a hard disk fluid [91]. In an extensive computer simulation study conducted in 1998 by Jaster [92], the analysis of orientational order in a 2D hard disk system indicated a scaling behavior consistent with the two-stage melting scenario. Additionally, the occurrence of a one-stage continuous transition could be excluded [92]. In 2011, that is, close to 40 years after the initial work by Kosterlitz and Thouless, a large-scale computer simulation study conducted by Bernard and Krauth unraveled crucial details of the melting of a 2D hard disk solid [59]. This recent work is in favor of a two-stage melting process with a continuous solid-hexatic transition and a first order hexatic-fluid transition - a result which was obtained through long-term computation and a profound analysis of the particle-resolved data obtained thereby.
As opposed to hard disks, 2D solids governed by soft, long-range repulsion have proven to be a model system in which the predictions of the KTHNY theory could be confirmed without ambiguity. Early experimental observations of a two stage melting process were made in colloidal systems with coulombic interactions [15] as well as in colloidal lattice systems with magnetic interactions [93, 94]. In 1997, Zahn et al. proposed a novel experimental realization of a planar colloidal monolayer, which is achieved by dispersing superparamagnetic polysterene beads in a hanging water droplet [24]. Due to gravity, the particles sediment until they reach the air/water-interface, where further downward motion is hindered by the surface tension of the water droplet. Thus, a very stable confinement of the particles into a nearly perfect monolayer is achieved, where the vertical deviation of the particles within the layer is below 1% of their diameter [8]. The superparamagnetic properties of the colloidal particles used in this setup originate from a doting with Fe_2O_3 iron oxide [8]. Via the application of an external magnetic field with field lines perpendicular to the plane of confinement, parallely aligned dipole moments are induced to the particles.

[2] For an exhaustive review of the computer simulation studies which seminally contributed to the understanding of 2D hard disk melting, see H. Weber and D. Marx and K. Binder, Phys. Rev. B **51**,14636 (1995) [60]. Following the scope of this review, a brief summary of these works is given here.

The parallel alignment of dipoles then leads to a purely repulsive, long-range interaction which scales with the inverse cube of the particle separation [22]. Intriguingly, the strength of the particle interaction can be externally tuned by altering the magnetic field strength. Thus, the system can be effectively heated or cooled, which enables to track the melting process while securing a thermal relaxation of the monolayer at every particular temperature step [8].
Probing this colloidal model system with video microscopy, the predictions of the KTHNY could be fully confirmed by monitoring the distinct degree of orientational and translational ordering predicted for the solid, hexatic and isotropic fluid phase [25, 95]. The colloidal samples utilized in these studies contained $\sim 10^5$ particles. Furthermore, this experimental setup enabled the detailed confirmation of the predicted behavior of Frank's constant K_A, thus providing very explicit evidence for the validity of the KTHNY scenario [74]. Also, a dynamical criterion for the distinction of the three phases based on the Lindemann parameter was deduced from these observations [95]. Also, numerical assessments of the two-dimensional melting in systems with dipolar interactions supported the validity of the KTHNY scenario [96].
Apart from probing the KTHNY melting scenario, the experimental setup depicted above was also employed to sample the behavior of binary mixtures of colloidal particles with different magnetic susceptibilities when exposed to rapid quenching. Thereby, a pronounced increase of the magnetic field was conducted after the mixture reached thermal relaxation, equivalent to a strong decrease of temperature which is quasi-instantaneous with respect to the diffusive timescale of the particles [97]. The subsequent formation of localized crystalline regions exhibited both triangular crystallites, which are composed of only one species, as well as crystallites which correspond to a checkerboard pattern, where both particle species are arranged in a square lattices and the two lattices are shifted relatively [97]. In further experiments and computer simulations [98, 99], the formation of crystalline patches in the suspended monolayer after a quench was monitored using a cluster criterion. Thereby, the nucleation mechanism governing the growth of polycrystalline regions could be distinguished from the two-step melting process observed in Ref. [95].
While the KTHNY scenario was unambiguously confirmed for soft, long-range repulsive potentials, numerous studies consistently suggested the invalidity of the theory for the case of hard disks. For soft, short-range repulsive interactions, however, results in favor of the KTHNY scenario were reported [100] as well as observations contradicting the theory of a two-stage continuous melting process [101,102]. Only recently, a large-scale computer simulation study systematically probed the dependence of the interaction range on the melting process in systems with repulsive interactions of the shape $\sim r^{-n}$ [103, 104]. The results suggest that for $n > 6$, the melting process corresponds to the scenario associated with the melting of a hard disk solid and the hexatic-fluid phase transition is in fact of first order, in agreement with the hard-disk scenario discussed in Ref. [59]. For exponents $n < 6$, however, the predictions of the KTHNY melting theory have been recovered [103, 104]. The effect of potential softness on first order signatures in the hexatic-fluid transition was also addressed in Ref. [105].
A further question concerning the scope of the KTHNY theory was tackled in a computer simulation study by Gribova et. al. [106], where the melting process in a monolayer of soft repulsive particles was compared to stacks of multiple particle layers. Via a thorough

finite-size analysis building on methods established in Refs. [60, 88], it could be shown that even slight deviations from a 2D confinement inhibit the occurrence of the hexatic phase [106]. Recent experimental studies in magnetized monolayers [107] or single-layer complex plasmas [108] have further expanded the current knowledge of 2D melting.

Melting in a pure, planar confinement is, however, a phenomenon rarely witnessed in nature. More commonly, 2D melting occurs in the presence of a substrate. This might be embodied by the surface of a solid, to which the melting agent adsorbs. A vital example of such realizations of two-dimensional confinement is adsorbtion to graphene sheets [109]. Typically, the underlying surface will exhibit some roughness, thus introducing a certain degree of disorder. This may be caused by randomly distributed indentations or bumps, as well as other repellent or attractive obstacles. The presence of such immobile obstacles is denoted as quenched, i.e. frozen-in disorder. Numerous experimental setups may be named in which the presence of such immobile defects crucially affects the phase behavior. Among these are type II superconductors, where magnetic vortices are formed in the presence of a magnetic field. The range of technical applications of type II superconductors is affected by the pinning of magnetic flux lines due to structural defects [110–112]. Also, the presence of quenched defects places a crucial role in the phase behavior of liquid crystal films [113], synthetic and biological Langmuir-Blodgett films [114, 115] or two-dimensional protein crystals [116].
The presence of frozen-in obstacles affects the pure, uniform background of the melting process which is presumed in the KTHNY treatment. Soon after the initial proposition of the KTHNY scenario, Nelson et al. conducted a renormalization group analysis of how weak disorder affects the 2D melting scenario [117, 118]. Thereby, a bead-spring model was considered, where a periodic arrangement of beads is interspersed with larger beads, and neighboring beads are connected with springs. The large obstacles do not interrupt the periodic arrangement of beads but induce a local dilation of the lattice. The authors argued that the presence of such quenched impurities obstructs the stability of the solid phase as they break up thermally excited dislocation pairs, and triggers a disorder-induced melting of the solid into the hexatic phase. Thus, the temperature T_m, which marks the transition from the solid to the hexatic phase, was predicted to shift to lower values with increasing degrees of disorder. Also, it was suggested in [117] that above a critical degree of disorder, no solid phase can be established at all. As opposed to the strong influence of quenched disorder on the solid-hexatic transition, only a slight dependence of the hexatic-fluid transition temperature T_i on disorder follows from the analysis conducted in Ref. [117]. Overall, the influence of quenched disorder was predicted to induce a broadening of the stability range of the hexatic phase at the expense of the stability of the solid phase. This initial treatment of 2D melting in the presence of weak disorder also implied a reentrant transition from the solid to the hexatic phase upon cooling for finite, subcritical degrees of disorder [117]. The implication of a reentrant melting transition was initially supported by a further analysis of the effect of quenched impurities based on continuum elastic theory [119].
In computer simulation studies subsequently conducted by Shi and Berlinsky [120], the formation of topological defects in the presence of an underlying random pinning potential has been analyzed and the defect patterns emerging in the cases of high and low pinning

disorder have been discussed. The authors observed a melting transition which is mainly attributed to the formation of extended grain boundaries in the presence of high disorder, which crucially affects the particle dynamics and promotes collective hopping [120]. Thus, early particle-resolved observations of the disorder-induced melting transition was provided.

Further contemporary studies disputed the widening of the hexatic phase and proposed that the hexatic phase is suppressed in the presence of sufficiently strong disorder, which melts the hexatic into an isotropic fluid [121]. In a later work by Cha and Fertig, a continuum elastic theory analysis of the 2D melting process was conducted in the presence of a slowly varying random potential, which was supported by additional computer simulation data [122]. In their treatment, the authors indicated a flaw in the renormalization group analysis conducted in [117]. This flaw is related to the fugacity expansion commonly applied in renormalization group theory. In the case of 2D melting in the presence of impurities, the fugacity expression is employed to assign a thermal probability to the event that a given lattice site is occupied by a dislocation [122]. However, the common expansion in the fugacity, which formally simplifies this expression, is forbidden here. This is due to the range of values of the dislocation-disorder energy entering in the fugacity, which, in some rare cases, might cause the simplified term to diverge while the original expression would approach zero instead. This formally overstated the probability for a dislocation to be created in the presence of disorder and promoted the prediction of a reentrant melting transition at low temperatures in the presence of arbitrarily small disorder. This concept was thoroughly revised by Cha and Fertig, who pointed out that in the presence of weak disorder, the solid remains stable at low temperatures [122]. However, they confirmed the existence of a critical degree of disorder above which melting of the solid is induced. Additionally, the impact of disorder on the solid-hexatic transition temperature T_m predicted in [117] was recovered in [122]. While a profound understanding of the disorder-induced melting of a solid into a translationally disordered state was provided in [122], the stability range of the hexatic phase was not resolved in this work.
The findings of Cha and Fertig were probed by a numerical study on superparamagnetic colloidal particles, which interact with a planar substrate featuring attractive potential wells [123]. In this work, the temperature-induced melting of the 2D solid in the absence of quenched disorder was compared to the disorder-induced melting at zero temperature. Thus, two different melting procedures could be resolved and compared on a microscopic level. The authors observed that with disorder-induced melting, increasing random disorder induces the creation of dislocation pairs and thereby enables the release of strain [123]. Thus, evidence was provided for the prediction that crystalline order can be maintained at zero temperature in the presence of finite quenched disorder while increased numbers of quenched impurities will trigger a disorder-induced melting. This is opposed to the temperature-induced melting process, where, as predicted in the classic KTHNY picture, the unbinding of dislocation pairs, which are already present in the crystalline phase triggers the disordering transition, as could be observed on a particle-resolved level [123]. In accordance with the scope of Ref. [122], the numerical study presented in Ref. [123] did not contain a specific diagnosis of the hexatic phase and its stability range but merely differentiated between the ordered and disordered state.

Simultaneously, first experimental realizations of two-dimensional colloidal systems featuring quenched disorder emerged and were employed to probe the influence of disorder on the melting scenario. In [93], a monolayer of dipolar colloidal particles has been realized by confining the colloids between two glass plates, where repulsive dipolar interactions are induced via the application of an external magnetic field. A small fraction of the particles has a larger diameter than the remaining, monodisperse particles and is stuck between the glass plates. These immobilized particles constitute frozen-in obstacles. The authors did not report on the occurrence of the hexatic fluid phase but rather pointed out that the solid phase, which was observed at high magnetic field strengths, relaxates into a stage denoted as hexatic glass [93]. This phase was found to bear the structural properties of the hexatic fluid phase but emerged from the solid phase without a change of temperature or magnetic field strength, respectively. Instead, the structural crossover into a translationally disordered state was attributed to the pinning of dislocations to the immobilized obstacles [93]. When decreasing the magnetic field strength, however, a disclination-unbinding mechanism was observed and the melting into the isotropic fluid phase was found to conform to the pure 2D melting scenario [93].
Substantial insight into the influence of quenched disorder on the structural properties of 2D solids was also provided by Pertsinidis et al., who studied a suspension of charged colloidal particles confined between a quartz bottom plate and a cover slip [34]. In this setup, quenched disorder has been introduced by roughening the surface of the quartz container wall by utilizing an ion-etching technique [34]. The roughened structure then induces a random pinning potential. In order to measure the influence of different degrees of disorder on the topological order of the 2D solid, structural features were etched into the surface on three distinct heights [34]. Thus, by reducing the separation of the two container walls, the degree of structural disorder induced by the random potential landscape could be altered *in situ* [34]. Thereby, the authors were able to experimentally verify that an increase of random disorder gradually deteriorates the translational and orientational order of the 2D solid and induces a transition into the hexatic phase. With a further increase of random disorder, the hexatic phase was observed to transform into an isotropic fluid phase [34]. The authors also probed the depinning of particles in a random potential landscape under the application of an external driving field and exposed that the dynamic properties of the depinning transition suggest a coexistence between solid and fluid regions in the monolayer [34].
In an experimental study on 2D colloidal system conducted by Yunker et al. [100], the transition of a crystal into a glass due to quenched disorder has been studied. The colloidal particles utilized therein interact via a short-range repulsion similar to that of hard spheres and quenched disorder has been introduced by inserting smaller particles into the mixture. The authors have thoroughly assessed the properties of the crystal-glass transition by monitoring the bond order parameter susceptibility and the number of dislocations. Through this analysis, it could be concluded that the disorder-induced crystal-glass transition resembles the crystal-fluid transition in terms of the structural transformation. Additionally, the authors reported a significant alteration of the particle dynamics reflected by a strong increase of the dynamic correlation length during the crystal-glass transition [100]. The disorder-induced transition of a crystal into a glass was also addressed in Refs. [124–127].
In an experimental assessment of the melting of Argon monolayers on graphene films, it

could be shown that the insertion of impurities alters the melting process from first order to second order and introduces a state reminiscent of the hexatic phase [128]. In further computer simulation studies, additional dynamical effects in two-dimensional systems in the presence of topological distortions have been reported. These include subdiffusive behavior in the presence of weak random disorder [129], as well as smectic flow and directional mode locking upon depinning in a periodic array of pinning sites [130, 131]

Despite the fact that the 2D melting process and the influence of quenched disorder on its occurrence have been evaluated and analyzed in various experimental and simulation studies, none of these works specifically tested the predictions stated by Nelson and coworkers [117, 118] concerning the stability range of the hexatic phase in the presence of quenched disorder. In the article "Two-dimensional melting under quenched disorder" [132], which constitutes the first part of this work, an experiment is presented to probe this predicton and to resolve the stability range of the hexatic phase for varying degrees of quenched disorder. Superparamagnetic colloidal particles are confined to the bottom of a glass container by gravity. As in Refs. [95, 97], the application of an external magnetic field perpendicular to this surface induces parallel dipole moments, leading to soft, long range repulsion between the colloidal particles. When the colloidal particles sediment to the glass plate, a fraction of the particle is pinned to the surface. This pinning is caused by van der Waals attractions and chemical interactions [132]. The randomly arranged pinned particles constitute a frozen-in array of obstacles. Intriguingly, in this setup, the particle interaction is the same for the obstacle particles as for the freely dispersed colloids. Thus, a second species of particles is constituted and a binary mixture of mobile and immobile, i.e., pinned particles can be explored.
As depicted above, the corresponding reference case of pure 2D melting could be realized by confining the particles to the surface of a hanging droplet, a setup which unambiguously confirmed the predictions of the KTHNY scenario [74, 95]. By probing different regions of the sample with varying pinning fractions, the influence of pinning disorder is monitored systematically in [132]. Particle trajectories are recorded using video microscopy, which allows for a particle-resolved analysis of dynamical and statical properties. Starting from an equilibrated crystalline state, the melting process is monitored by incrementally reducing the strength of the external magnetic field, which corresponds to an effective heating of the system [132]. The system is allowed to equilibrate for 24 hours before trajectories are recorded. Thus, the decay characteristics of the bond-orientational order correlation function are probed in every sample region at every distinct temperature step. Additionally, particle-resolved computer simulations of the melting process in the presence of randomly pinned particles are conducted. These enable an extended sampling of pinning disorder and contribute static and dynamic particle information, from which the characteristics of the two-step melting process can be deduced.
For each parameter combination of pinning fraction and magnetic field strenght, that is, inverse temperature probed in the experiment and the computer simulation, the occurrence of liquid, hexatic and solid phase is compiled into a phase diagram. In this phase diagram, the broadening of the stability range of the hexatic phase is clearly reflected. Specifically, the hexatic-solid transition shifts to lower temperature in setups with increased pinning disorder while at the same time, the fluid-hexatic transition is only weakly affected. This

behavior corresponds precisely to the predictions stated by Nelson in [117], and the data obtained in computer simulation and experiment are in good agreement. Furthermore, spatiotemporal fluctuations of the bond orientational order are observed close to the phase transitions, pointing towards continuous transitions [132]. Qualitatively, these heterogeneous patterns of orientational order conform to observations reported for an impurity-free two-dimensional Lennard-Jones system [133]. Also, several finite size scaling methods, which were previously established and applied e.g. in Refs. [60, 106], support the finding that the melting process observed in the presence of pinning disorder consists of two continuous phase transitions [132]. Based on the findings of [74], where the behavior of Frank's constant K_A was specifically verified, the scaling of K_A is monitored for different fractions of pinning disorder. This analysis reflects the shift of the transition temperature T_m, at which K_A diverges.
Furthermore, intriguing dynamic properties of the particles in the vicinity of pinned obstacles are found: In the fluid phase, these particles exhibit slower dynamics than the remaining particles, which are sufficiently apart from obstacles. In the solid phase, this behavior is inverted, and the particles in the vicinity of pinning sites exhibit increased dynamics when compared to the particles in regions unaffected by disorder, which might point towards an increased probability of defect unbinding in the proximity of pinned particles in the solid phase as discussed in [117, 122].

The second part of this work is constituted by the article "Fluctuations of orientational order and clustering in a two-dimensional colloidal system under quenched disorder" [134]. Therein, an extended analysis of the experimental and simulation data of the 2D melting process in the presence of pinning disorder is presented. The widening of the hexatic phase discussed in [132] can, by this analysis, be attributed to the formation of bond orientational clusters, the emergence of which is inhibited in the presence of disorder. These bond orientational clusters are topologically connected regions with uniform bond orientation order, which appear in the isotropic liquid phase and merge into larger regions throughout the hexatic phase. By visualizing these clusters, it is possible to monitor the continuous formation of crystalline order throughout the hexatic phase [134]. These orientational clusters undergo strong spatio-temporal fluctuations on time scales beyond the orientational correlation time [134]. Thus, orientational cluster can be readily distinguished from polycrystalline regions or crystal nuclei which would indicate a phase transition of first order [106]. By stating cluster criteria similar to those suggested in Ref. [98], orientational clusters are detected in both experimental and simulation data and are thoroughly evaluated. Specifically, cluster densities, average cluster sizes and the population of noncluster particles are assessed as a function of system temperature and disorder strength [134]. It is found that the presence of pinning disorder impedes the merging of clusters. Instead, in the presence of pinning, a multitude of comparably small clusters prevails over a broad temperature range. At low temperatures, the probability for a particle to be included in a cluster is reduced if it is located in the vicinity of a pinned particles. At high temperatures, this probability is increased and clusters preferentially emerge in the proximity of pinning sites. This corresponds to similar findings with respect to the particle dynamics in the vicinity of pinning sites observed in [132].
Also, the occurrence of the KTHNY melting scenario is supported by a further finite-size

scaling analysis and a distinct diagnosis of the topological defects based on Voronoi tesselation, i.e., bound and isolated dislocations as well as single disclinations [134]. Overall, this combined approach of computer simulation and experiment supports the two-step melting scenario in the presence of quenched disorder. The widening of the hexatic phase with increasing disorder can be traced back to the characteristic properties of orientational clusters and their formation and growth during the melting transition [134].

The investigation of the two-dimensional melting process via superparamagnetic particles presented in Refs. [132, 134] and previous works [25, 97] is reviewed in the article "Two-dimensional colloidal mixtures in magnetic and gravitational fields" [135], which constitutes the third part of this work. In this review, results on the sedimentation behavior of mixed colloidal suspensions under time-dependent gravity are alos discussed, which have been originally stated in [45].

Within the KTHNY melting theory, it has been established that the formation and unbinding of dislocations mediates the structural transition from a crystal into a liquid and that the presence of topological defects, i.e., bound or isolated dislocations as well as disclinations, alters the mechanical properties of a material in a distinct way - as an example, it has been pointed out that the presence of isolated dislocations induces a finite rotational stiffness [74]. In a wider sense, the creation and diffusion of defects governs the transformation of crystalline solids in a broad range of scenarios where the material responds to external stimuli. Apart from temperature- or substrate-induced transitions, this is particularly true for the application of mechanical stress, which may induce material fatigue, deformation, or fluidization of a solid [136]. The stability of crystalline solids under stress may also be compromised by the formation and propagation of microcracks [136, 137]. In many technical applications, precise knowledge of the material response to stress and a profound understanding of the underlying microscopic deformation mechanisms is imperative. Examples include aeroplane wings, which endure heavy strain but may be severely compromised by the presence of microscopic fissures [138, 139]. Also, the biomechanical process of bone fracture is governed by the formation and dissipation of cracks starting from an initial microscopic disruption [140, 141]. In all of these situations, the formation and motion of topological defects is key to the understanding of the structural transition a crystalline solid undergoes [136, 142, 143].
The mechanical response of a solid is typically elastic, i.e., reversible, when a small stress is applied [144]. If the stress is removed, the solid will return to its previous state and the topological order of the particles constituting the crystal remains unaltered. When a high stress is applied, the mechanical response crosses over to plastic, i.e., irreversible deformation [145, 146]. The structural changes occuring during plastic deformation are not restored when the stress is removed. On the microscopic scale, plastic deformation in a crystal is typically driven by numerous, correlated instances of topologic rearrangement, which are referred to as a *plastic events* - for example, these may correspond to bond breaking [147, 148] or discrete slip events [149].
The specific value of stress at which the mechanical response of a solid crosses over from elastic to plastic deformation is known as the yield point [144].
In general, a material which is solid in the absence of mechanical stress will exhibit flowing

behavior once an applied stress exceeds the yield point, leading towards a deterioration of the crystalline structure through fluidization or cracking [145, 146, 150]. Conversely, the mechanical response of a liquid ideally corresponds to plastic deformation, i.e., flowing even when the applied stress is very small [144]. Thus, ideally, when a liquid is deformed due to weak mechanical stress and the stress is removed, the liquid will remain in the deformed state irrespective of how small a deformation occurred [144].
However, when studying the behavior of flowing matter, which is done in the field of rheology [144], many phenomena emerge which require a broadening of the distinction between liquid and solid. For example, many fluid substances are known to respond elastically to an increase of stress or the sudden removal of stress - some fluids will resist weak stress or will gradually recover after the stress has been removed [48]. In this case, one refers to viscoelastic behavior [144]. On the other hand, various solids do exhibit slow and gradual plastic deformation even below the yield point. An example of such viscoplastic behavior is creep flow [151, 152].
When performing rheological studies, a material is examined in a predefined loading scenario in order to determine material properties such as rigidity, viscosity or the yield behavior. A typical setup which is of high relevance for many technical applications is the study of a material under Couette shear flow [144]. Thereby, a sample is considered between two boundary plates which move relatively with a prescribed velocity, such that the strain in the sample increases at a linear rate with increasing distance from the bottom layer and is homogeneous within a layer parallel to the boundary [144]. Another fundamental loading scenario is Poisseuille flow, which corresponds to the flow of a material which is pumped through a tube [46, 144]. Experimentally, these flowing properties of a given medium are studied using a range of technical appliances known as rheometers, in which a specific flow profile can be maintained.
Under the influence of strong shear flow, the order of crystalline materials may be destroyed and one refers to shear-induced melting [150, 153–158]. In light scattering experiments on colloids, it has been observed that the presence of shear flow triggers the melting of a crystal even at temperatures and densities which, under equilibrium conditons, correspond to the stability of the crystalline phase [154,159]. The shear-induced melting process observed in [159] consists of several stages which emerge with increasing shear rates. After an initial formation of discrete, sliding layers in the material, these expand into mobile bands upon increasing shear rate [153,159]. Ultimately, the entire system assumes a flowing state [159].
In a numerical assessment of the shear-induced melting of soft-sphere crystals, which followed the initial observation of shear-induced melting in experiments, it has been suggested that the viscoelastic behavior of many fluids may, in general, be explicable in terms of a shear-induced phase transition [153]. Recent experimental studies on soft colloidal crystals have resolved the shear-induced melting of one-component crystals on the particle level by utilizing confocal microscopy [150, 158]. Thereby, shear flow was found to enhance the mobility of particles, thus contributing to the 'thermal' dissociation of the crystalline structure. Additionally, the authors have proposed a measure for the cumulative effect of shear flow and thermal motion, implying a melting criterion in the manner of the classical Lindemann criterion [160]. The latter is employed to predict the stability of an equilibrium crystal based on the particle fluctuations [95]. In a further experimental study on the melting of colloidal suspensions under shear it has been established that qualitatively, the

melting process induced by shear flow differs strongly from equilibrium melting, which is reflected by large-scale fluctuations of the order parameter and the emergence of crystalline domains in the material after the onset of shear-induced melting [150]. Conversely, shear flow may induce ordering phenomena, too, such as the formation of crystalline clusters in isotropic suspensions [150] or the alignment of a crystalline layer with respect to the direction of shear [161]. For weak shear flow, coexistence of a strained crystal and a sheared melt can be observed [162].
Adding to the insight obtained by studying the fluidization of solids in simple shear flow, perturbation methods like microrheology [32] or nanoindentation [163] allow to deduce flow properties of a material. In microrheology, the motion of a tracer particle is utilized to probe the rheologic response of the surrounding medium [164]. In indentation measurements, a sample is locally perturbed with a point-like tip, which induces cracking and local fluidization [18].

A fundamental understanding of the plastic deformation of crystalline solids can be obtained by studying the formation and propagation of dislocations. Over decades, numerous studies have expanded our understanding of the interaction of dislocations, their individual and collective motion as well as the local accumulation of defects during plastic deformation [145, 149, 164–171]. Experimental and numerical studies have explored the spatially and temporarily heterogeneous patterns of dislocation formation, which accompany plastic deformation in a crystal and addressed the scale-free flow inherent to defect dynamics [18, 149, 172–174].
A fundamental framework for the investigation of crystalline plasticity based on topological defects is the plastic response of a perfect one-component crystal. Building on theoretical models for the dissipation of dislocations in a one-component crystal, acoustic emission experiments on macroscopic ice crystals have elucidated the plasticity of crystalline solids [172, 174, 175]. In these experiments, the avalanche-like propagation of dislocations through a macroscopic sample of ice is detected acoustically [149]. Furthermore, discrete dislocation dynamics computer simulations have been applied to study the plastic deformation of single-crystals. These allow to model the collective arrangement of dislocations [169, 172, 176, 177]. Thus, the numeric treatment of crystalline plasticity via mean-field models [178] could be extended to a discrete treatment of defects.
Further large-scale computer simulations based on this technique have captured the formation and annihilation of dislocation loops in the vicinity of a crack tip [173]. Through a comparison of atomistic simulations and mesoscale dislocation dynamics simulations, the microscopic dynamics of the topological defects could be directly related to the mesoscopic deformation of the material subject to mechanical perturbation [173]. Experimentally, similar findings have been provided by a study of colloidal crystals, where the perturbation induced during the indentation of a crystalline colloidal layer with a needle tip has been analyzed via laser diffraction microscopy [18]. The formation of dislocations in the initially defect-free sample in the vicinity of the indentation could thus be resolved on the particle scale [18]. Via continuum modeling, the authors characterized the defect nucleation rate in the colloidal crystal based on thermal fluctuation of the particles and the applied strain, deriving relations, which, intriguingly, are also applicable to atomic crystals [18]. Further experimental studies assessed the plastic deformation of crystalline materials by

tracking structural slip events, which are mediated by the gliding of dislocations [149,172]. In Ref. [149], these 'discrete slip events' where directly monitored via transmission electron microscopy in measurement of nickel microcrystals under shear. Thereby, it has been shown that the spatial extension of slip events spans many length scales and that the dislocation system in fact exhibits scale-free behavior [149], as was previously suggested in computer simulation studies and theoretical models of dislocation propagation [178, 179]. These findings support the view that the plastic response of one-component, single-crystals is a highly heterogeneous process, which, qualitatively, often resembles plate tectonics rather than fluid flow, as pointed out in Ref. [149]. The deformation process is mediated by structural deteriorations on various length- and time-scales, which occur in an avalanche-like pattern [149,172].
However, this avalanche-like propagation of dislocations is more controversial when considering polycrystalline materials, in which multiple crystalline domains are separated by grain boundaries [148,174]. In an experimental study on polycrystalline ice samples with grain sizes distributed over many length scales, it was found that the scale-free gliding motion of dislocations can only partly be retrieved when the propagation of defects is impeded by grain boundaries [174]. While the size of dislocation avalanches was found to be governed by the scaling of the crystal grains, supercritical effects may induce the formation of secondary avalanches in adjacent crystalline domains [174]. These effects were also supported by Monte Carlo computer simulations [174].
Computer simulation studies on polycrystals under shear have further suggested that, besides the avalanche-like diffusion of dislocations, the plastic deformation is also driven by the cooperative sliding motion of particles along grain boundaries [147,148]. This collective motion is accompanied by large stress drops, indicating the release of stored elastic energy [147]. As a model system for the study of 2D polycrystalline samples, binary mixtures of softly repulsive particles with varying compositions are employed in Refs. [147,148]. Thereby, the composition of the two particle species has been tailored in order to inhibit full crystallization and promote the formation multiple polycrystalline domains [147,148].

It may be noted here that the formation and diffusion of dislocations in a one-component crystal is not only crucial for irreversible deformations, but also governs relaxation processes in the presence of small stress. The patterns of collective motion governing the elastic response of a triangular crystal to internal stress were recently probed experimentally in a 2D soft colloidal crystal [164]. In this setup, individual crystal particles were excited with an optical tweezer, and the subsequent collective response of the surrounding particles was precisely analyzed using bright field microscopy. Evaluating the particle trajectories, cooperative patterns of particle motion could be identified, which correspond to the propagation of dissociated vacany-interstitial pairs or the intermittent formation of grain boundaries [164]. Notably, these collective patterns of motion do not introduce lasting structural defects but mediate the relaxation of the crystal into an undisturbed state. Intriguingly, these patterns qualitatively correspond to the response of the colloidal crystal to thermally induced perturbations [164].

While the study of crystalline plasticity typically revolves around the observation and analysis of well-defined topological defects, in general, no such object can be readily de-

termined when investigating the plasticity of amorphous materials [180]. During the past decades, numerous experimental and computer simulation studies have addressed the rheological response of amorphous materials such as foams [157], emulsions [181] metallic glasses [182], polymer solutions [65] or colloidal suspensions [183], which may assume disordered, vitreous states. In general, these examples of soft matter behave like a solid and respond elastically when a small shear stress is applied but start flowing when the applied stress exceeds a yield value [184, 185].
In the field of rheology, these materials are also denoted as "yield stress fluids" [186] or "soft glassy materials" [185]. Rheologic studies on the properties of these media under shear flow have detected a broad range of intriguing properties - these include nonlinear effects like shear-thickening or shear-thinning, where the viscosity of the flowing material decreases or increases, respectively, with increasing shear rate [187, 188]. Such flow properties are in distinct contrast to the behavior of ideal, i.e., Newtonian fluids where the viscosity is not a function of the shear rate and one refers to non-Newtonian fluids in this case. Common examples of non-Newtonian fluids include shear-thickenig cornstarch solutions [189], which solidify when a strong external force is rapidly applied. The hardening of shear-thickening fluids upon a sudden perturbation is also exploited in the ongoing development of novel protective gear [190]. An everyday-life example of a *shear-thinning* fluid is ketchup, which, due to the insertion of xantham gum during the manufacturing process, flows more easily when squeezed through the bottleneck [191]. Many more complex fluids like paints or pastes exhibit shear-thinning properties and flow smoothly when they are pressed, smeared or stirred [190]. Also, shear-thinning polymer fluids are commonly employed as a drilling fluid [192]. Throughout the past decades, the non-Newtonian flow properties of complex fluids have been addressed in numerous experiments [36]. Building on the continuous progress of theoretcal models and algorithmic approaches [193, 194], numerous computer simulation studies [55, 56, 193, 195–199] have further elucidated the non-linear flow properties of complex fluids.
Another class of intriguing phenomena which have been thoroughly studied in the context of amorphous plasticity are dynamic heterogeneities in the sheared medium, i.e., shear banding or localization [36, 47, 200]. With shear localization, the medium subject to shear flow separates into coexisting regions of higher and lower shear rate or may even contain regions which do not move at all [47]. The formation of concentrated flow regions is almost ubiquitous in sheared complex fluids with mesoscopic structural features which may jam into soft, disordered states [36, 201]. Thus, shear bands have been observed in granular media, pastes, foams and emulsions but also colloidal suspensions under shear [201–204]. As pointed out in Refs. [47, 185, 205–209], these dynamic heterogeneities arise due to the interplay of the slow dynamics inherent to amorphous materials and the imposed dynamics of the external shear flow. Varnik et al. thoroughly assessed the emergence of shear localization in a computer simulation study of a model amorphous solid under shear flow [47]. The amorphous solid discussed in [47] is a glass-forming, 80:20 binary mixture consisting of 4800 particles, which interact via the Lennard-Jones potential. The sample is located between two boundary walls, one of which moves at a prescribed velocity, whereby Couette shear flow is imposed. The authors observed that, for low shear rates, the system is divided into a sheared region, in which the velocity of the particles in the direction of shear increases linearly, and an arrested region, in which the particles are largely unaffected by shear and

do not move noticeably in the direction of shear. With equal probability, the sheared region may be adjacent to the moving, upper boundary or the resting, lower boundary, as was concluded from multiple repetitions of the computer simulation and conforms to the assumption that the boundaries are interchangeable due to galilean invariance [47]. Above a certain value of the wall-imposed shear rate, the shear band covers the entire system [47]. At this particular value of the shear rate, the shear stress corresponds to the yield stress. This suggests a multivalued region in the shear stress vs. shear rate curve below the yield point, where shear-banding prevails [47].
Further numerical studies have addressed the emergence of spatiotemporal heterogeneities such as shear banding in the shear response of amorphous media [186, 210]. As deduced from particle-resolved computer simulations conducted by Chaudhuri et al., shear-banding in amorphous media is, in general, not a permanent state, although very long-lived spatial heterogeneities may arise depending on the applied shear rate and the interaction potential of the jammed particles [211]. Specifically, attractive forces between the particles were found to promote the formation of long-lived heterogeneities [211]. The emergence of shear bands is also highly dependent on the age of the sample, as was established in Ref. [212]. Furthermore, shear bands may be induced by the spatial confinement of the flowing medium [213] and can also be affected by impurities, as was found in experiments on binary amorphous metals with embedded nanocrystals [214].

A lot of effort has been made to characterize the nature of plasticity in amorphous media in terms of the local structural rearrangement, thus providing a means to formally address plastic effects like spatiotemporal flow heterogeneities, shear bands or avalanche-like deformations in disordered materials in spite of the lack of distinguishable topological defects [3]. An initial approach for the characterization of plastic deformation in amorphous materials was presented by Maeda and Takeuchi in their computer simulation study of a metallic glass under shear [182]. Through a particle-resolved analysis of the deformation process, Maeda and Takeuchi were able to identify spherical regions in which the plastic deformation is localized. In these regions, which span several atomic distances, the particles are displaced according to a distinct, quadrupolar pattern of motion by which strain energy is released [182]. Similar findings were reported in experiments on soap bubbles conducted in [215], which suggested that plastic deformation is mediated by the rearrangement of particles within a localized region in an amorphous material. Such deformation patterns in foams where formally defined as "T1" events, which correspond to a localized, irreversible exchange of topological neighborhood relations in a dense arrangement of particles [181, 216, 217] and constitute an example for elemental plastic events in amorphous media. From the observation of localized plastic events, the concept of "shear transformation zones" was derived [218, 219], which also entered in the description of flow heterogeneities and strain localization [220]. Building on this concept, Maloney and Lemaître have addressed the spatial structure of plastic deformation in sheared, athermal glasses by computer simulations [180]. They have identified a distinct real-space structure of plastic

[3] An elaborate review of the formal description of plastic events in amorphous media is presented in C. E. Maloney and A. Lemaître, Phys. Rev. E **74**, 016118 (2006) [180]. Following the outline depicted therein, a brief summary of the works contributing to this description shall be given at this point.

events which corresponds to a quadrupolar rearrangement pattern [180]. Furthermore, the authors found that the plastic deformation can be separated into localized shear transformations, which accumulate into "slip lines" spanning the entire system [180]. Intriguingly, these findings are largely unaffected by the details of the particle interaction [180]. In a similar computer simulation approach, Tanguy et al. have assessed the spatially heterogeneous plastic response of a model amorphous material in athermal flow [221]. In some analogy to [180], they have identified quadrupolar rearrangement patterns as well as vortical rearrangements. The alignment of such large-scale plastic events was found to induce the formation of shear bands in the material [221].
The structural rearrangements governing plastic deformation in thermal amorphous materials under shear were probed experimentally in [222], where a sheared colloidal glass was monitored by direct real-space observation. The authors identified discrete shear transformation zones and measured the local dedistribution of strain in the vicinity of plastic events. Also, the authors detected a spatial correlation between shear transformation zones, which interact via a long-range elastic stress field [222]. According to these findings, plastic events in the flowing material induce further structural transformations in their vicinity.
Further crucial insight into the underlying mechanism of plasticity in sheared amorphous materials was recently provided by Mandal, Varnik and coworkers [223, 224]. Through computer simulation and experiment, they assessed the dynamical fluctuations arising in a sheared, thermal colloidal glass on a single-particle level, reflecting the dynamic impact of plastic events [223]. Also, the authors evaluated the dynamical correlations of particle fluctuations in the sheared material, as expressed, e.g., by the dynamic four-point correlation, which decays according to a power-law behavior [224]. Intriguingly, this correlation exhibits a spatially anisotropic shape when shear deformation dominates the thermal dynamics of the particles [223].
Combined, these studies have provided an increased understanding of the plastic deformation of amorphous materials, where the mesoscopic response is governed by localized plastic events on the particle scale. Although these events do not correspond to a distinct topology and cannot be captured in terms of point-defects, they are reflected in distinct patterns of particle motion and structural rearrangement. Intriguingly, these localized patterns of deformation also induce anisotropic redistributions of the shear stress [221] or correspond to a local alteration of the potential energy landscape [180], the pressure [182] or the contact force distribution [181, 225] and may be traced by anisotropic dynamical correlations [223].

As summarized above, the plastic deformation of one-component crystalline solids and polycrystalline solids can be described and analyzed in terms of the formation and diffusion of well-defined topological defects. Throughout many years, the initial theoretical predictions and models on crystalline plasticity have been amended by large-scale computer simulations and elaborate experimental setups, providing a very exhaustive understanding of the connection between microscopic rearrangements and meso- or macroscopic material response. Also, the plastic deformation of amorphous solids has been thoroughly researched during the past decades. Many intriguing, non-Newtonian phenomena inherent to soft glassy materials such as the viscoplastic behavior of complex fluids with a finite yield

stress, nonlinear rheologic response like shear-thinning or -thickening and the emergence of spatial heterogeneities in the flow profile can be explained in terms of a microscopic understanding of amorphous plasticity, which was obtained by theoretical modeling and particle-resolved observation in computer simulations and experiments. Despite the absence of well-defined point defects, plastic events in amorphous media can be traced by distinct, localized patterns of particle motion, anisotropic stress redistributions in their vicinity and a spatial correlation of plastic events. While a complete, unified theoretical explanation of soft glassy rheology is still lacking, a broad range of phenomena emerging in the flow behavior of amorphous media is well understood.

Many solids which are encountered in nature or are manufactured artificially do, however, belong to a further distinction of solid materials, namely multicomponent crystals. While these are essentially crystals and exhibit the inherent high degree of translational and orientational order discussed above, the regular crystalline lattice is composed of more than one particular constituent, which may be of atomic, molecular or ionic nature [67]. Mixed crystals are ubiquitous in nature: The vast variety of stable chemical compounds of two or more chemical elements entails an array of crystalline structures, which are determined by the stoichiometry of the chemical compounds, the nature of the component binding - e.g. covalent, ionic or metallic binding - and the geometric packing of the components resulting from different sizes or interactions asymmetries [226]. Common examples of multicomponent crystals are *inorganic* compounds like sodium chloride or zinc sulfide, which are typically found in the form of solid minerals. Large portions of the earth's rocky surface consist of *organic* crystalline compound materials like calcium carbonate - porous networks of mixed crystalline organic materials may host reservoirs of shale gas and have attracted substantial scientifc and economic interest [227]. In the field of biology, the crystalline part of bone tissue, hydroxylapatite, may be named as a biological example for multicomponent crystalline materials [140, 204]. In general, organic compounds are a crucial contingency for life on planet earth, as carbon-based chemical compounds predominantly define the building-blocks of all known lifeforms. Specifically, this covers all instances of carbohydrates, e.g., cellulose. Furthermore, mixed crystals do also play a very prominent role in the engineering of artificial materials, such as metallic alloys [152, 228–235]. During the manufacturing process of metallic alloys, particles of one metallic element may be replaced by another element at some lattice sites and one refers to a substitutional alloy - examples include bronze or brass [236]. Also, alloys may host inclusions or precipitates of a several elements [230].
In all of these instances, the stability of multicomponent crystals may be compromised by mechanical stress - in various applications, shear deformation poses an elementary source of strain and it is therefore imperative to acquire a precise understanding of the behavior of mixed crystals under shear. So far, only very little is known about the shear-induced breaking process for mixed crystals. Specifically, a description of the early stage of the deformation process, i.e., the transition from elastic to plastic deformation under stress, is lacking. While the onset of plasticity has been elucidated for one-component crystals, polycrystals and amorphous materials during the past decades, only little effort has been devoted to the characterization of the shear-induced formation of structural defects in a mutlicomponent crystal, which ultimately triggers the macroscopic breakage of the mate-

rial. Colloids have proven to be an ideal model system for the observation of structural transitions on the particle scale and pose a favorable testing bed for the investigation of compound plasticity, as they allow to acquire particle-resolved data of the particle rearrangement during the deformation process and grant the accessibility of the problem in versatile experimental setups.

In the article "How does a thermal binary crystal break under shear?" [237], which constitutes the fourth part of this work, the shear-induced breaking of a binary, two-dimensional model crystal is explored in a computer simulation approach. The binary model crystal at hand is composed of equal numbers of particles from two particle species denoted as species A and B. The crystal particles are arranged in such a way that each species forms a square sublattice while the two sublattices are shifted relatively by half a lattice constant in each spatial direction. The resulting checkerboard pattern is known as the S(AB) structure [37]. This crystalline pattern is abundant in nature and may be encountered in granulates [238], ionic crystals [38,239] or dipolar colloidal suspensions [39,97,99]. The particle interaction is modeled corresponding to the soft, long-range repulsion of superparamagnetic particles, which are confined to a plane with induced dipole moments perpendicular to that plane. This setup can be recalled from experiments utilizing superparamagnetic colloidal particles to explore the two-dimensional melting scenario [74,95] or ultrafast quenching [97] and has been depicted above. The two species A and B have a high interaction asymmetry - corresponding to different magnetic susceptibilities in the experimental setup - with the A-particles being the more strongly coupled species.
Utilizing Brownian dynamics computer simulations, the onset of shear deformation in an initially pure, defect-free sample of the S(AB) binary model crystal is analyzed. The superposition of shear flow and thermal flucutations is found to induce an intriguing interplay between the two particle species, which indicates a hierarchical breaking scenario. The strained unit cell, in which a single, weakly coupled B particle is encased by four strongly coupled A particles, is further distorted by thermal fluctuations of either particle species. Specifically, aligned displacements of the A particles may distort the potential energy landscape encountered by the B particle in such a way that a pathway leading out of the unit cell is paved. The likelihood of this event is found to depend on the orientation of the crystalline lattice with respect to the direction of shear, and various distinct deformation modes are pointed out in [237] which induce the formation of such pathways in the energy landscape - following these, the thermally excited B particle can escape the distorted unit cell. This corresponds to an elemental plastic event in the binary crystal and induces the creation of a vacancy/interstitial pair in the material. An interstitial defect is constituted by two B particles occupying the same lattice site while a vacancy is, in the case of the S(AB) crystal, formed by four A particles encasing an empty B lattice site.
As opposed to the dislocations encounterd in one-component crystals, this topologic defect pair is very persistent and cannot be easily annihilated in this case. The presence of such a stable defect pair initiates a new stage of the deformation process: Being highly mobile, the interstitial defect diffuses throughout the crystalline lattice, where it stimulates the formation of further defects. The local lattice distortion induced in the vicinity of the traveling defect facilitates the escape of further B particles from their strained unit cell. In contrast, vacancies are strongly localized but are found to merge into larger, mechani-

cally unstable structures as more and more defects are proliferated and the global strain increases. Eventually, these defects form a band which spans the entire system - this band may be aligned parallel to the direction of shear or perpendicular to it. Intriguingly, the location of such a disordered region is crucially determined by the early occurrence of stable topological defects and can, in many cases, be directly traced back to an initial plastic event by which a stable vacancy was induced. Once a disordered band emerges, a mesoscopic breakage of the crystal can be observed, which is reflected by opposing nonaffine displacements on either side of the band. The presence of a persistent, disordered region in the sample allows for the release of strain via a nonaffine slip-motion of the entire crystal, which corresponds to a particle displacement on the order of one lattice constant. After this deformation, the particles in the disordered band rearrange such that the unstrained crystalline pattern is mostly restored. However, due to the stoichiometric composition of the unit cell, no complete restoration of the crystalline lattice can be achieved and typically, embedded defects remain. If the shear deformation is continued and strain increases, these defects predominantly determine the emergence of further band-like disordered regions. This shear-induced breaking process of a thermalized binary crystal is in distinct contrast to the plastic deformation of a one-component crystal. In the latter case, the material responds to internal and external perturbations via the spontaneous formation and annihilation of dislocations which, during their comparably short lifetime, initiate collective patterns of motion to release stress [164]. In contrast, the superposition of shear and thermal fluctuations induces persistent defects in the binary crystal which may have lifetimes of many Brownian times [237]. These defects cannot be easily annihilated and crucially determine the breaking of the crystal by merging into extended disordered regions, the like of which ar not observed in the plastic response of one-component crystals. The distinct creation pattern of vacancy/interstitial pairs is identified as an elemental plastic event, which, in the sheared, thermalized mixture crystal can be clearly distinguished from the destabilization of the crystal upon heating [237]. Reference computer simulations of the temperature-induced destabilization of the S(AB) crystal and the plastic deformation of a triangular crystal of species A under shear have been performed in [237] and support the finding that the shear-induced breaking of the S(AB) crystal poses a qualitatively different scenario.

However, the shear-induced deformation of the binary crystal observed in [237] bears a remarkable resemblance with the plasticity of amorphous media. Specifically, plastic events in the binary model crystal are found to induce a stress redistribution in their vicinity according to an anisotropic, fourfold pattern. This redistribution pattern qualitatively corresponds to recent findings in amorphous dispersions of polydisperse hard spheres under shear [240] and flowing emulsions close to the jamming point [181]. Additionally, an evaluation of the plastic events recorded in the simulation of the binary crystal under shear reveals a non-vanishing spatial correlation of plastic events. This correlation is most pronounced along the direction of shear and perpendicular to it, reflecting the emergence of defect bands in these directions as observed in the computer simulations. This observation conforms to recent findings on the plasticity of amorphous solids [223, 224], where an anisotropic spatial correlation of plastic events has been detected in computer simulations and experiments, agreeing with earlier theoretical predictions stated in Ref. [218].

These observations imply that the plastic response of a multicomponent crystal qualita-

tively resembles the plastic response of soft glassy materials in many aspects. In fact, the local creation of persistent structural defects which merge into expanded disordered regions corresponds to a local "amorphization" of the crystal - the stoichiometric constraints impeding the annihilation of defects render these defective bands into vitreous regions, the presence of which enables a mesoscopic rearrangement of the crystal via large nonaffine displacements.
These results provide novel insights relevant for the study of solid plasticity: While crystalline and amorphous media are generally understood as qualitatively different materials with respect to the mechanisms governing plastic deformation in the presence of shear, this qualitative difference does not fully apply when a multicomponent crystal is considered. Even in the simple case of an equimolar binary crystal, the plastic response strongly deviates from the dislocation-mediated plasticity of a one-component crystal and exhibits characteristics of vitreous media.

The scientific efforts of the past decades have substantially raised our understanding of freezing and melting processes. In particular, the case of two-dimensional melting has incited a vital debate which promoted the insight that changes in the system geometry or the particle interaction qualitatively affect the mechanism by which freezing and melting is governed. The thesis at hand contains an examination of the two-dimensional melting process in the presence of frozen-in obstacles - via a particle-resolved analysis of data obtained by computer simulation and experiments on superparamagnetic colloidal particles, the controversial KTHNY melting scenario could be confirmed in the presence of quenched disorder and the long-standing theoretical prediction of a broadening of the hexatic phase [117] has been explicitly shown. It would be interesting to expand this examination to the case of long-range quenched potentials, which Nelson considered in his original treatment of melting in the presence of quenched disorder [117]. Also, a systematic study of further types of disorder would increase our understanding of disorder-induced melting - this may include short-range disorder or disorder which is not frozen-in on the timescale of the observation. Addressing the shear-induced destabilization of a binary model crystal via computer simulations, a novel shear-induced melting mechanism has been detected, which, intriguingly, is in marked contrast to the melting of a one-component crstal. Moreover, the shear-induced breaking process of the binary model crystal implies a qualitative similarity between the plastic response of mixed crystals and that of vitreous materials. The results presented in [237] can be verified in experimental setups similar to those proposed in [74, 95, 97, 98, 132, 134], where superparamagnetic particles are suspended in a hanging droplet or dipersed on a planar surface in an external magnetic field. Couette shear flow can be imposed by an external laser field [28]. Through real-space imaging techniques like confocal microscopy, the hierarchical breaking scenario predicted in [237] could be verified on the particle scale. It would be promising to address shear-induced breaking at small damping as could be explored in computer simulations and experiments on dusty plasmas [11, 146]. In order to systematically study the plastic response of multicomponent crystals, more interaction asymmetries, composition ratios and model potentials need to be explored. The study of the shear-induced breaking of binary crystals could also be explored in 3D, where a wealth of binary colloidal crystals can be assessed [241].

Bibliography

[1] D. J. Z. (trans.), *Plato: Timaeus* (Hacklet Publishing Co., Indianapolis and Cambridge, Mass, 2000).

[2] J. W. Gibbs, *Elementary Principles in Statistical Mechanics* (Charles Scribner's Sons, New York, 1902).

[3] E. A. Guggenheim, *Modern Thermodynamics by the Methods of J. W. Gibbs* (Methuen, London, 1933).

[4] For a detailed collection of everyday-life applications of thermodynamics, see: http://www.brighthubengineering.com/thermodynamics/38344-thermodynamics-integral-part-of-our-life/ (Jan 2015).

[5] *Understanding Moore's law : four decades of innovation*, edited by D. C. Brock (Chemical Heritage Press, Philadelphia, Pa, 2006).

[6] J. W. Morris, Lecture on Material Science held at the University of California, Berkeley, 2015, chapter 4: Defects in Solids, http://www.mse.berkeley.edu/groups/morris/MSE205/Extras/defects.pdf.

[7] W. Heisenberg, Zeitschrift für Physik **43**, 172 (1927).

[8] K. Zahn and G. Maret, Curr. Opin. Colloid Interface Sci. **4**, 60 (1999).

[9] M. Doi, *Soft Matter Physics* (Oxford University Press, Oxford, 2013).

[10] P. Pusey, in: *Colloidal Suspensions*, edited by J. P. Hansen, D. Levesque, and J. Zinn-Justin (North-Holland, Amsterdam, 1989).

[11] A. V. Ivlev, H. Löwen, G. E. Morfill, and C. P. Royall, *Complex plasmas and colloidal dispersions: particle-resolved studies of classical liquids and solids - Series in Soft Condensed Matter* (World Scientific, London, 2012), Vol. 5.

[12] V. Prasad, D. Semwogerere, and E. R. Weeks, J. Phys.: Condens. Matter **19**, 113102 (2007).

[13] B. V. R. Tata and B. Raj, Bull. Mater. Sci. **21**, 263 (1998).

[14] B. Kainz, E. A. Oprzeska-Zingrebe, and J. L. Toca-Herrera, Biotechnol. J. **9**, 51 (2014).

[15] C. A. Murray and D. H. Van Winkle, Phys. Rev. Lett. **58**, 1200 (1987).

[16] M. Ballauff, Curr. Opin. Colloid Interface Sci. **6**, 132 (2001).

[17] R. Sigel, Curr. Opin. Colloid Interface Sci. **14**, 426 (2009).

[18] P. Schall, I. Cohen, D. A. Weitz, and F. Spaepen, Nature **440**, 319 (2006).

[19] P. N. Pusey and W. Megan, Nature **320**, 340 (1986).

[20] S. Asakura and F. Oosawa, J. Polym. Sci. **33**, 183 (1958).

[21] D. Wilms, S. Deutschländer, U. Siems, K. Franzrahe, P. Henseler, P. Keim, N. Schwierz, P. Virnau, K. Binder, G. Maret, and P. Nielaba, J. Phys.: Condens. Matter **24**, 464119 (2012).

[22] V. A. Froltsov, C. N. Likos, H. Löwen, C. Eisenmann, U. Gasser, P. Keim, and G. Maret, Phys. Rev. E **71**, 031404 (2005).

[23] P. Tierno, Phys. Rev. Lett. **109**, 198304 (2012).

[24] K. Zahn, J. M. Mendez, and G. Maret, Phys. Rev. Lett. **79**, 175 (1997).

[25] K. Zahn, R. Lenke, and G. Maret, Phys. Rev. Lett. **82**, 2721 (1999).

[26] N. Hoffmann, F. Ebert, C. N. Likos, H. Löwen, G. Maret, R. Klein, and J. K. G. Dhont, Phys. Rev. Lett. **97**, 078301 (2006).

[27] F. Ebert, P. Dillmann, G. Maret, and P. Keim, Rev. Sci. Instrum. **80**, 083902 (2009).

[28] A. Ashkin, Phys. Rev. Lett. **24**, 156 (1970).

[29] A. Ashkin, J. Dziedzic, J. Bjorkholm, and S. Chu, Opt. Lett. **11**, 288 (1986).

[30] K. C. Neuman and S. M. Block, Rev. Sci. Instrum. **75**, 2787 (2004).

[31] I. Williams, E. C. Oğuz, R. L. Jack, P. Bartlett, H. Löwen, and C. P. Royall, J. Chem. Phys. **140**, 104907 (2014).

[32] J. W. Swan, R. N. Zia, and J. F. Brady, J. Rheol. **58**, 1 (2014).

[33] J. Zhao, P. Papadopoulos, M. Roth, C. Dobbrow, E. Roeben, A. Schmidt, H.-J. Butt, G. Auernhammer, and D. Vollmer, Eur. Phys. J. - Special Topics **222**, 2881 (2013).

[34] A. Pertsinidis and X. S. Ling, Phys. Rev. Lett. **100**, 028303 (2008).

[35] M. Rex, H. Löwen, and C. N. Likos, Phys. Rev. E **72**, 021404 (2005).

[36] P. Schall and M. van Hecke, Annu. Rev. Fluid Mech. **42**, 67 (2010).

[37] L. Assoud, R. Messina, and H. Löwen, Europhys. Lett. **80**, 48001 (2007).

[38] L. Assoud, R. Messina, and H. Löwen, J. Chem. Phys. **129**, 164511 (2008).

[39] L. Assoud, R. Messina, and H. Löwen, Mol. Phys. **109**, 1385 (2011).

[40] T. Biben and J.-P. Hansen, Mol. Phys. **80**, 853 (1993).

[41] W. Nuesser and H. Versmold, Mol. Phys. **96**, 893 (1999).

[42] A. Esztermann and H. Löwen, Europhys. Lett. **68**, 120 (2004).

[43] K. Milinković, J. T. Padding, and M. Dijkstra, Soft Matter **7**, 11177 (2011).

[44] A. Rosato, K. J. Strandburg, F. Prinz, and R. H. Swendsen, Phys. Rev. Lett. **58**, 1038 (1987).

[45] T. Kruppa, T. Neuhaus, R. Messina, and H. Löwen, J. Chem. Phys. **136**, 134106 (2012).

[46] D. Semwogerere and E. R. Weeks, Phys. Fluids **20**, 043306 (2008).

[47] F. Varnik, L. Bocquet, J.-L. Barrat, and L. Berthier, Phys. Rev. Lett. **90**, 095702 (2003).

[48] J. Zausch and J. Horbach, Europhys. Lett. **88**, 60001 (2009).

[49] K. Kim, K. Miyazaki, and S. Saito, Eur. Phys. J. Special Topics **189**, 135 (2010).

[50] K. Kim, K. Miyazaki, and S. Saito, J. Phys.: Condens. Matter **23**, 234123 (2011).

[51] Y. Saito and H. Muller-Krumbhaar, in: *Applications of the Monte Carlo Method in Statistical Physics*, edited by K. Binder (Springer, New York, 1984).

[52] K. Binder, in: *Monte Carlo Methods in Statistical Physics*, edited by K. Binder (Springer, Berlin, 1986).

[53] K. Binder, Rep. Prog. Phys. **60**, 487 (1997).

[54] K. Binder, J. Horbach, W. Kob, W. Paul, and F. Varnik, J. Phys.: Condens. Matter **16**, S429 (2004).

[55] D. J. Evans and G. P. Morriss, Phys. Rev. Lett. **51**, 1776 (1983).

[56] D. M. Heyes, Phys. Lett. A **132**, 399 (1988).

[57] H. Löwen, J. Phys.: Condens. Matter **4**, 10105 (1992).

[58] M. P. Allen and D. J. Tildesley, *Computer Simulations of Liquids* (Oxford Science Publications, Clarendon Press, Oxford, 1987).

[59] E. P. Bernard and W. Krauth, Phys. Rev. Lett. **107**, 155704 (2011).

[60] H. Weber, D. Marx, and K. Binder, Phys. Rev. B **51**, 14636 (1995).

[61] R. Piazza, *Soft Matter: The stuff that dreams are made of* (Copernicus, Amsterdam, 2011).

[62] F. Ramos, C. López, E. Hernández-García, and A. Muñoz, Phys. Rev. E **77**, 021102 (2008).

[63] M. C. Marchetti, J. F. Joanny, S. Ramaswamy, T. B. Liverpool, J. Prost, M. Rao, and R. Aditi Simha, Soft Active Matter, http://arxiv.org/pdf/1207.2929v1.pdf (unpublished).

[64] S. Blundell and K. M. Blundell, *Concepts in Thermal Physics* (Oxford University Press, Oxford, 2008).

[65] A. Onuki, *Phase Transition Dynamics* (Cambridge University Press, Cambridge, 2002).

[66] K. J. Strandburg, Rev. Mod. Phys. **60**, 161 (1988).

[67] P. M. Chaikin and T. C. Lubensky, *Principles of Condensed Matter Physics* (Cambridge Univesity Press, Cambridge, 1995).

[68] N. D. Mermin and H. Wagner, Phys. Rev. Lett. **17**, 1133 (1966).

[69] D. J. Bishop and J. D. Reppy, Phys. Rev. Lett. **40**, 1727 (1978).

[70] H. J. Jensen, A. Brass, and A. J. Berlinsky, Phys. Rev. Lett. **60**, 1676 (1988).

[71] M. J. Gingras and D. A. Huse, Phys. Rev. B Condens. Matter **22**, 15193 (1996).

[72] J. M. Kosterlitz and D. J. Thouless, J. Phys. C **6**, 1181 (1973).

[73] J. M. Kosterlitz and D. J. Thouless, in: *Progress in Low Temperature Physics*, edited by D. F. Brewer (North-Holland, Amsterdam, 1983).

[74] P. Keim, G. Maret, and H. H. von Grünberg, Phys. Rev. E **75**, 031402 (2007).

[75] N. D. Mermin, Phys. Rev. **176**, 250 (1968).

[76] *Bond-Orientational Order in Condensed Matter Systems*, edited by K. J. Strandburg (Springer, Berlin, 1992).

[77] B. Halperin and D. R. Nelson, Phys. Rev. Lett. **41**, 121 (1978).

[78] D. R. Nelson and B. Halperin, Phys. Rev. B **19**, 2457 (1979).

[79] A. P. Young, Phys. Rev. B **19**, 1855 4 (1979).

[80] T. M. Liebling and L. Pournin, Documenta Math. **Extra Volume ISMP**, 419 (2012).

[81] D. S. Fisher, B. Halperin, and R. Morf, Phys. Rev. B **20**, 4692 (1979).

[82] S. T. Chui, Phys. Rev. Lett. **48**, 933 (1982).

[83] S. T. Chui, Phys. Rev. B **28**, 178 (1983).

[84] M. A. Glaser and N. A. Clark, Adv. Chem. Phys. **83**, 543 (1993).

[85] D. R. Nelson, in: *Phase Transition and Critical Phenomena*, edited by C. Domb and J. L. Lebowitz (Academic Press, New York, 1983).

[86] H. Kleinert, *Gauge Fields in Condensed Matter* (World Scientific, Singapore, 1989).

[87] Y. Saito, Phys. Rev. Lett. **48**, 1114 (1982).

[88] K. J. Strandburg, J. A. Zollweg, and G. V. Chester, Phys. Rev. B **30**, 2755 (1984).

[89] J. A. Zollweg, G. V. Chester, and P. W. Leung, Phys. Rev. B **39**, 9518 (1989).

[90] J. Lee and K. J. Strandburg, Phys. Rev. B **46**, 11190 (1992).

[91] V. N. Ryzhov and E. E. Tareyeva, Phys. Rev. B **51**, 8789 (1995).

[92] A. Jaster, Europhys. Lett. **42**, 277 3 (1998).

[93] R. E. Kusner, J. A. Mann, and A. J. Dahm, Phys. Rev. B **49**, 9190 (1994).

[94] R. Seshadri and R. Westervelt, Phys. Rev. Lett. **66**, 2774 (1991).

[95] K. Zahn and G. Maret, Phys. Rev. Lett. **85**, 3656 (2000).

[96] S. Z. Lin, B. Zheng, and S. Trimper, Phys. Rev. E **73**, 066106 (2006).

[97] L. Assoud, F. Ebert, P. Keim, R. Messina, G. Maret, and H. Löwen, Phys. Rev. Lett. **102**, 238301 (2009).

[98] P. Dillmann, G. Maret, and P. Keim, J. Phys.: Condens. Matter **20**, 404216 (2008).

[99] L. Assoud, F. Ebert, P. Keim, R. Messina, G. Maret, and H. Löwen, J. Phys.: Condens. Mat. **21**, 464114 (2009).

[100] P. Yunker, Z. Zhang, and A. G. Yodh, Phys. Rev. Lett. **104**, 015701 (2010).

[101] A. H. Marcus and S. A. Rice, Phys. Rev. Lett. **77**, 257712 (1996).

[102] A. H. Marcus and S. A. Rice, Phys. Rev. B **55**, 637 (1997).

[103] S. C. Kapfer and W. Krauth, Soft-disk melting: From liquid-hexatic coexistence to continuous transitions, http://arxiv.org/abs/1406.7224. (unpublished).

[104] S. C. Kapfer and W. Krauth, Two-Step Melting in Two Dimensions: First-Order Liquid-Hexatic Transition, accepted in Phys. Rev. Lett. (unpublished).

[105] D. E. Dudalov, Y. D. Fomin, E. N. Tsiok, and V. N. Ryzhov, Effect of a potential softness on the solid-liquid transition in a two-dimensional core-softened potential system, arXiv: 1407.3989v1 (unpublished).

[106] N. Gribova, A. Arnold, T. Schilling, and C. Holm, J. Chem. Phys. **135**, 054514 (2011).

[107] J. Schockmel, E. Mersch, N. Vandewalle, and G. Lumay, Phys. Rev. E **87**, 062201 (2013).

[108] P. Hartmann, A. Douglass, J. C. Reyes, L. S. Mattews, T. W. Hyde, A. Kovacs, and Z. Donko, Phys. Rev. Lett. **105**, 115004 (2010).

[109] J. C. Meyer, A. K. Geim, M. I. Katsnelson, K. S. Novoselov, T. J. Booth, and S. Roth, Nature (London) **446**, 60 (2007).

[110] A. I. Larkin, Sov. Phys. JETP **31**, 784 (1970).

[111] Y. Imry and S.-K. Ma, Phys. Rev. Lett. **35**, 1399 (1975).

[112] A. I. Larkin and Y. N. Ovchinnikov, J. Low Temp. Phys. **34**, 409 (1979).

[113] R. Geer, T. Stoebe, C. C. Huang, R. Pindak, J. W. Goodby, M. Cheng, J. T. Ho, and S. W. Hui, Nature **355**, 152 (1992).

[114] R. Viswanathan, L. L. Madsen, J. A. Zasadzinski, and D. K. Schwartz, Science **269**, 51 (1995).

[115] I. R. Peterson, R. Steitz, H. Krug, and I. Voigt-Martin, J. Phys. (France) **51**, 1003 (1990).

[116] B. Berge, L. Faucheux, K. Schwab, and A. Libchaber, Nature (London) **350**, 322 (1991).

[117] D. R. Nelson, Phys. Rev. B **27**, 2902 (1983).

[118] S. Sachdev and D. R. Nelson, J. Phys. C: Solid State Physics **17**, 5473 (1984).

[119] E. M. Chudnovsky, Phys. Rev. B **33**, 245 (1986).

[120] A.-C. Shi and A. J. Berlinsky, Phys. Rev. B **47**, 653 2 (1993).

[121] R. A. Serota, Phys. Rev. B **33**, 3403 (1986).

[122] M.-C. Cha and H. A. Fertig, Phys. Rev. Lett. **74**, 4867 24 (1995).

[123] S. Herrera-Velarde and H. H. von Grünberg, Soft Matter **5**, 391 (2009).

[124] Z.-X. Cai, S. Sen, and D. O. Welch, Phys. Rev. B **51**, 15873 (1995).

[125] D. Carpentier and P. Le Doussal, Phys. Rev. Lett. **81**, 1881 (1998).

[126] T. Kawasaki and H. Tanaka, J. Phys.: Condens. Matter **23**, 194121 (2011).

[127] C. J. Olson Reichhardt, E. Groopman, Z. Nussinov, and C. Reichhardt, Phys. Rev. E **86**, 061301 (2012).

[128] J. Ma, E. D. Carter, and H. B. Kleinberg, Phys. Rev. B **57**, 9270 15 (1998).

[129] L. Chen and M. W. Deem, Phys. Rev. Lett. **68**, 021107 (2003).

[130] Y. G. Cao, Z. F. Zhang, M. H. Zhao, G. Y. Fu, and D. X. Ouyang, Physica A **391**, 2940 (2012).

[131] Z. F. Zhang, Y. Q. Dong, and Y. G. Cao, Comm. Theor. Phys. **57**, 320 (2012).

[132] S. Deutschländer, T. Horn, H. Löwen, G. Maret, and P. Keim, Phys. Rev. Lett **111**, 098301 (2013).

[133] H. Shiba, A. Onuki, and T. Araki, Europhys. Lett. **86**, 66004 (2009).

[134] T. Horn, S. Deutschländer, H. Löwen, G. Maret, and P. Keim, Phys. Rev. E **88**, 062305 (2013).

[135] H. Löwen, T. Horn, T. Neuhaus, and B. ten Hagen, Eur. Phys. J. Special Topics **222**, 2961 (2013).

[136] J. P. Hirth and J. Lothe, *Theory of Dislocations* (Wiley, New York, 1982).

[137] F. Brau, Tearing of thin sheets: Cracks interacting through an elastic ridge, http://arxiv.org/abs/1409.0450 (unpublished).

[138] S.-B. Shim, K. Ahn, J. C. Seferis, A. J. Berg, and W. Hudson, J. Adv. Materials **26**, 48 (1995).

[139] N. D. Alexopoulos, E. Miklis, A. Stylianos, and D. P. Myriounis, Int. J. Fatigue **56**, 95 (2013).

[140] X. Guo, L. C. Liang, and S. A. Goldstein, J. Biomech. Engineering **120**, 112 (1998).

[141] A. R. Najafi, A. R. Arshi, M. R. Eslami, S. Fariborz, and M. H. Moeninzadeh, J. Biomech. **40**, 2788 (2007).

[142] L. B. Freund, *Dynamic fracture mechanics* (Cambridge University Press, Cambridge, 1990).

[143] J. Friedel, *Dislocations* (Pergamon, Oxford, 1964).

[144] R. W. Whorlow, *Rheological techniques* (Ellis Horwood Ltd., Chichester, 1980).

[145] J. P. Sethna, K. A. Dahmen, and C. R. Meyers, Nature (London) **410**, 242 (2001).

[146] C. Yang and L. I, Phys. Rev. E **89**, 041102(R) (2014).

[147] T. Hamanaka, H. Shiba, and A. Onuki, Phys. Rev. E **77**, 042501 (2008).

[148] H. Shiba and A. Onuki, Phys. Rev. E **81**, 051501 (2010).

[149] D. M. Dimiduk, C. Woodward, R. LeSar, and M. D. Uchic, Science **312**, 1188 (2006).

[150] Y. L. Wu, D. Derks, A. van Blaaderen, and A. Imhof, Proc. Natl. Acad. Sci. USA **106**, 10564 (2009).

[151] H.-G. Kim, Y.-H. Kim, B.-K. Choi, and Y.-H. Jeong, J. Nuc. Mat. **359**, 268 (2006).

[152] Y. Mishin, J. A. Warren, R. F. Sekerka, and W. J. Boettinger, Phys. Rev. B. **88**, 184303 (2013).

[153] D. J. Evans, Phys. Rev. A **25**, 2788 (1981).

[154] B. J. Ackerson and N. A. Clark, Phys. Rev. Lett. **46**, 1123 (1981).

[155] H. M. Lindsay and P. M. Chaikin, J. Phys. (Paris) Colloque **46-C3**, 269 (1985).

[156] S. Butler and P. Harrowell, J. Chem. Phys. **103**, 4653 (1995).

[157] A. D. Gopal and D. J. Durian, J. Colloid Interface Sci. **213**, 169 (1999).

[158] D. Derks, Y. L. Wu, A. van Blaaderen, and A. Imhof, Soft Matter **5**, 1060 (2009).

[159] N. A. Clark and B. J. Ackerson, Phys. Rev. Lett. **44**, 1005 (1980).

[160] R. G. Larson, *The Structure and Rheology of Complex Fluids* (Oxford Univerity Press, New York, 1999).

[161] H. Löwen, R. Messina, N. Hoffmann, C. N. Likos, C. E. an P. Keim, U. Gasser, G. Maret, R. Goldberg, and T. Palberg, J. Phys.: Condens. Matter **17**, S3379 (2005).

[162] S. Butler and P. Harrowell, J. Chem. Phys. **118**, 4115 (2003).

[163] J. D. Kiely, K. F. Jarausch, J. E. Houston, and P. E. Russell, J. Mater. Res. **14**, 2219 (1999).

[164] B. van der Meer, W. Qi, R. Fokkink, J. van der Gucht, M. Dijkstra, and J. Sprakel, Proc. Natl. Acad. Sci. USA 15356 (2014).

[165] J. A. Erwing and W. Rosenhain, Philos. Trans. R. Soc. London Ser. A **193**, 353 (1900).

[166] A. H. Cottrell, *Dislocations and Plastic Flow in Crystals* (Oxford University Press, Oxford, 1956).

[167] J. J. Gilman, *Micromechanics of Flow in Solids* (McGraw-Hill, New York, 1969).

[168] H. Neuhauser, *Dislocations in Solids* (North-Holland, Amsterdam, 1983).

[169] B. Devincre and L. P. Kubin, Mater. Sci. Eng. **A234-236**, 8 (1997).

[170] C. L. Kelchner, S. J. Plimpton, and J. C. Hamilton, Phys. Rev. B. **58**, 11085 (1998).

[171] E. T. Lilleodden, J. A. Zimmermann, S. M. Foiles, and W. D. Nix, J. Mech. Phys. Sol. **51**, 901 (2003).

[172] M.-C. Miguel, A. Vespignani, S. Zapperl, J. Weiss, and J.-R. Grasso, Nature **410**, 667 (2001).

[173] V. Bulatov, F. Abraham, L. Kubin, B. Devincre, and S. Yip, Nature **391**, 669 (1998).

[174] T. Richeton, J. Weiss, and F. Louchet, Nature Mat. **4**, 465 (2005).

[175] J. Weiss and D. Marsan, Science **299**, 89 (2003).

[176] I. Groma and G. S. Pawley, Phil. Mag. A **67**, 1459 (1983).

[177] R. Fournet and J. M. Salazar, Phys. Rev. B **53**, 6283 (1996).

[178] M. Koslowski, R. LeSar, and R. Thomson, Phys. Rev. Lett. **93**, 125502 (2004).

[179] M.-C. Miguel, P. Moretti, M. Zaiser, and S. Zapperi, Mater Sci. Eng. A **400-401**, 191 (2005).

[180] C. E. Maloney and A. Lemaître, Phys. Rev. E. **74**, 016118 (2006).

[181] K. W. Desmond and E. R. Weeks, Experimental measurements of stress redistribution in flowing emulsions, http://arxiv.org/abs/1306.0269 (unpublished).

[182] K. Maeda and S. Takeuchi, Phil. Mag. A **44**, 643 (1981).

[183] T. Sentjabrskaja, E. Babaliari, J. Hendricks, M. Laurati, G. Petekidis, and S. U. Egelhaaf, Soft Matter **9**, 4524 (2013).

[184] F. Varnik, L. Bocquet, and J.-L. Barrat, J. Chem. Phys. **120**, 2788 (2004).

[185] L. Berthier and J.-L. Barrat, J. Chem. Phys. **116**, 6228 (2002).

[186] G. Picard, A. Ajdari, F. Lequeux, and L. Bocquet, Phys. Rev. E **71**, 010501 (2005).

[187] W. J. Frith, P. d'Haene, R. Buscall, and J. Mewis, J. Rheol. **40**, 531 (1996).

[188] R. Besseling, E. R. Weeks, A. B. Schofield, and W. C. K. Poon, Phys. Rev. Lett. **99**, 028301 (2007).

[189] A. Fall, F. Bertrand, G. Ovarlez, and D. Bonn, Shear Thickening of Cornstarch Suspensions, http://arxiv.org/pdf/1206.1717.pdf (unpublished).

[190] http://science.howstuffworks.com/liquid-body-armor1.htm (Jan 2015).

[191] For a popular scientific review on the flow properties of ketchup, see: http://www.firstscience.com/SITE/ARTICLES/ketchup.asp (Jan 2015).

[192] K. Van Dyke, *Drilling Fluids, Mud Pumps, and Conditioning Equipment* (The University of Texas at Austin - Petroleum Extension Service, Austin, 1998).

[193] A. W. Lees and S. F. Edwards, J. Phys. C.: Solid State Phys **5**, 1921 (1972).

[194] D. J. Evans and G. P. Morriss, Phys. Rev. A **30**, 1528 (1984).

[195] D. J. Evans, Phys. Lett. **74A**, 229 (1979).

[196] D. J. Evans, Phys. Rev. A **22**, 290 (1980).

[197] D. J. Evans, Mol. Phys. **47**, 1165 (1982).

[198] D. M. Heyes, G. P. Morriss, and D. J. Evans, J. Chem. Phys. **83**, 4760 (1985).

[199] D. M. Heyes, P. J. Mitchell, P. B. Visscher, and J. R. Melrose, J. Chem. Soc. Faraday Trans. **90**, 1133 (1994).

[200] G. Ovarlez, S. Rodts, X. Chateau, and P.Coussot, Rheol. Acta **48**, 831 (2009).

[201] P. Coussot, *Rheometry of Pastes, Suspensions and Granular Materials* (Wiley, New York, 2005).

[202] L. B. Chen, C. F. Zukoski, B. J. Ackerson, H. J. M. Hanley, and G. C. Straty, Phys. Rev. Lett. **69**, 688 (1992).

[203] J. K. G. Dhont, M. P. Lettinga, Z. Dogic, T. A. J. Lenstra, and H. Wang, Faraday Discuss. **123**, 157 (2003).

[204] T. Divioux, D. Tamarii, C. Barentin, and S. Manneville, Phys. Rev. Lett. **104**, 208301 (2010).

[205] P. Sollich, F. Lequeux, P. Hébraud, and M. E. Cates, Phys. Rev. Lett. **78**, 2020 (1997).

[206] S. M. Fielding, P. Sollich, and M. E. Cates, J. Rheol. **44**, 323 (2000).

[207] L. Berthier, J.-L. Barrat, and J. Kurchan, Phys. Rev. E **61**, 5464 (2000).

[208] J.-L. Barrat and L. Berthier, Phys. Rev. E **63**, 012503 (2000).

[209] L. Berthier and J.-L. Barrat, Phys. Rev. Lett. **89**, 095702 (2002).

[210] J.-C. Baret, D. Vandembroucq, and S. Roux, Phys. Rev. Lett. **89**, 195506 (2002).

[211] P. Chaudhuri, L. Berthier, and L. Bocquet, Phys. Rev. E **85**, 021503 (2012).

[212] R. L. Moorcroft, M. E. Cates, and S. M. Fielding, Phys. Rev. Lett. **106**, 055502 (2011).

[213] J. S. Myung, S. Song, and K. H. Ahn, J. Non-Newtonian Fluid Mech. **199**, 29 (2013).

[214] J. Park, Y. Shibutani, M. Wakeda, and S. Ogata, Mat. Transactions **48**, 1001 (2007).

[215] A. S. Argon and L. T. Shi, Philos. Mag. A **46**, 275 (1982).

[216] H. M. Princen, J. Colloid Interface Sci. **91**, 160 (1983).

[217] D. Chen, K. W. Desmond, and E. R. Weeks, Soft Matter **8**, 10486 (2012).

[218] A. S. Argon, Acta Metall. **27**, 47 (1979).

[219] M. L. Falk and J. S. Langer, Phys. Rev. E. **57**, 7192 (1998).

[220] Y. Shi and M. L. Falk, Phys. Rev. Lett. **95**, 095502 (2005).

[221] A. Tanguy, F. Leonforte, and J.-L. Barrat, Eur. Phys. J. E **20**, 355 (2006).

[222] P. Schall, D. A. Weitz, and F. Spaepen, Science **318**, 1895 (2007).

[223] S. Mandal, V. Chikkadi, B. Nienhuis, D. Raabe, P. Schall, and F. Varnik, Phys. Rev. E **88**, 022129 (2013).

[224] F. Varnik, S. Mandal, V. Chikkadi, D. Denisov, P. Olsson, D. Vågberg, D. Raabe, and P. Schall, Phys. Rev. E **89**, 040301 (2014).

[225] J. Boberski, M. R. Shaebani, and D. E. Wolf, Europhys. Lett. **108**, 44002 (2014).

[226] L. E. Moore and A. Elaine, *Solid state chemistry : an introduction* (Taylor & Francis, CRC, Boca Raton, Fla, 2005).

[227] D. J. K. Ross and R. M. Bustin, Marine and Petroleum Geology **26**, 916 (2009).

[228] V. Fallah, J. Stolle, N. Ofori-Opoku, S. Esmaeili, and N. Provatas, Phys. Rev. B **86**, 134112 (2012).

[229] V. Fallah, A. Korinek, N. Ofori-Opoku, N. Provatas, and S. Esmaeili, Acta Mater **61**, 6372 (2013).

[230] L. Rougier, A. Jacot, C.-A. Gandin, P. Di Napoli, P.-Y. Théry, D. Ponsen, and V. Jaquet, Acta Mater. **61**, 6396 (2013).

[231] F. Sun, J. Y. Zhang, M. Marteleur, T. Gloriant, P. Vermaut, D. Laillé, P. Castany, C. Curfs, P. J. Jacues, and F. Prima, Acta Mater. **61**, 6406 (2013).

[232] S. M. Hafez Haghighat, R. Schäublin, and D. Raabe, Acta Mater. **64**, 24 (2014).

[233] H. Matsumoto, Y. Koizumi, T. Ohashi, B.-S. Lee, Y. Li, and A. Chiba, Acta Mater. **64**, 1 (2014).

[234] T. Iwai, J. Phys. Soc. Japan **68**, 3717 (1999).

[235] H.-C. Yu, D.-H. Yeon, A. Van der Ven, and K. Thornton, Acta Mater. **55**, 6690 (2007).

[236] *Elements of Metallurgy and Engineering Alloys*, edited by F. Campbell (ASM Intl., Materials Park, OH, 2008).

[237] T. Horn and H. Löwen, J. Chem. Phys. **141**, 224505 (2014).

[238] G. K. Kaufman, M. Reches, S. W. Thomas, J. Feng, B. F. Shaw, and G. M. Whitesides, Appl. Phys. Lett. **94**, 044102 (2009).

[239] L. Assoud, R. Messina, and H. Löwen, Europhys. Lett. **89**, 36001 (2010).

[240] S. Mandal, private communication (2014).

[241] P. Bartlett, R. H. Ottewill, and P. N. Pusey, Phys. Rev. Lett. **68**, 3801 (1992).

Two-Dimensional Melting under Quenched Disorder

Sven Deutschländer,[1] Tobias Horn,[2] Hartmut Löwen,[2] Georg Maret,[1] and Peter Keim[1]
[1]*Fachbereich für Physik, Universität Konstanz, D-78464 Konstanz, Germany*
[2]*Institut für Theoretische Physik II: Heinrich-Heine-Universität Düsseldorf, D-40225 Düsseldorf, Germany*
(Received 10 May 2013; published 27 August 2013)

We study the influence of quenched disorder on the two-dimensional melting behavior of superparamagnetic colloidal particles, using both video microscopy and computer simulations of repulsive parallel dipoles. Quenched disorder is introduced by pinning a fraction of the particles to an underlying substrate. We confirm the occurrence of the Kosterlitz-Thouless-Halperin-Nelson-Young scenario and observe an intermediate hexatic phase. While the fluid-hexatic transition remains largely unaffected by disorder, the hexatic-solid transition shifts to lower temperatures with increasing disorder. This results in a significantly broadened stability range of the hexatic phase. In addition, we observe spatiotemporal critical (like) fluctuations, which are consistent with the continuous character of the phase transitions. Characteristics of first-order transitions are not observed.

DOI: 10.1103/PhysRevLett.111.098301 PACS numbers: 82.70.Dd, 61.20.Ja, 64.70.D−, 64.70.pv

Since the seminal work of Kosterlitz, Thouless [1,2], Halperin, Nelson, and Young (KTHNY) [3–5] it has been known that melting in two spatial dimensions can be qualitatively different from three-dimensional bulk melting. While the latter is typically a phase transition of first order, a two-stage scenario with an intervening hexatic phase can emerge in two-dimensional systems, which is separated from the isotropic fluid and solid phase by two continuous transitions [6]. The KTHNY melting scenario further predicts that, in two dimensions, the melting process is mediated by the unbinding of thermally activated topological defects. In particular, the emergence of the hexatic phase is related to the dissociation of dislocation pairs into isolated dislocations [2,7]. These break translational symmetry, leading to a vanishing shear modulus. However, the orientational symmetry remains quasi long range and the modulus of rotational stiffness, Frank's constant K_A, attains a nonvanishing value [4]. It has been shown that the KTHNY scenario is realized for soft long-range pairwise potentials scaling with the inverse cube of the particle separation [8,9]. In fact, video microscopy experiments with superparamagnetic colloidal particles pending at a two-dimensional air-water interface and exposed to an external magnetic field perpendicular to the interface have confirmed the KTHNY scenario in detail [10–12]. Further reports on soft repulsive particles in two dimensions are in favor of the KTHNY scenario [13–15] while in systems with very short-ranged or hard-core particle interactions, first-order characteristics were found for both transitions [16,17]. Here, we investigate whether the continuous melting including critical fluctuations persists in the presence of quenched disorder or whether first-order signatures emerge instead [18].

Pure 2D bulk systems are rare in nature; planar confinement is typically realized by adsorption on an interface, such that crystallization usually occurs on solid substrates (examples include graphene sheets, see Ref. [19]) which introduce quenched (i.e., frozen-in) disorder due to some roughness. The same holds for flux lines pinned by impurities [20–23], which leads to large critical fields in type II superconductors. Defects may also affect the phase behavior of freely suspended liquid crystal films [24], of synthetic [25] and biological [26] Langmuir Blodgett films, or even 2D protein crystals [27]. Based on a topological defect analysis for weak disorder, Nelson and co-workers [28,29] have predicted that the KTHNY scenario persists with a widening of the hexatic stability range for increasing strength of quenched disorder. This notion was questioned in subsequent theoretical studies [30]. More recent experimental efforts [31–34], simulations [35–37], and theories [38] have markedly increased our understanding of two-dimensional melting under disorder, but the occurrence of the hexatic phase was never resolved in all of these studies. Therefore, the above-mentioned predictions of Nelson and co-workers [28,29] have never been tested by experiment or simulations.

In this Letter, we propose an experiment on superparamagnetic colloids on a glass substrate on which a small fraction of the particles is pinned, inducing quenched disorder. Clearly, as a reference, the KTHNY scenario occurs for the pure case without any disorder on a pinning-free air-water interface [10,12]. We can now systematically study the melting scenario in detail for different fractions of pinned particles. In our experiments, we confirm the KTHNY scenario and the predictions by Nelson and co-workers [28,29] under disorder. The stability range of the hexatic phase widens upon increasing disorder as opposed to the prediction of Ref. [30]. We also perform two-dimensional computer simulations for parallel dipoles and find good agreement with our experimental data. Extracting an "effective" K_A, we recover the scaling of the elasticity modulus in the presence of disorder. Thereby,

we provide evidence that melting in the presence of disorder is governed by the same defect-mediated process predicted and confirmed for pure systems. Furthermore, we observe heterogeneous orientational order close to the melting temperature but a long-time analysis reveals that such heterogeneities fluctuate strongly on time scales larger than the orientational correlation time indicating critical behavior.

The experimental system consists of superparamagnetic colloidal particles which are confined in two dimensions and subject to quenched disorder embodied by a random distribution of fixed particles. The colloidal suspension is kept at room temperature and an external magnetic field H applied perpendicular to the particle layer induces a repulsive dipole-dipole potential $V(r) = \mu_0(\chi H)^2/r^3$, where χ denotes the magnetic susceptibility [39] and r the particle distance. The phase behavior is studied by tuning the interaction strength via the external magnetic field, quantified by the dimensionless interaction parameter

$$\Gamma = \frac{\mu_0(\pi n)^{3/2}(\chi H)^2}{k_B T}, \tag{1}$$

with the 2D particle density n and the thermal energy $k_B T$. The particles have a diameter $d = 4.5$ μm and the mass density 1.7 kg/dm^3. The suspension is sealed within a cell consisting of two parallel cover slips glued together via a hollow cylindrical glass spacer of 5 mm diameter. By gravity, the particles sediment and form a monolayer on the bottom glass plate, where a short-time lateral diffusion constant of $D = 0.0295$ μm^2/s is observed. Because of van-der-Waals interactions and chemical reactions between colloids and the glass surface, a small amount of particles pin to the substrate. This distribution is slowly altered by thermal tearing or the creation of new pinning connections, but the pinned particles are fixed on the time scale of our measurements. We exemplify three different sample regions with varying pinning strengths ranging from approximately 0.5% to 0.8%. The colloidal ensemble is melted from an equilibrated crystalline state by decreasing H in small steps. After each step, the system is allowed to equilibrate for at least 24 hours before particle trajectories are recorded via video microscopy [40] for 2.7 hours, which equals $\approx 50\tau_B$.

Complementary, computer simulations are carried out in the NAT ensemble, with A denoting the area of the system. The total particle number is fixed to $N = 16000$ and periodic boundary conditions are applied. Each pinning strength is sampled with at least 15 statistically independent configurations of obstacles, which are achieved by pinning randomly selected particles in a fluid configuration of hard disks at a packing fraction of 0.25%. Within statistical precision, this realization of pinning corresponds to the distribution of pinned particles observed in the experiment. Using the standard Metropolis Monte Carlo (MC) algorithm, a full freezing and melting cycle is conducted for each particular setup at which the initially chosen particles remain pinned. After incrementing $\Gamma \propto 1/T$, the system is equilibrated for 5×10^5 MC sweeps before recording data. While Monte Carlo methods are known to converge rapidly towards static equilibrium states, the underlying phase-space sampling provides a suitable means to study dynamic properties, as well [41]. For each parameter set of temperature and pinning strength, the observables obtained by MC simulations are averaged over all sample realizations of disorder.

The KTHNY theory predicts a two-step melting process, in which the isotropic fluid and solid phase are separated by an intermediate hexatic phase. While translational order is only short range in the hexatic phase, orientational order persists. More precisely, it switches from long range in the solid over quasi long range in the hexatic phase to short range in the isotropic fluid. The characteristic range of orientational order in the different phases can be quantified in terms of the correlation $g_6(r, t)$ of the bond order parameter

$$\psi_6 = \frac{1}{n_j}\sum_k e^{i6\theta_{jk}}, \tag{2}$$

where the sum goes over all n_j nearest neighbors of particle j, and θ_{jk} is the angle of the kth bond in respect to a certain reference axis. Mapping the characteristic ranges of the spatial orientational order on the time domain, we can study the dynamical orientational correlation $g_6(t) = \langle \psi_6^*(t)\psi_6(0)\rangle$, which, analogously to the spatial correlation, decays exponentially in the isotropic fluid, and algebraically in the hexatic phase, and approaches a constant value in the solid [42]. This quantity is well suited to characterize the melting process, as discussed in Refs. [8,9] and successfully employed experimentally in Ref. [10].

Figure 1 shows $g_6(t)$ for both, experiment (0.48% pinning) and simulation (0.5%). The time axis is reduced to the Brownian time scale $\tau_B = (d/2)^2/D$. After a short-time decay due to Brownian motion, the characteristic behavior of the solid, the hexatic (linear decay in the log-log plot), and isotropic fluid is clearly distinguishable at long times. To confirm the characteristic decay behavior, $g_6(t)$ is fitted with a second-order polynomial fit on a double-logarithmic scale: $\ln(g_6(t)) = a + b\ln(t/\tau_B) + c\ln^2(t/\tau_B)$, with dimensionless coefficients a, b, and c. Solid, hexatic, and isotropic fluid phases are characterized by the relative contribution of positive or negative curvature, expressed by $c/|b|$. We define an upper and a lower threshold value for $c/|b|$ to distinguish between the negatively curved exponential decay of $g_6(t)$ in the isotropic fluid, positive curvature in the solid, and a linear course in between, reflecting the hexatic phase (for further details and an evaluation of the spatial bond order correlation function see the Supplemental Material [43]).

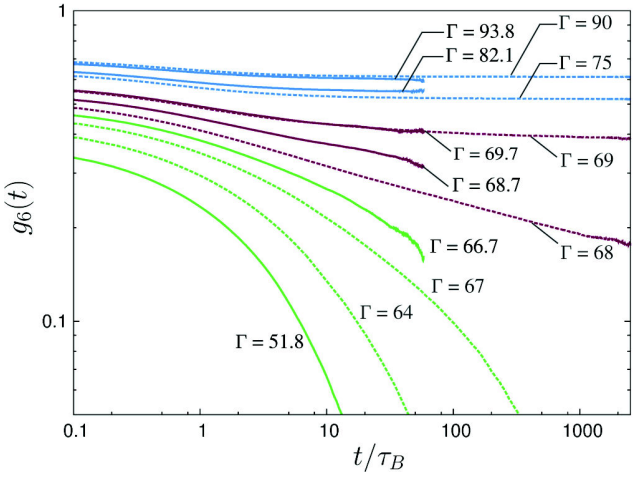

FIG. 1 (color online). Temporal bond orientational correlation function $g_6(t)$ in the presence of quenched disorder plotted versus reduced time t/τ_B on a double-logarithmic scale. The fraction of pinned particles is 0.48% in the experiment and 0.5% in the simulation. Exemplary curves are shown for the isotropic fluid [green (light gray)], hexatic [red (black)], and solid [blue (dark gray)] phase, where experimental data are drawn with solid lines, and computer simulations with dashed lines.

To illustrate the critical behavior at the transition points, we determine the orientational correlation time ξ_t and an "effective" Frank's constant K_A, characterizing the elastic response of topological defects to torsion in the presence of pinned particles (see Fig. 2). The parameters are extracted from exponential fits $\sim e^{-t/\xi_t}$ in the isotropic fluid and algebraic fits $\sim t^{\eta_6/2}$ in the hexatic phase, where the orientational exponent $\eta_6 = 18k_BT/\pi K_A$ is inversely proportional to Frank's constant. In the isotropic fluid, K_A is zero due to the appearance of isolated disclinations. The corresponding stress field "absorbs" external torsion by diffusion and/or rotation. Approaching the hexatic-isotropic fluid transition at the temperature $\Gamma_i^{-1} \approx 0.0148$, ξ_t diverges, and K_A jumps to the finite value $72/\pi$. In the hexatic phase, K_A remains constant due to the presence of quasi–long-range orientational order: a torsion would mediate a separation of dislocations into isolated disclinations, inducing a change in the strain field at a finite stress response. Approaching the solid-hexatic transition, the elastic response to a torsion increases due to the decreasing number of isolated dislocations. Simultaneously, K_A diverges. Our data indicate that, in the presence of disorder, the divergent behavior of Frank's constant spreads. More precisely, K_A increases at lower temperatures for higher pinning strengths, which means that the hexatic-solid transition temperature Γ_m^{-1} strongly depends on disorder, as proposed in Refs. [28,29,35]. Furthermore, this implies the reduction of torsional stiffness at a fixed temperature: in the presence of pinned particles, the response to a torsional stimulus becomes more elastic.

To emphasize the consequences of these distinct characteristics at the transitions on the phase behavior of the system, the two-step melting process is mapped to the parameter plane of temperature and pinning strength. Figure 3 shows the resulting phase diagram. In the cooling and heating cycle of the simulations no hysteresis was found, as is typical for continuous transitions—see the Supplemental Material [43] for details and additional evaluation of our data indicating the continuous nature of the phase transition. The hexatic-isotropic fluid transition is found to remain largely unaffected by pinning; the transition temperature Γ_i^{-1} is barely shifted by disorder. In contrast, the hexatic-solid phase boundary is strongly

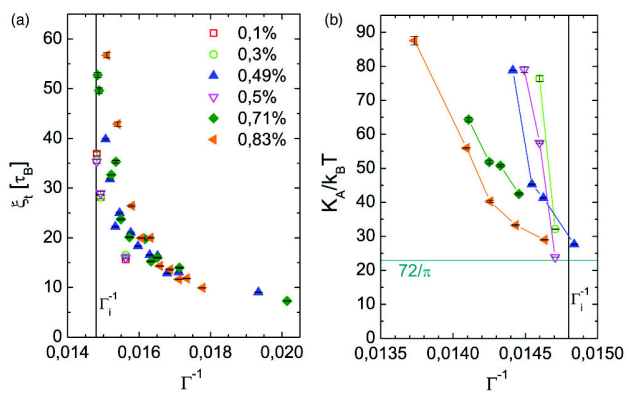

FIG. 2 (color online). (a) Orientational correlation time ξ_t and (b) Frank's constant K_A, for different concentrations of pinned particles. Filled symbols represent experimental data, open symbols simulation. The meaning of the symbols is the same in (a) and (b); lines are guides to the eye. While ξ_t is almost not affected by different pinning strengths, K_A is clearly lowered with increasing pinning.

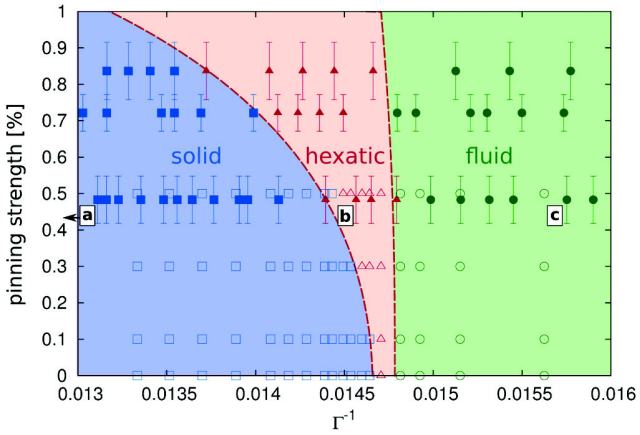

FIG. 3 (color online). Phase diagram indicating the solid [blue (dark gray)], hexatic [red (light gray)] and isotropic fluid [green (medium gray)] phase in the parameter space of temperature $\propto \Gamma^{-1}$ and pinning strength. Full symbols represent experimental data, while open symbols correspond to simulation results. Letters indicate the location of snapshots in Fig. 4.

influenced. The transition temperature is shifted significantly towards lower values for increasing numbers of pinned particles. This can be explained qualitatively considering the influence of pinned sites on the distinct symmetries: a pinned particle causes a strain field in its vicinity and therefore shifts particles to release the created stress. Orientational order can be recovered, since particles are able to adjust the orientational field ψ_6 to their local environment by slight displacements. However, the hexatic-solid transition is governed by a significant change in translational order. If pinned particles are displaced from their ideal lattice position, a positional lack can only be restored by bending lattice lines. Moreover, the shear modulus is zero in the isotropic fluid and hexatic phase, which disburdens the conservation of order by adjusting the strain. As a result, the stability range of the hexatic phase widens with increasing disorder, which is in accordance with theoretical predictions [28,29]. In addition, this effect seems to become more crucial for higher disorder strengths, resulting in a curved behavior of the hexatic-solid phase boundary. This suggests the existence of a critical disorder strength, above which the system is not able to form an ordered state [35], but rather becomes an amorphous solid in the form of a hexatic glass [31,33], depending on the range of quenched disorder [38].

To determine the dynamics of the orientational order in space, we illustrate the magnitude and spatial distribution of the orientational order parameter $\langle|\psi_6|\rangle_t$, averaged over a finite time window of $\approx 50\tau_B$ [see Figs. 4(a)–4(c)]. In the solid phase, orientational order is homogeneous and persistent in time. It is only locally reduced by thermally activated, short living dislocation pairs. In the hexatic and isotropic fluid phase, the magnitudes of $\langle|\psi_6|\rangle_t$ decrease and are subject to a strongly heterogeneous spatial pattern on various length scales. This behavior can equally be observed in computer simulation snapshots (see the Supplemental Material [43]). Similar heterogeneities were reported for an impurity-free two-dimensional Lennard-Jones system [44]. The observed heterogeneities of the orientational order field close to Γ_i are spatiotemporal and reflect criticallike fluctuations at the hexatic-isotropic fluid transition, thus confirming our finding that this transition is continuous [see movie 1 and 2 in the Supplemental Material [43] covering a time window two decades larger (up to $\approx 4000\tau_B$) compared to Figs. 4(a)–4(c)].

To exhibit the proximate effects of the pinned sites, we compare the spatial dynamics of particles in the vicinity of and far away from pinning centers for an intermediate pinning strength [see Fig. 4(d)]. While in the isotropic fluid the mean square displacement is decreased near pinning, it is increased in the solid. The inhibited dynamics in the disordered phase can be explained by the confining character of the pinned sites. Conversely, the local dynamics in the solid seems to be increased near pinning. This might be

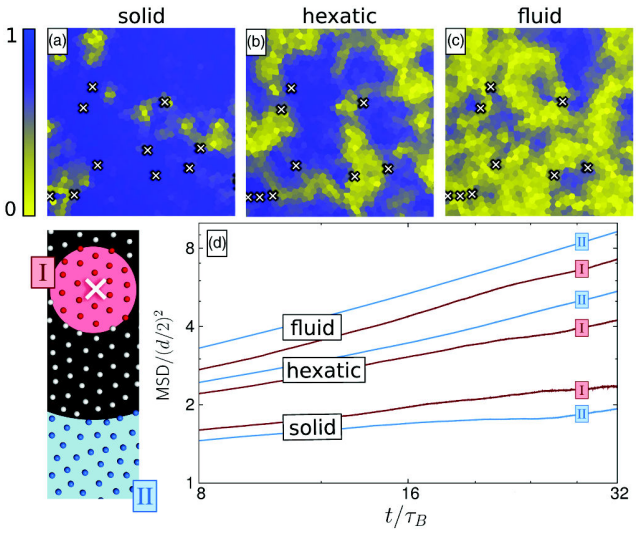

FIG. 4 (color online). (a)–(c) Snapshots of the experimental system at 0.48% pinning, showing the local orientational order parameter $\langle|\psi_6|\rangle_t$ averaged over $\approx 50\tau_B$ in the different phases [(a) $\Gamma^{-1} = 0.0117$, (b) $\Gamma^{-1} = 0.0143$, (c) $\Gamma^{-1} = 0.0154$]. The field of view is 450×450 μm. Voronoi cells are color coded according to the bar on the left. (d) Mean square displacement (MSD) calculated for particles within a distance of $8d$ around pinning sites (region I in the inset) and more than $24d$ away from them (region II). Temperatures correspond to (a)–(c).

related to an increased probability of dislocation pair unbinding induced by quenched disorder [28,35]. The crossover lies in the hexatic phase at $\Gamma^{-1} \approx 0.0144$, close to the solid-hexatic phase transition, which supports our finding that this transition is more affected by quenched disorder than the hexatic-isotropic liquid one.

In conclusion, we investigated the melting transition of 2D crystals under quenched disorder in the form of pinning sites. Analyzing the dynamics of the orientational correlation, we probed the disorder vs temperature phase diagram and determined the orientational correlation time and Frank's constant. Both show divergent behavior at the corresponding phase transition, confirming the continuous melting character of the KTHNY scenario. While the hexatic-isotropic fluid transition is rather unaffected by pinning, the transition from the solid to the hexatic phase is strongly influenced, resulting in a significant broadening of the hexatic phase. In addition, we observed spatiotemporal dynamical heterogeneities of the orientational order parameter (see the movies in the Supplemental Material [43]), marking critical(like) fluctuations, whereas first-order characteristics are not observed. In comparison to the bulk, the local dynamics of particles in the vicinity of pinned sites is decreased in the isotropic liquid, which is not directly reflected by a localization of the fluctuations of the order parameter (see the movies in the Supplemental Material [43]). The further investigation of 2D systems with this kind of weak quenched disorder might reveal

the role of critical fluctuations in the disorder-mediated melting process and also opens the field of hexatic membranes with adatoms or molecules. Using weak random potentials or (quasi)crystalline structures, commensurable and incommensurable crystal transitions come into focus, and for strong disorder, crystal to amorphous solid transitions can be investigated.

We thank A. Arnold, M. Schmiedeberg, and D. Hajnal for helpful discussions, as well as R. Messina and L. Assoud for providing a computer code. We thank the DFG for financial support within SFB TR6 (Projects C2 and C3).

[1] J. M. Kosterlitz and D. J. Thouless, J. Phys. C **5**, L124 (1972).
[2] J. M. Kosterlitz and D. J. Thouless, J. Phys. C **6**, 1181 (1973).
[3] B. I. Halperin and D. R. Nelson, Phys. Rev. Lett. **41**, 121 (1978).
[4] D. R. Nelson and B. I. Halperin, Phys. Rev. B **19**, 2457 (1979).
[5] A. P. Young, Phys. Rev. B **19**, 1855 (1979).
[6] K. J. Strandburg, Rev. Mod. Phys. **60**, 161 (1988).
[7] For a review, see P. M. Chaikin and T. C. Lubensky, *Principles of Condensed Matter Physics* (Cambridge University Press, Cambridge, England, 1995).
[8] S. Z. Lin, B. Zheng, and S. Trimper, Phys. Rev. E **73**, 066106 (2006).
[9] N. Gribova, A. Arnold, T. Schilling, and C. Holm, J. Chem. Phys. **135**, 054514 (2011).
[10] K. Zahn and G. Maret, Phys. Rev. Lett. **85**, 3656 (2000).
[11] H. H. von Grünberg, P. Keim, K. Zahn, and G. Maret, Phys. Rev. Lett. **93**, 255703 (2004).
[12] P. Keim, G. Maret, and H. H. von Grünberg, Phys. Rev. E **75**, 031402 (2007).
[13] Y. Han, N. Y. Ha, A. M. Alsayed, and A. G. Yodh, Phys. Rev. E **77**, 041406 (2008).
[14] S. Prestipino, F. Saija, and P. V. Giaquinta, Phys. Rev. Lett. **106**, 235701 (2011).
[15] Y. Peng, Z. Wang, A. M. Alsayed, A. G. Yodh, and Y. Han, Phys. Rev. Lett. **104**, 205703 (2010).
[16] A. H. Marcus and S. A. Rice, Phys. Rev. Lett. **77**, 2577 (1996).
[17] E. P. Bernard and W. Krauth, Phys. Rev. Lett. **107**, 155704 (2011).
[18] Since correlation lengths diverge exponentially in the KTHNY theory such that one can take derivatives arbitrarily often, those transitions are called continuous.
[19] J. C. Meyer, A. K. Geim, M. I. Katsnelson, K. S. Novoselov, T. J. Booth, and S. Roth, Nature (London) **446**, 60 (2007).
[20] A. I. Larkin, Sov. Phys. JETP **31**, 784 (1970).
[21] Y. Imry and S.-K. Ma, Phys. Rev. Lett. **35**, 1399 (1975).
[22] A. I. Larkin and Y. N. Ovchinnikov, J. Low Temp. Phys. **34**, 409 (1979).
[23] D. S. Fisher, M. P. A. Fisher, and D. A. Huse, Phys. Rev. B **43**, 130 (1991).
[24] R. Geer, T. Stoebe, C. C. Huang, R. Pindak, J. W. Goodby, M. Cheng, J. T. Ho, and S. W. Hui, Nature (London) **355**, 152 (1992).
[25] R. Viswanathan, L. L. Madsen, J. A. Zasadzinski, and D. K. Schwartz, Science **269**, 51 (1995).
[26] I. R. Peterson, R. Steitz, H. Krug, and I. Voigt-Martin, J. Phys. (France) **51**, 1003 (1990).
[27] B. Berge, L. Faucheux, K. Schwab, and A. Libchaber, Nature (London) **350**, 322 (1991).
[28] D. R. Nelson, Phys. Rev. B **27**, 2902 (1983).
[29] S. Sachdev and D. R. Nelson, J. Phys. C **17**, 5473 (1984).
[30] R. A. Serota, Phys. Rev. B **33**, 3403 (1986).
[31] R. E. Kusner, J. A. Mann, and A. J. Dahm, Phys. Rev. B **49**, 9190 (1994).
[32] A. Pertsinidis and X. S. Ling, Phys. Rev. Lett. **100**, 028303 (2008).
[33] P. Yunker, Z. Zhang, and A. G. Yodh, Phys. Rev. Lett. **104**, 015701 (2010).
[34] P. Hartmann, A. Douglass, J. C. Reyes, L. S. Matthews, T. W. Hyde, A. Kovacs, and Z. Donko, Phys. Rev. Lett. **105**, 115004 (2010).
[35] M.-C. Cha and H. A. Fertig, Phys. Rev. Lett. **74**, 4867 (1995).
[36] S. Herrera-Velarde and H. H. von Grünberg, Soft Matter **5**, 391 (2009).
[37] T. Kawasaki and H. Tanaka, J. Phys. Condens. Matter **23**, 194121 (2011).
[38] D. Carpentier and P. Le Doussal, Phys. Rev. Lett. **81**, 1881 (1998).
[39] The magnetic susceptibility is determined via the comparison of the pair correlation function with simulations as $\chi = (5.75 \pm 0.05) \times 10^{-11}$ Am^2/T.
[40] F. Ebert, P. Dillmann, G. Maret, and P. Keim, Rev. Sci. Instrum. **80**, 083902 (2009).
[41] K. Binder, Rep. Prog. Phys. **60**, 487 (1997).
[42] D. R. Nelson, in *Phase Transition and Critical Phenomena*, edited by C. Domb and J. L. Lebowitz (Academic, New York, 1983).
[43] See Supplemental Material at http://link.aps.org/supplemental/10.1103/PhysRevLett.111.098301 for an evaluation of simulation data equivalent to Fig. 4, movies illustrating criticallike fluctuations in simulations and experiment, details on the polynomial fit criterion, further evidence for the continuous nature of the phase transition, and an evaluation of spatial correlation functions.
[44] H. Shiba, A. Onuki, and T. Araki, Europhys. Lett. **86**, 66 004 (2009).

Erratum: Two-Dimensional Melting under Quenched Disorder [Phys. Rev. Lett. 111, 098301 (2013)]

Sven Deutschländer, Tobias Horn, Hartmut Löwen, Georg Maret, and Peter Keim

(Received 27 November 2013; published 18 December 2013)

DOI: 10.1103/PhysRevLett.111.259901 PACS numbers: 82.70.Dd, 61.20.Ja, 64.70.D-, 64.70.pv, 99.10.Cd

We have detected a typing error in Eq. (1) of our Letter. A prefactor of $1/4\pi$ was missing in the definition of the interaction strength Γ.

Equation (1) should correctly read

$$\Gamma = \frac{\mu_0(\chi H)^2(\pi n)^{3/2}}{4\pi k_B T}. \tag{1}$$

The same prefactor has to be included in the preceding definition of the repulsive dipole-dipole potential, which correctly reads $V(r) = \mu_0(\chi H)^2/4\pi r^3$.

Supplemental material for: Two-dimensional melting under quenched disorder

July 30, 2013

1 Time-averaged orientational order

Fig. 4 of the main article shows the analysis for the experimental data. Figure 1 shows the same analysis performed for simulations. There is very good agreement between experiment and simulations.

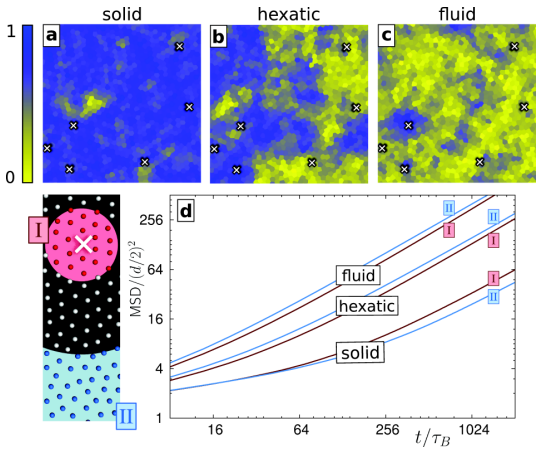

Figure 1: (a-c): Same as Figure 4 in the main paper but now for the simulations. Snapshots of the simulation system at 0.5% pinning, showing the local orientational order parameter $\langle|\psi_6|\rangle_t$ averaged over $\approx 70\ \tau_B$ in the different phases (a: $\Gamma^{-1} = 0.01429$, b: $\Gamma^{-1} = 0.01471$, c: $\Gamma^{-1} = 0.01563$,). The field of view corresponds to $450\mu\text{m} \times 450\mu\text{m}$. Voronoi cells are color-coded according to the bar on the left. (d): Mean square displacement (MSD) calculated for particles within a distance of $8d$ around pinning sites (region I in inset) and more than $24d$ away from them (region II). The temperatures for solid, hexatic and fluid phase correspond to (a-c).

2 Description of the movies

To illustrate the fluctuations of the order parameter near the hexatic-isotropic liquid and hexatic-solid phase transition, we calculate the time evolution of the magnitude of the local bond order parameter $|\psi_6| = \left|\frac{1}{n_j}\sum_k e^{i6\theta_{jk}}\right|$ for both, experiment and simulation for long time runs. Like in Fig. 4, a-c in the main text and Fig. 1 of the supp. mat. particles are represented by their Voronoi cells and pinned sites are marked with crosses. The Voronoi cells are color-coded with the magnitude of the local bond-order paramater $\langle|\psi_6|\rangle_t$ averaged for a finite time window. This time window was chosen to be shorter than the orientational correlation time at the hexatic-isotropic liquid transition to analyze the present local order. This was repeated for a duration much longer than the orientational correlation time at the given temperature. A movie (with linear time scale) was constructed from the images. As can be seen in the movies for both, experiment and simulation, the local bond order field shows heterogeneities in space and time. This can be interpreted as critical(-like) fluctuations of the orientational order field. Patterns of similar magnitude do not persist in time as expected for systems with phase equilibria, nor do they move due to possible grain boundary dynamics. The patterns clearly emerge and disappear on various time and length scales, marking a continuous (or second order) phase transition. In addition, the fluctuations seem to be slightly enhanced in regions with increased pinning which might point to a dependency of critical fluctuations on quenched disorder.

- Movie 1: Experimental data recorded at $\Gamma^{-1} = 0.01447$ and 0.48% pinning, covering a time frame of $\approx 4080\tau_B \approx 8$ days. $\langle|\psi_6|\rangle_t$ was averaged over $\approx 42\,\tau_B$.

- Movie 2: Simulation data recorded at $\Gamma^{-1} = 0.0146$ and 0.5% pinning, covering a time frame of $\approx 2700\tau_B$. $\langle|\psi_6|\rangle_t$ was averaged over $\approx 70\,\tau_B$.

3 Polynomial fit criterion

In order to quantify the characteristic decay properties of $g_6(t)$ in the solid, hexatic and fluid phase, the linearly equidistant $g_6(t)$ data points are fitted with a second order polynomial fit on a double-logarithmic scale. This is achieved by calculating the least square parabola

$$\ln(g_6(t)) = a + b\,\ln(t/\tau_B) + c\,\ln^2(t/\tau_B) \tag{1}$$

with dimensionless coefficients a, b and c for the set of values $(\ln(t/\tau_B), \ln(g_6(t)))$. To characterize solid, hexatic and fluid phase, the relative contribution of curvature is considered, expressed by the ratio $c/|b|$. In the fluid phase, $g_6(t)$ decays exponentially, and the polynomial fit (1) exhibits negative curvature, $c/|b| < 0$. In the solid phase, $g_6(t)$ approaches a constant value such that the data is best approximated by a positively curved polynomial, $c/|b| > 0$. Since the algebraic decay of $g_6(t)$ corresponds to a linear decay in the log-log plot, the relative contribution of curvature vanishes, $c/|b| \approx 0$. We

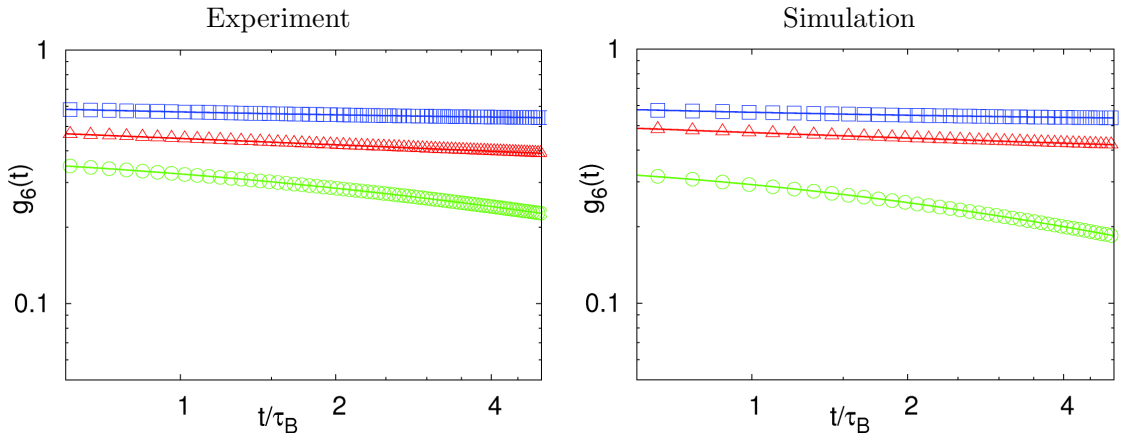

solid, $\Gamma^{-1} = 0.0117$, $c/|b| = 0.1305$
hexatic, $\Gamma^{-1} = 0.0143$, $c/|b| = -0.0056$
fluid, $\Gamma^{-1} = 0.0154$, $c/|b| = -0.3107$

solid, $\Gamma^{-1} = 0.0133$, $c/|b| = 0.1413$
hexatic, $\Gamma^{-1} = 0.0146$, $c/|b| = 0.0444$
fluid, $\Gamma^{-1} = 0.0156$, $c/|b| = -0.4131$

Figure 2: Exemplary $g_6(t)$ curves recorded in experiment & simulation (symbols) for the solid (blue squares), hexatic (red triangles) and isotropic fluid phase (green circles) fitted with the second order polynomial fit (1) (solid lines). The effective temperature Γ^{-1} and relative contribution of curvature $c/|b|$ are stated below the plot. The fraction of pinned particles is 0.48% in the experiment and 0.5% in the simulation.

define a lower and an upper threshold, $c/|b| = \pm 0.07$ to map all $g_6(t)$ curves recorded to the three phases (see Table 1).

phase	$g_6(t)$	$c/\|b\|$
solid	constant	> 0.07
hexatic	algebraic decay	$-0.07 \leq c/\|b\| \leq 0.07$
fluid	exponential decay	< -0.07

Table 1: Characterization of solid, hexatic and fluid phase via the relative curvature contribution in Eq. (1).

For an equivalent treatment of experimental and simulation data, we consider the time-window $0.6 \leq t/\tau_B \leq 5$ and shift the origin to $t_0/\tau_B = 0.6$ to ensure $b < 0$, see Fig. 2. The phase diagram depicted in Fig. 3 of the main article is obtained with these settings. To test our approach for longer times, the polynomial fit is extended to $t/\tau_B = 400$ for the simulation data (Fig. 3), at which all properties of the phase diagram are recovered (see Fig. 4).
As a further consistency check, we applied the polynomial fit criterion to correlation

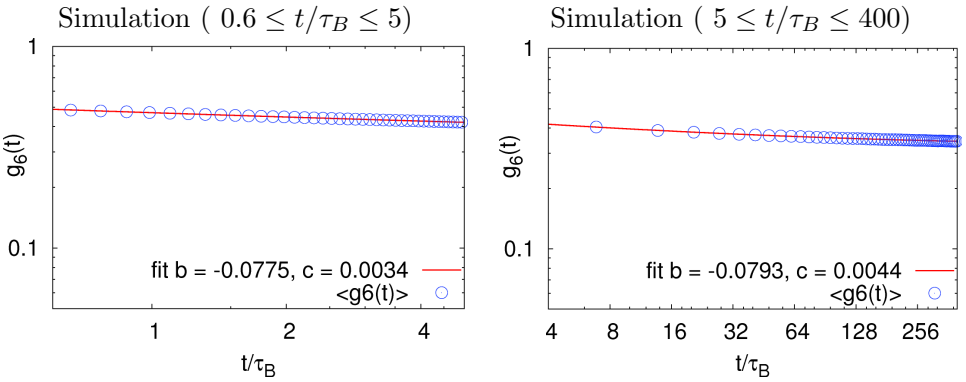

Figure 3: Second order polynomial fit applied to exemplary simulation data for times $0.6 \leq t/\tau_B \leq 5$ (left) and $5 \leq t/\tau_B \leq 400$ (right).

function data recorded in Ref. [1] .The envelope of the local maxima of $g_6(r)$ was fitted in the range $0.5 \leq r/\sigma \leq 64$. In doing so, our approach was found to recover the distinction drawn in [1] between curves corresponding to the fluid, hexatic and solid phase (see Fig. 1 therein).

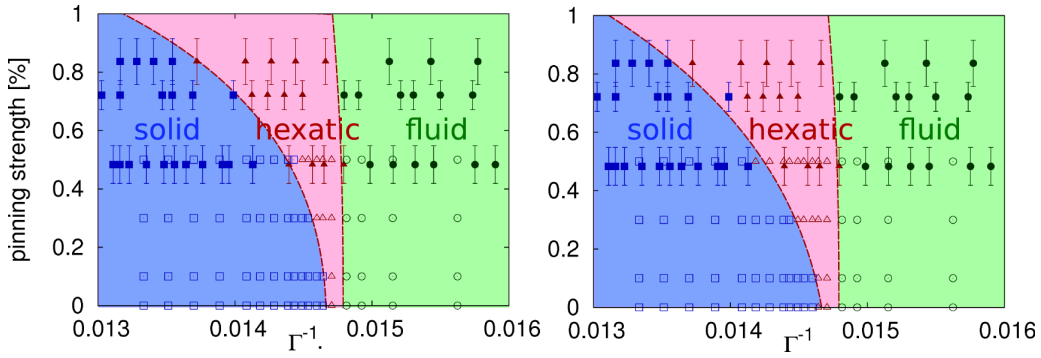

Figure 4: Phase diagram with simulation data fitted in the time-range $0.6 \leq t/\tau_B \leq 5$ (left) or $5 \leq t/\tau_B \leq 400$ (right). Open symbols represent simulation data, while full symbols correspond to experimental results. The latter are not altered and are shown for comparison only. The phase diagram does not change significantly if the parameters are varied, covering a large range of values.

[1] N. Gribova, A. Arnold, T. Schilling, and C. Holm, J. Chem. Phys. **135**, 054514 (2011).

4 Further evidence of the continuous nature of the melting process

A full cooling and heating cycle was conducted in the computer simulations. At each temperature step, the mean specific energy $\langle U \rangle$ was calculated. The results are depicted in Fig. 5. The cooling and heating branches collapse, which indicates a continuous phase transition. In order to distinguish between the observed widening of the hex-

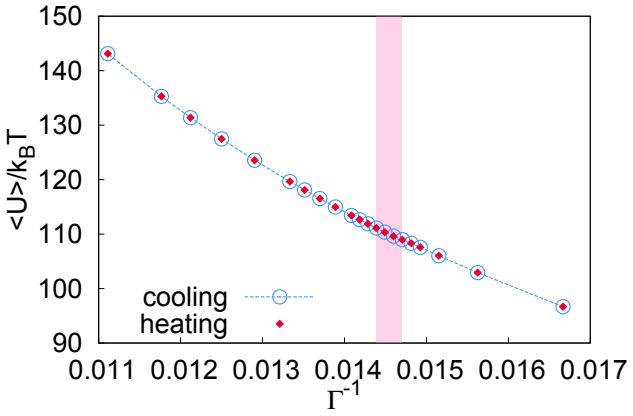

Figure 5: Mean specific energy $\langle U \rangle$ for cooling (open circles) and heating (full diamonds). The pinning fraction is 0.5%. The temperature range corresponding to the intermediate hexatic phase is indicated in red.

atic phase with increasing disorder and the signature of a polycrystalline structure, we examine a polycrystalline reference system by quenching an isotropic bulk fluid to the deep solid phase in the computer simulation. The resulting configuration consists of several crystalline regions with different orientations, which are sharply separated by grain boundaries, see Fig. 6. In comparison, a snapshot of the system with pinning in the hexatic phase exhibits no grain boundaries and apart from the spatio-temporal fluctuations discussed in the main article, there is globally homogeneous orientational order (Fig. 6). Furthermore, we monitor the probability distribution of the squared value of the orientational order parameter ψ_{6L} on various length scales. As discussed in [1], a monomodal distribution is expected in the absence of polycrystallinity. Our results are shown in Fig. 7 and clearly indicate a single peak in the distribution. While in the isotropic fluid phase, the distribution diverges at $\psi_{6L}^2 = 0$ (Fig. 7 (a)), the location of the peak shifts to intermediate values at the isotropic $\rightarrow$ hexatic transition (b) and approaches higher values as the system is cooled further (c). For the pinning system, the distribution is clearly monomodal, while the distribution is bimodal for the polycrystalline reference system, see Fig. 7 (d).

To provide further evidence for the continuous nature of the phase transition, we conduct a finite-size scaling analysis of the fluctuation of the translational and orientational

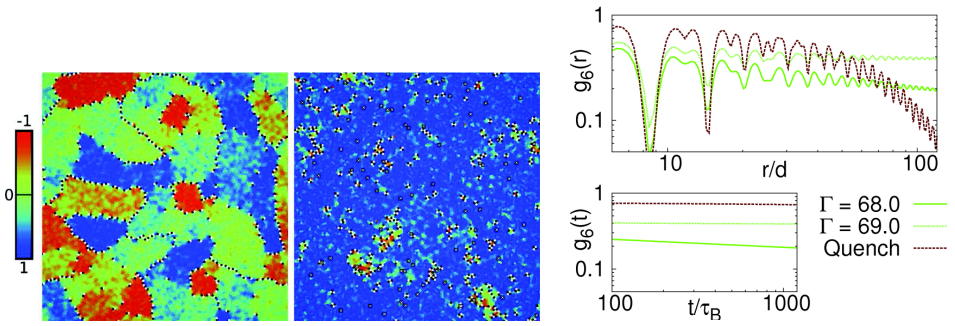

Figure 6: Left, Middle: Computer simulation snapshots showing the orientation of the local director $\boldsymbol{\psi}_{6,i}$ relative to the global director $\boldsymbol{\psi}_6$. The colorcode corresponds to the bar on the left and is based on the normalized scalar product $\boldsymbol{\psi}_{6,i} \cdot \boldsymbol{\psi}_6/(|\boldsymbol{\psi}_{6,i}||\boldsymbol{\psi}_6|)$. Five- and sevenfolded defects are shown in black or white, respectively. Left: Pure bulk system after a quench from $\Gamma = 60$ to $\Gamma = 200$. Middle: System with 0.5% pinning in the hexatic phase ($\Gamma = 69.5$) Crosses indicate the positions of pinned particles. Right: Spatial and temporal correlation functions $g_6(r)$ (top) and $g_6(t)$ (bottom) calculated for the quenched polycrystalline system (red dashed curve). As a reference, typical computer simulation curves from the hexatic phase are shown for the system with 0.5% pinning (green solid / dotted curve).

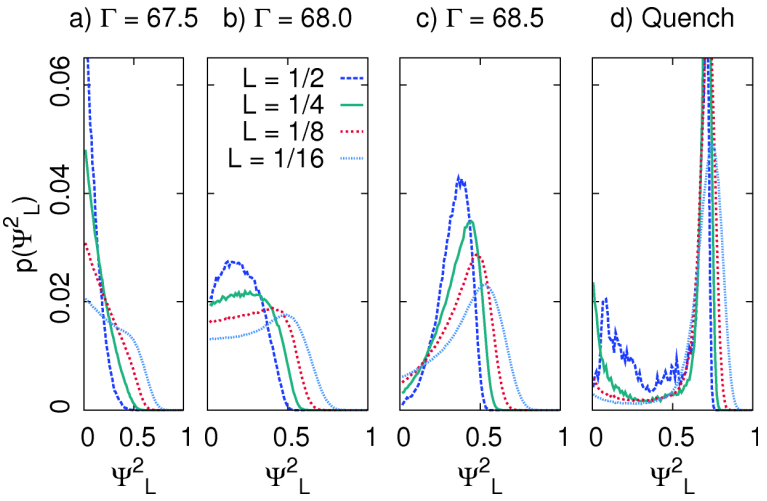

Figure 7: Probability distribution of ψ_{6L}^2 calculated for subcells of sidelength L (stated as a fraction of the total box length). (a-c) System with pinning, (d) Quenched polycrystalline configuration (shown in Fig. 6).

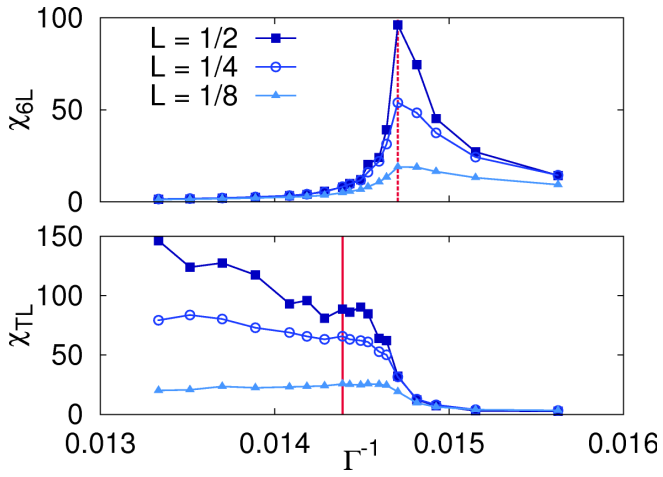

Figure 8: Top: Susceptibility χ_{6L} of the orientational order parameter as defined in [2] versus effective temperature calculated for subcells of sidelength L (stated as a fraction of the total box length). The dashed line corresponds to T_i derived from the analysis of $g_6(t)$. Bottom: Susceptibility χ_{TL} of the translational order parameter. The solid line corresponds to T_m derived from the analysis of $g_6(t)$. Data is shown for computer simulations, the pinning fraction is 0.5%.

order parameters ψ_T and ψ_6, respectively. Therefore, we consider the translational and orientational susceptibilities χ_{TL} and χ_{6L} as defined in Ref. [2], Our results are shown in Fig. 8. The susceptibility χ_{6L} diverges at the value of T_i estimated by the analysis of $g_6(t)$. At a lower temperature close to the estimated value of T_m, χ_{TL} undergoes a reasonable increase, then decreases for large systems once again pointing to a possible divergence for $L \to \infty$. The maximum in the susceptibility χ_{TL} occurs at higher coupling than that of χ_{6L} (for $L = 1/2$). The existence of two distinct temperatures for the divergent behavior of χ_{6L} and χ_{TL} indicates the two-step melting process. Further, it has to be pointed out that finding a proper reciprocal lattice vector $\vec{G}$ is essential for a reliable analysis of the translational order parameter ψ_T, its correlation, and susceptibility. For statistically independent ensembles, $\vec{G}$ will change and should be calculated separately for every ensemble. This has been done in our analysis, we determined the lattice vector that maximizes ψ_T for every ensemble. However, this becomes increasingly difficult approaching the hexatic phase due to the increasing dislocation densities. Furthermore, in the hexatic phase the reciprocal lattice vector is no longer defined since the translational order is short range and no lattice exists.

[2] Y. Han, N. Y. Ha, A. M. Alsayed, A. G. Yodh, Phys. Rev. E **77**, 041406 (2008).

5 Spatial correlation functions

In addition to the analysis of the temporal correlation function $g_6(t)$ stated in the main article, the spatial correlation function $g_6(r) = \langle \psi_6^*(r)\psi_6(0)\rangle$ is discussed here. Figure 5 shows exemplary curves for $g_6(r)$ in the isotropic fluid, hexatic and solid phase for experimental and simulation data. The decay behavior in the different phases is clearly distinguishable. While in the isotropic fluid $g_6(r)$ decays exponentially, it has an algebraic signature in the hexatic phase, and approaches a constant value in the solid, excluding the possibility of polycrystallinity. Consistent with Poisson statistics, there is an accumulation of pinned particles in the lower left corner of the experimental sample, see Fig. 10. This induces a small distortion of the lattice in the lower left corner leading to the weak decay of the experimental curve in the solid phase at $\Gamma = 119.5$. Since the orientational correlation in the time domain is robust to such distortions it is better suited to identify the transition temperature.

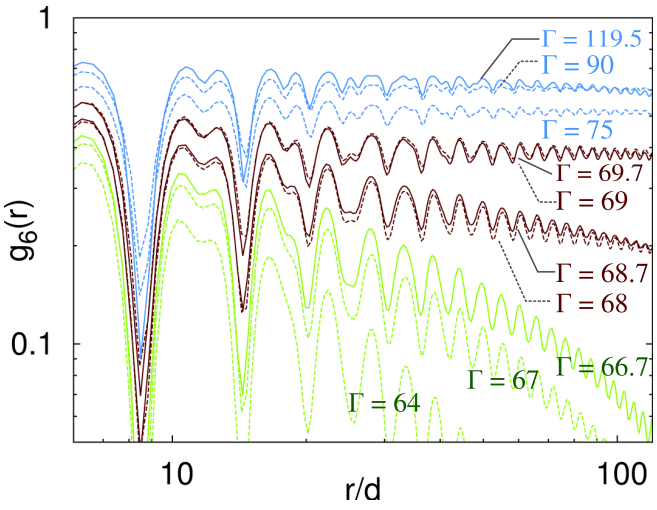

Figure 9: Spatial correlation function $g_6(r)$ of the bond order parameter in the presence of quenched disorder plotted versus reduced distance r/d on a double-logarithmic scale. The fraction of pinned particles is 0.48% in the experiment and 0.5% in the simulation. Exemplary curves are shown for the isotropic fluid (green), hexatic (red), and solid (blue) phase, where experimental data is drawn with solid, computer simulations with dashed lines.

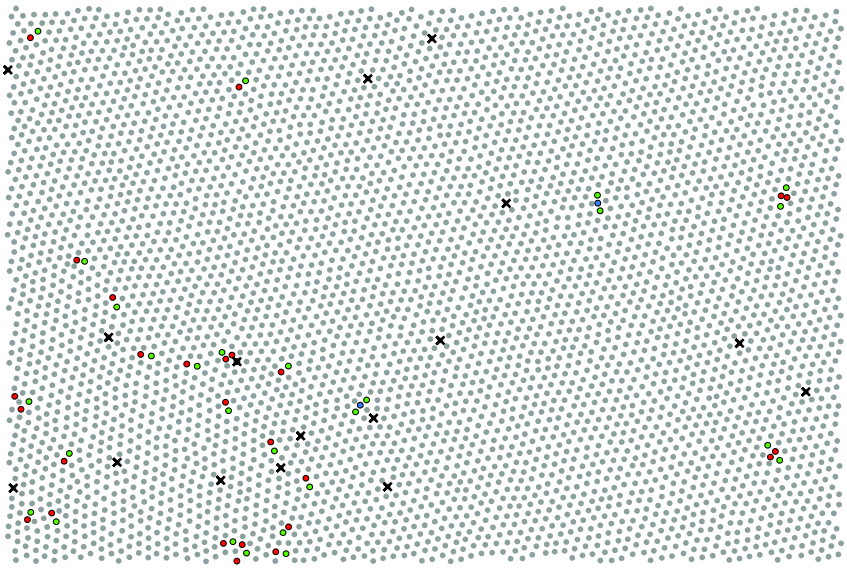

Figure 10: Snapshot of the system at $\Gamma = 119.5$ illustrating the defect distribution. Particles with six nearest neighbors are colored gray, fivefold coordinated sites red, sevenfold green, and particles with more than seven or less than 5 nearest neighbors are colored blue. Pinned particles are marked with crosses. The lower left of the field of view shows a small distortion due to an accumulation of pinned particles in the experiment.

1) Two-dimensional melting under quenched disorder	
Journal	Physical Review Letters
Impact Factor	7.728
Authorship	2nd author
Contribution	33%
	Computer simulations and data analysis

Fluctuations of orientational order and clustering in a two-dimensional colloidal system under quenched disorder

Tobias Horn,[1,*] Sven Deutschländer,[2] Hartmut Löwen,[1] Georg Maret,[2] and Peter Keim[2]
[1]*Institut für Theoretische Physik II, Heinrich-Heine-Universität Düsseldorf, D-40225 Düsseldorf, Germany*
[2]*Fachbereich für Physik, Universität Konstanz, D-78464 Konstanz, Germany*
(Received 10 September 2013; published 11 December 2013)

Using both video microscopy of superparamagnetic colloidal particles confined in two dimensions and corresponding computer simulations of repulsive parallel dipoles, we study the formation of fluctuating orientational clusters and topological defects in the context of the KTHNY-like melting scenario under quenched disorder. We analyze cluster densities, average cluster sizes, and the population of noncluster particles, as well as the development of defects, as a function of the system temperature and disorder strength. In addition, the probability distribution of clustering and orientational order is presented. We find that the well-known disorder-induced widening of the hexatic phase can be traced back to the distinct development characteristics of clusters and defects along the melting transitions from the solid phase to the hexatic phase to the isotropic fluid.

DOI: 10.1103/PhysRevE.88.062305 PACS number(s): 82.70.Dd, 64.70.D−, 61.20.Ja, 64.70.pv

I. INTRODUCTION

The controversy about the microscopic process controlling melting in two dimensions has lasted for several decades. According to the widely accepted theory by Kosterlitz, Thouless, Halperin, Nelson, and Young (KTHNY) [1–5], two-dimensional (2D) melting is a sequence of two continuous phase transitions. The solid and isotropic fluid phases are separated by an intermediate anisotropic fluid phase with quasi-long-range sixfold orientational order, called the *hexatic* phase. The KTHNY scenario further suggests that the two continuous transitions are driven by the dissociation of thermally activated topological defects [2,5]. Given the sixfold symmetry of a triangular lattice, a dislocation constitutes a topological defect which consists of a pair of particles with five and seven nearest neighbors, respectively. Following the predictions of the KTHNY theory, dislocations are bound into neutral pairs in the solid phase, and orientational order is long-range; i.e., the orientational correlation function attains a finite value. As pointed out by Mermin [6], the translational order of the crystalline state is only quasi-long-range due to long-wavelength fluctuations. Mediated by the unbinding of dislocation pairs into isolated dislocations, the transition to the hexatic phase takes place at a temperature T_m [4]. Although translational order is destroyed by the presence of isolated dislocations, orientational order persists in the hexatic phase on a quasi-long-range scale [3,4]. Thus, in the hexatic phase, the orientational correlation function decays algebraically as a function of the separation distance. The transition from the hexatic to the isotropic fluid phase at the temperature $T_i > T_m$ is marked by the unbinding of dislocations into single five- and sevenfold point defects, which are referred to as disclinations. In the isotropic fluid, orientational order vanishes and the orientational correlation function decays exponentially.

Alternative approaches to melting in two dimensions have been conceived where the melting process is modeled as a single first-order transition [7,8]. However, throughout numerous experimental and simulation studies, the KTHNY theory could not be consistently verified or refuted [9]. Instead, evidence was found that the melting process strongly depends on the pair interaction of the system at hand [10]. While systems governed by very short-range or hard-core interactions are reported to exhibit coexisting phases [11–13], thus contradicting the notion of a continuous transition, reports on soft repulsive particles in two dimensions favor the KTHNY scenario [14–16]. For particles interacting via long-range dipolar interactions scaling with the inverse cube of the particle separation, the KTHNY scenario has been unambiguously confirmed [17–19]. Video-microscopy experiments on superparamagnetic colloidal particles pending at an air-water interface, where an external magnetic field induces dipolar moments perpendicular to the surface, have verified the predictions of the KTHNY scenario in detail [20,21], including the elastic properties related to the mechanism of defect unbinding [22]. Furthermore, this setup was studied after a quench by instantaneously increasing the external magnetic field [23–25]. Thereby, crystallization occurred without any evidence of the hexatic phase. Instead, the local formation of crystallites, which gradually merged into larger crystalline patches, leads to a polycrystalline state [23].

According to theoretical predictions by Nelson and coworkers, the two-stage melting scenario persists in the presence of weak disorder [26,27], and the stability range of the hexatic phase widens with increasing disorder. While T_i is predicted to be largely unaffected by disorder, T_m decreases with increasing disorder until, eventually, no crystalline state can be established [26]. While the original work suggested a reentrant melting at low temperatures in the presence of disorder [26], later works revised this idea and a final prediction of the stability range of the ordered (i.e., solid) phase in the temperature-disorder plane was stated in [28]. Further numerical studies confirmed the topography of the ordered-disordered phase diagram [29], albeit the hexatic phase was not resolved. Experimental realizations of colloidal systems under quenched disorder were explored, where quenched disorder was embodied by larger particles dispersed in an array of smaller particles. Thereby, the solid phase exhibited the properties of an hexatic glass [30]. Static and dynamic properties of the crystalline state in the presence of a random pinning

*thorn@thphy.uni-duesseldorf.de

potential were studied in [31]. Additionally, the properties of a disorder-induced glass transition have been thoroughly accounted for [32–34]. Recent studies on experimental model systems like magnetized monolayers [35] or single-layer complex plasmas [36] have increased our understanding of the 2D crystallization process.

In a previous work [37], we proposed an experiment on superparamagnetic colloidal particles on a substrate, where quenched disorder is realized by randomly pinning particles to the substrate. Probing different regions of the sample with varying fractions of pinned particles, the melting process was analyzed for various degrees of disorder. Thus, the specific dependency of the transition temperatures T_i and T_m on disorder predicted in [26] and [27] was verified and a broadening of the hexatic phase could be observed. Furthermore, computer simulations on parallel dipoles in two dimensions were conducted, which exhibited very good agreement with the experimental data.

In this paper, we extend our previous findings on the disorder-induced melting process [37] with a detailed analysis of orientational clusters which show strong fluctuations in time. The development of these clusters is discussed globally and locally as a function of the induced disorder in the form of particle pinning. Dealing with fluctuations on various length scales in continuous 2D melting, this is an essential part of understanding the conservation of the continuous nature of the transitions in the presence of weak induced disorder. In the isotropic liquid phase, the emergence of small clusters corresponds to strongly fluctuating patches of high orientational order, which gradually merge into bigger clusters at lower temperatures. The emergence of a single cluster spanning the entire system occurs close to the isotropic $\rightarrow$ hexatic transition. As discussed in [37], the orientational order parameter exhibits spatiotemporal critical(-like) fluctuations close to the isotropic-hexatic transition and throughout the hexatic phase. In the coarsened picture of orientational clusters, these fluctuations correspond to regions excluded from clusters. Albeit the description of orientational clusters is formally similar to the analysis of heterogeneous crystallites in a quenched colloidal system as explored in [23], orientational clusters are not invoked by a quench of the system but rather exhibit the nature of the continuous transition. As we observe in computer simulations and experiment, the number and size of these clusters display characteristic properties in the isotropic fluid, hexatic fluid, and solid phase. Analyzing setups with varying degrees of quenched disorder, the broadening of the hexatic phase can be traced back to inhibited cluster formation. As indicated by a comparison of our results to bulk reference simulations, the formation of orientational clusters is not induced by the presence of pinned particles but can be observed in a pure system as well. The analysis of the density of topological defects indicates that the widened stability range of the hexatic phase reported in [37] is in fact associated with an increased abundance of isolated dislocations. This is consistent with the KTHNY scenario, which predicts that isolated dislocations emerge in the hexatic phase and that quenched disorder triggers the unbinding of dislocation pairs. Additionally, we present further analysis of our experimental and numerical data supporting the continuous nature of the isotropic-hexatic phase transition.

The paper is organized as follows: In Sec. II, we describe the experiment. The simulation technique is reported in Sec. III. Section IV contains a description of our methods and introduces the definition of clusters. Our analysis of cluster formation and the finite-size behavior of global orientational order is given in Sec. V. Topological defects are analyzed in Sec. VI. Finally, Sec. VII provides the conclusion.

II. EXPERIMENTAL SETUP

We study a suspension of superparamagnetic colloidal particles in two dimensions. Confined within a cylindrical glass cell of 5-mm diameter, the particles sediment due to gravity and form a monolayer on the bottom glass plate. Quenched disorder is imposed by the pinning of a small amount of particles which are attached to the glass substrate due to van der Waals interactions and chemical reactions. The particles have a diameter of $d = 4.5\ \mu$m and a mass density of $1.7\ \mathrm{kg/dm^3}$. The short-time lateral diffusion constant on the glass substrate is $D = 0.0295\ \mu\mathrm{m}^2/\mathrm{s}$ and the Brownian time scale corresponds to $\tau_B = (d/2)^2/D \approx 170$ s. Although thermal tearing or the creation of new pinning connections does alter the distribution of obstacles, the pinned particles remain fixed on the time scale of our measurements ($\approx 60\ \tau_B$). Applying an external magnetic field H perpendicular to the substrate plane, dipole moments are induced. Due to the parallel alignment of dipoles, the pair interaction scales with the inverse cube of the particle separation. The pair interaction strength can be readily expressed by the dimensionless parameter [38]

$$\Gamma = \frac{\mu_0 (\chi H)^2}{4\pi a^3 k_B T}, \tag{1}$$

where a is the mean particle distance, χ denotes the magnetic susceptibility, and $k_B T$ is the thermal energy. The definition $a = (\pi n)^{-1/2}$ allows us to calculate the dipolar distance dependence of the pair potential from the 2D particle number density n (including a geometrical prefactor). By changing the magnetic field, the system can be effectively "heated" or "cooled" homogeneously. We study the melting process in three sample regions with varying pinning fractions, ranging from approx. 0.5% to 0.8%. While the entire system comprises $>10^5$ particles, each monitored region contains $\approx 5 \times 10^3$ particles. The colloidal ensemble is melted from an equilibrated crystalline state by decreasing H in small steps. After each step, the system is allowed to equilibrate for at least 24 h before particle trajectories are recorded for 2.7 h via video microscopy [39].

III. SIMULATION

Additionally, we perform computer simulations of point-like superparamagnetic particles in two dimensions which interact via the purely repulsive pair potential of parallel dipoles. Standard metropolis Monte Carlo (MC) simulations were conducted on the NAT ensemble, with A denoting the area of the square simulation cell. The particle number was fixed at $N = 16\,000$ and periodic boundary conditions were applied. Particle interactions are calculated via the truncated

and shifted potential,

$$U(r_{ij}) = \begin{cases} \Gamma((r_{ij}/a)^{-3} - (r_c/a)^{-3}), & r_{ij} < r_c, \\ 0, & r_{ij} \geqslant r_c, \end{cases} \quad (2)$$

where the cutoff radius $r_c/a = 10$ is chosen. The initial state of the simulation is obtained by successively attempting to place particles at random positions within the simulation cell, while the minimum distance between particles is restricted to $r_{ij} \geqslant a$. The resulting configurations corresponds to an isotropic liquid of hard disks with a packing fraction of 0.25%. Quenched disorder is introduced by pinning a randomly chosen subset of particles to their initial position and rendering them immobile for the entire simulation run. Within statistical accuracy, this procedure models the distribution of pinning sites observed in the experiment. Each particular pinning fraction is sampled with at least 15 statistically independent distributions of pinned particles. Although typically MC methods are employed to study static properties in equilibrium states, the underlying phase-space sampling provides a suitable means for studying dynamic processes too [40]. To estimate the Brownian time scale in terms of MC sweeps (i.e., attempted moves per particle), the diffusion of particles is observed in a dilute bulk suspension. Thus, we find that the experimental Brownian time τ_B corresponds to ≈36 MC sweeps. Starting in the isotropic fluid phase ($\Gamma^{-1} = 0.0167$), a full freezing and melting cycle is conducted for each pinning configuration. Note that during this process, the particular distribution of pinned particles remains fixed. At each step of Γ, the system is equilibrated for up to 5×10^5 MC sweeps (≈13 800 τ_B), after which data are acquired over 10^5 MC sweeps. For each pinning fraction explored, the observables obtained at a given value of Γ are averaged over all sample realizations of disorder. As a reference, the same freezing and melting cycle is conducted for a pure bulk system, where all particles are mobile.

IV. METHODS

Sixfold orientational order can be expressed in terms of the bond order parameter

$$\psi_{6,j} = \frac{1}{n_j} \sum_{k=1}^{n_j} e^{i6\theta_{jk}}, \quad (3)$$

where the sum goes over all n_j nearest neighbors of particle j, and θ_{jk} is the angle of the kth bond with respect to a certain reference axis. For a particle embedded in a perfect hexagonal crystal at zero temperature, the magnitude of ψ_6 is 1. It decreases as the neighbor particles deviate from their ideal lattice positions, e.g., almost vanishes for a five- or sevenfold coordinated defect. Here, nearest neighbors of a particle are determined via the Voronoi construction. In order to analyze orientational clusters and fluctuations of the order parameter, we consider the local time-averaged director $\Psi_{6,i}$,

$$\Psi_{6,i}(t) = \frac{1}{\Delta_t} \int_{t-\Delta_t}^{t} \psi_{6,i}(t')dt'. \quad (4)$$

For both experiment and simulation, the averages are conducted over a time frame $\Delta_t/\tau_B \geqslant 50$. Furthermore, the global

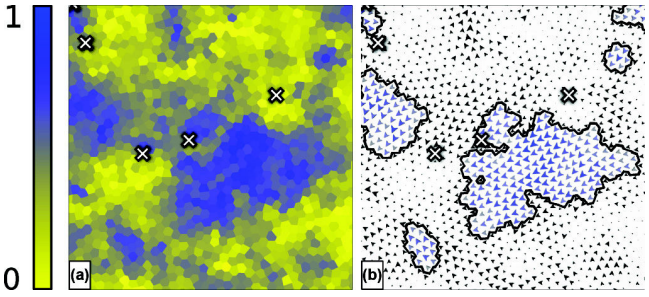

FIG. 1. (Color online) Simulation snapshots illustrating orientational clusters close to the fluid → hexatic transition ($\Gamma^{-1} = 0.0149$). The field of view corresponds to 450×450 μm (≈7% of the simulation cell). (a) Voronoi cells color-coded based on the time-averaged local orientational order parameter $\Psi_6(t)$. Colors are specified by the bar at the left. Crosses indicate the positions of pinned particles. (b) Orientational director field, where the complex number $\Psi_{6,i}(t)$ is shown as a 2D vector, the size of which corresponds to the magnitude of $\Psi_{6,i}(t)$. Outlines of clusters are indicated in black.

time-averaged director Ψ_6 is defined by

$$\Psi_6(t) = \frac{1}{N} \sum_{i=1}^{N} \Psi_{6,i}(t). \quad (5)$$

Orientational clusters are determined via two criteria. First, for a particle to be included in a cluster at time t, the time-averaged order parameter has to meet the criterion

$$|\Psi_{6,i}(t)| \geqslant 0.5. \quad (6)$$

If particle i is included in a cluster, so may be a neighboring particle j, if it meets criterion (6) and the sixfold director has a common orientation. Therefore, we consider the angle ϕ_{ij} between the real projection of $\Psi_{6,i}(t)$, $\Psi_{6,j}(t)$ and impose the limit

$$\cos(\phi_{ij}) = \frac{\Psi_{6,i} \cdot \Psi_{6,j}}{|\Psi_{6,i}||\Psi_{6,j}|} \geqslant 0.984. \quad (7)$$

The application of these two criteria is illustrated in Fig. 1.

V. CLUSTER ANALYSIS

Applying the criteria introduced in the previous section to the data recorded in computer simulation and experiment, the formation of clusters is examined within the two-step melting process. Therefore, the reduced transition temperatures Γ_i^{-1} and Γ_m^{-1} are inherited from our previous study [37], where the KTHNY melting scenario was confirmed for the system at hand. In the same work, it was shown that there is a broadening of the hexatic phase for increased pinning fractions (see Fig. 2). While Γ_i^{-1} is hardly affected, Γ_m^{-1} shifts from ≈0.0146 to ≈0.0144 as the pinning fraction is increased from 0.1% to 0.5%. These findings are based on an analysis of the spatial and dynamic bond order correlation function. Furthermore, we analyzed the orientational correlation time ξ_t and an "effective" Frank's constant K_A, which is the modulus of torsional stiffness in the presence of pinned particles. Our data indicate that in the presence of disorder, the divergent behavior of Frank's constant is shifted to lower temperatures for higher pinning strengths [37]. Since the divergence of K_A coincides

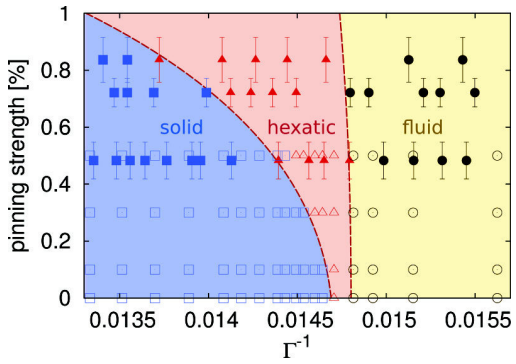

FIG. 2. (Color online) Phase diagram indicating the solid [blue (dark gray)], hexatic fluid [red (medium gray)], and isotropic fluid [yellow (light gray)] phases in the parameter space of the temperature $\propto\Gamma^{-1}$ and pinning strength. Filled symbols represent experimental data, while open symbols correspond to simulation results [37].

with the hexatic → solid transition, this implies a strong dependency of T_m on disorder, as proposed in Refs. [26]–[28]. In the following, we revisit the continuous, disorder-induced melting scenario in the context of the development and characteristics of orientational clusters and examine how the latter are influenced by pinning. Figure 3 illustrates the formation of clusters in two exemplary systems with pinning fractions of 0.1% and 0.5%, respectively. Snapshots are shown at three distinct temperature steps, which, for a pinning fraction of 0.1%, cover all three phases. In the isotropic fluid phase close to Γ_i^{-1} [Figs. 3(a) and 3(d)], a substantial number of separate clusters can be observed. However, the orientation of these clusters is strongly heterogeneous. In the hexatic phase [Figs. 3(b) and 3(e)], the formerly separated clusters have merged into a large cluster with a homogeneous orientation. Note that, in general, the formation of a uniform cluster does not necessarily collapse with the isotropic → hexatic transition point and is highly dependent on the cluster criteria stated in Sec. IV.

As reported in [37], orientational order undergoes spatiotemporal fluctuations throughout the hexatic phase. These critical-like fluctuations occur on time scales beyond the orientational correlation time and are consistent with the continuous nature of the phase transition. In terms of orientational clustering, these fluctuating regions correspond to particles not included in clusters. For further clarification, computer simulation snapshots illustrating the time evolution of clusters on different time scales are shown in Fig. 4. We find the temperature range in which these spatiotemporal patterns occur to depend strongly on the pinning fraction. At $\Gamma^{-1} \approx 0.0146$, the fluctuations have subsided in the system with a pinning fraction of 0.1% [Fig. 3(c)], while there are still substantial fluctuations in the system with a pinning fraction of 0.5% [Fig. 3(f)]. Starting from this qualitative observation, we systematically study the co-occurrence of orientational clusters and disordered, fluctuating regions by tracking several quantities related to the formation of clusters versus the effective temperature Γ^{-1} for various pinning fractions. First, we measure the abundance of clusters at each specific temperature step. Therefore, the number of clusters is averaged over an observation window of $\approx 10\tau_B$ for the experimental data and $>2000\ \tau_B$ for the simulation data. In the computer simulation, the result is additionally

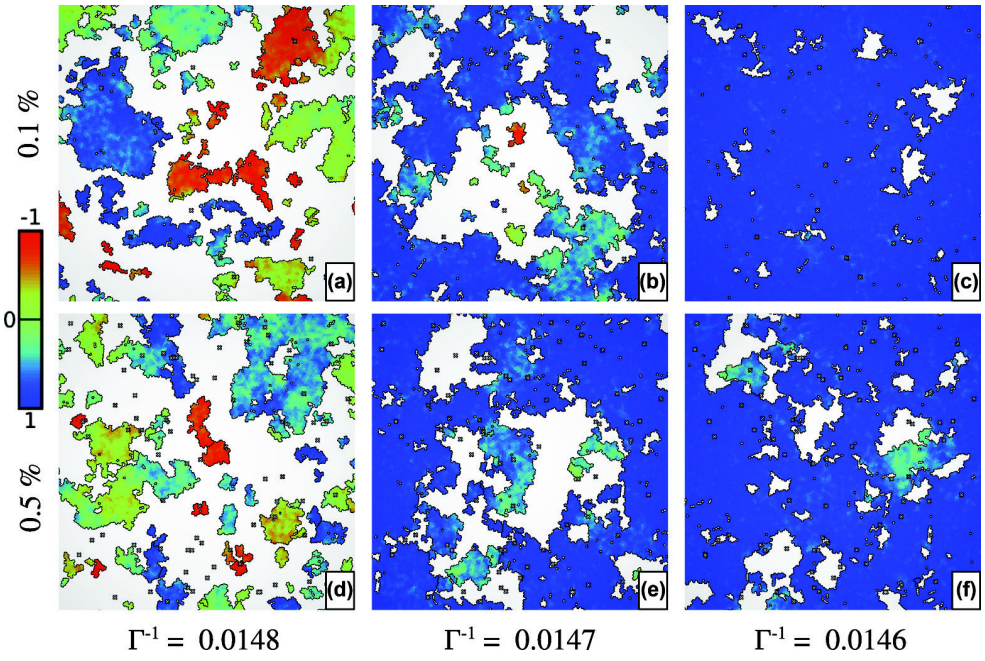

FIG. 3. (Color online) Simulation snapshots of exemplary configurations for pinning fractions 0.1% (a–c) and 0.5% (d–f). Voronoi cells are shown for particles included in clusters. The color-code corresponds to the bar at the left, based on the normalized product $\Psi_{6,i} \cdot \Psi_6/(|\Psi_{6,i}||\Psi_6|)$. Crosses indicate the positions of pinned particles. At $\Gamma = 0.0148$, both systems are in the isotropic fluid phase; the transition to the hexatic phase occurs at $\Gamma = 0.0147$. At $\Gamma = 0.0146$, the system with less pinning enters the solid phase (c), while the system with a higher pinning fraction remains in the hexatic phase (f) and fluctuations persist.

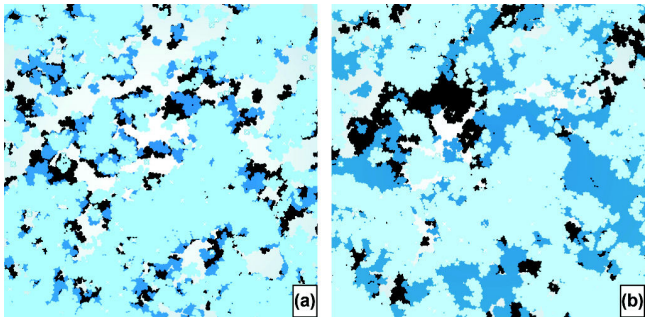

FIG. 4. (Color online) Fluctuating clusters in the hexatic phase ($\Gamma^{-1} = 0.0147$, 0.5% pinning). (a) Cluster configurations at three time steps: t_0 [black], $t_0 + 35\tau_B$ [medium blue (gray)], and $t_0 + 70\tau_B$ [light blue (light gray)]. Voronoi cells are shown for particles included in a cluster. (b) Cluster configurations at three time steps: t_1 [black], $t_1 + 700\tau_B$ [medium blue (gray)], and $t_0 + 1400\tau_B$ [light blue (light gray)]. Snapshots are from the computer simulation.

averaged over all realizations of disorder for a specific pinning fraction. Our results are shown in Fig. 5; note that in order to account for the different system sizes in experiment and simulation, the cluster number is normalized with respect to the average total particle number $\langle N \rangle$. For both experiment and simulation, we observe that in the fluid phase, the number of clusters N_C is high. Close to the isotropic → hexatic transition temperature $\Gamma_i^{-1} \approx 0.0147$, the number decreases sharply and saturates towards small values close to 1 throughout the hexatic phase. Correspondingly, the normalized number of clusters approaches 0. This behavior corresponds to the observation of cluster formation in Fig. 3. Additionally, our results capture the influence of pinning disorder on the abundance of clusters: The number of clusters observed at a pinning fraction of 0.5% systematically exceeds the one observed at 0.1% pinning over a broad, intermediate temperature interval, which coincides

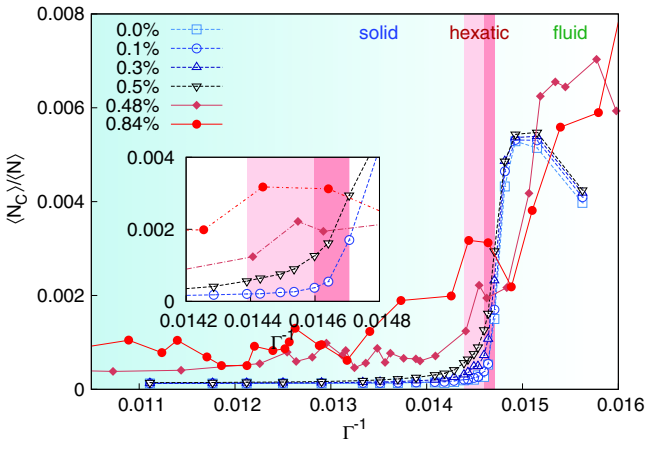

FIG. 5. (Color online) Average of the normalized number of orientational clusters $\langle N_C \rangle / \langle N \rangle$ versus the effective temperature for different pinning strengths. Experimental data are plotted with filled symbols, while open symbols represent numerical data. Lines are guides for the eye. The temperature range of the hexatic phase for 0.1% pinning is highlighted in red (medium gray); the widening of the hexatic phase at 0.5% pinning is illustrated in light red (light gray). Inset: Closeup of the average cluster number.

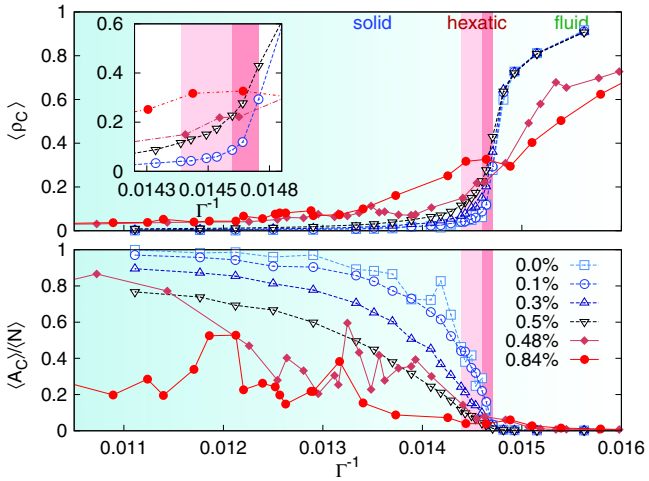

FIG. 6. (Color online) Top: Average ratio $\langle \rho_C \rangle$ of particles outside of clusters versus effective temperature. Inset: Closeup of the behavior in the hexatic phase. Bottom: Average size $\langle A_C \rangle / \langle N \rangle$ of clusters stated as a fraction of the average total particle number. Experimental data are plotted with filled symbols; open symbols represent numerical data. Lines are guides for the eye. As in Fig. 5, the temperature range of the hexatic phase is highlighted in red (gray) for two distinct pinning fractions.

with the widened temperature range of the hexatic phase. This picture is supported by the analysis of fluctuating disordered regions, i.e., regions excluded from clusters. We track the average number density of particles which are excluded from clusters versus the effective temperature, at which the averaging routine depicted above is applied. For every time step, the number of particles excluded from clusters is detected and divided by the total number of particles. The resulting number density ρ_C is averaged over all time steps in the observation window. Our results are shown in Fig. 6 (top). We find that the ratio of particles excluded from clusters is close to 1 in the isotropic fluid, drops sharply around Γ_i^{-1}, and approaches 0 at lower temperatures. In agreement with the previous discussion, an increase in the pinning fraction results in a weaker decay of this ratio below Γ_i^{-1}; i.e., a given ratio of excluded particles is maintained over a broader temperature interval than in the case of lower disorder. Again, this temperature interval collapses with the broadened regime of the hexatic phase reported in [37].

As the third quantity, the average size of clusters is shown in Fig. 6 (bottom) for various pinning fractions. The average number of particles included in a single cluster is stated as a fraction of the average total particle number $\langle N \rangle$. This analysis indicates that the formation of clusters spanning the entire system is inhibited by pinning disorder. Instead, the division of the system into a multitude of clusters persists over a broader temperature interval such that, on average, clusters are smaller. Note that for the experimental data, there is less averaging and the average size of clusters fluctuates strongly. However, the qualitative influence of pinning disorder is captured by both experimental and numerical data. The qualitative resemblance of cluster formation in the pure case and in the presence of disorder implies that the emergence of fluctuating orientational clusters is intrinsic to the two-stage melting scenario, not just

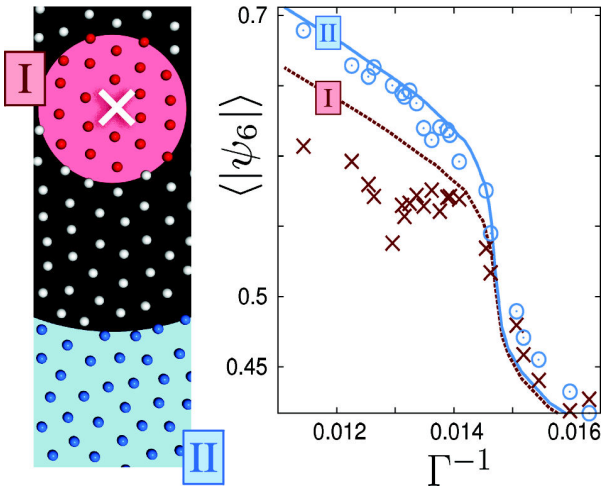

FIG. 7. (Color online) Left: Computer simulation snapshot illustrating the subdivision into regions close to (I) and far from (II) pinned particles. Right: Instantaneous value of the order parameter ψ_6 in regions I and II versus the effective temperature Γ^{-1}. Lines correspond to computer simulation data (pinning fraction, 0.5%); experimental data are represented by symbols (crosses, region I; circles, region II; pinning fraction, 0.48%).

an effect introduced by the presence of pinned particles. As reported in [37], an increase in the pinning fraction induces a shift of T_m towards lower values. Here, this behavior is reflected by the inhibited formation of orientational clusters.

For a closer investigation of the impact of pinning disorder on the formation of orientational clusters, we introduce a subdivision of the system into three regions. Region I represents the vicinity of pinned particles and comprises all particles within a radius of $8d$ around a pinning site (including the pinned particles themself). Region II contains all particles which are more than $24d$ away from the closest pinning center, thus being presumably unaffected by pinning disorder. Particles contained in neither region I nor region II are neglected for the purpose of the following analysis. The subdivision of the system according to these criteria is illustrated in Fig. 7 (left). We analyze the magnitude of the instantaneous bond orientational order parameter ψ_6 in regions I and II, respectively. Our results are shown in Fig. 7 (right). A general trend can be observed: On average, orientational order is reduced in the vicinity of pinned particles (region I) compared to distant particles (region II). This effect is especially pronounced in the hexatic and solid phase. No significance can be detected in the isotropic fluid phase, which is expected to be caused by the intrinsic large degree of disorder in an isotropic system.

As a further step, we consider the conditional probability for a particle being part of a cluster, given the fact that the particle belongs to region I or II, respectively (Fig. 8). Thereby, we observe that in the isotropic fluid, particles in region I are in fact slightly *more* likely to be included in a cluster than particles in region II. Thus, the emergence of small clusters at $T > T_i$ occurs preferentially in the vicinity of pinned particles. However, this behavior is inverted at lower temperatures. In the hexatic and solid phase, where single clusters cover large parts of the system, particles in the neighborhood of pinning

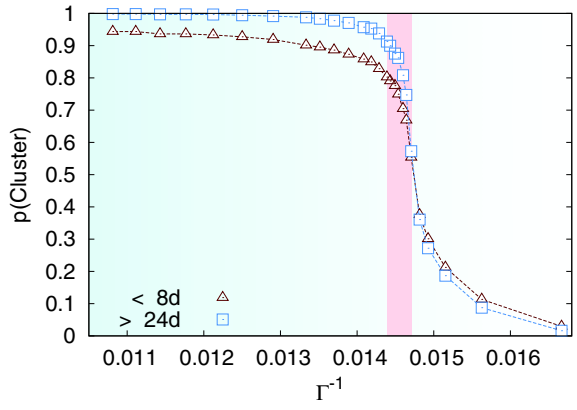

FIG. 8. (Color online) Conditional probability that a particle belongs to a cluster given that it is located in region I (triangles) or region II (squares) versus effective temperature Γ^{-1}. Data were obtained with computer simulations; the pinning fraction corresponds to 0.5%. Lines are guides for the eye. The temperature range of the hexatic phase is highlighted in light red (gray).

sites are significantly *less* likely to be part of a cluster. Thus, at low temperatures, pinned particles inhibit the formation of clusters by deteriorating orientational order in their vicinity, while they stabilize orientational order at high temperatures. This result is in good agreement with a previous analysis of the dynamic properties of particles in regions I and II [37]. Thereby, it was found that the long-term dynamics of particles close to pinning sites is inhibited in the fluid phase, while in the solid phase, particles in region I exhibit increased dynamics compared to those in region II. Interestingly, increased or decreased dynamics are correlated to low or high orientational order, respectively.

In order to verify the continuous nature of the phase transition, we calculate the probability distribution $p(\Psi_L^2)$ of the squared order parameter Ψ_L^2. We perform a finite-size analysis by considering various subcell sizes, $L = 1/2$, $1/4$, $1/8$, and $1/16$, where L states the side length of a subcell as a fraction of the side length of the total system. For a continuous phase transition, we expect the probability distribution to exhibit a single peak for all temperatures and on all length scales. Our results are shown in Fig. 9 and are in agreement with the continuous nature of the melting process. The probability distribution of $p(\Psi_L^2)$ is shown for a broader range of temperatures for the fixed subcell size $L = 1/4$ in Fig. 10.

VI. DEFECT ANALYSIS

Following the KTHNY theory, the 2D melting process is driven by the unbinding of topological defects. Specifically, bound dislocation pairs break into isolated dislocations above T_m, marking the solid $\rightarrow$ hexatic transition. Above T_i, dislocations dissociate into single disclinations. The existence of isolated dislocations (i.e., pairs of five- and sevenfold defects) leads to quasi-long-range orientational order and is the fingerprint of the hexatic phase. We approach the hexatic phase by tracking the density of defects, in particular, the number of isolated dislocations. Numerically, isolated dislocations are identified as a fivefold and a sevenfold defect particle

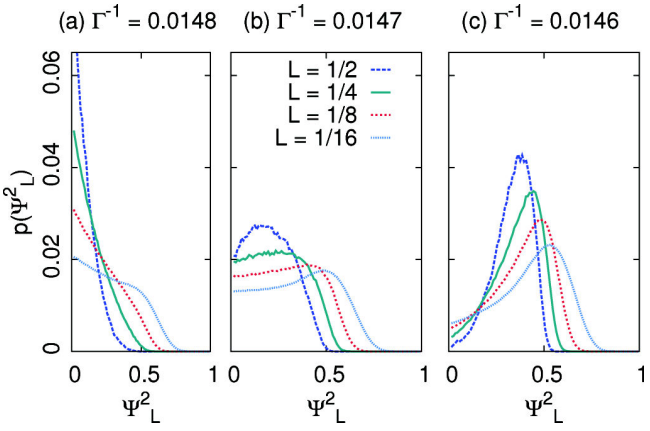

FIG. 9. (Color online) Finite-size analysis of the probability distribution of Ψ_L^2 calculated for subcells of side length L (stated as a fraction of the total box length). Curves are shown for computer simulation data; the pinning fraction corresponds to 0.5%. (a) $\Gamma^{-1} = 0.0148$: isotropic fluid phase, where the peak of the probability distribution is located at $\Psi_L^2 = 0$. (b) $\Gamma^{-1} = 0.0147$: fluid $\rightarrow$ hexatic transition, where the peak shifts to intermediate values of Ψ_L^2. (c) $\Gamma^{-1} = 0.0146$: hexatic phase.

which are Voronoi neighbors, and additionally, both have exactly one defect particle in their neighborhood (which is the respective counterpart). Thus, we exclude entangled chains, grain boundaries, and agglomerations of defect particles. However, as discussed in [14], this definition does not exclude close but nonadjacent pairs of dislocations, which, for a sufficiently large Burgers circuit, yield a 0 Burgers vector. Furthermore, the application of periodic boundary conditions affects the counting of defect particles [14]. Since these sources of miscounting affect all our data, a qualitative comparison between defect densities at different pinning fractions is still valid. Additionally, we track the density of bound dislocations, which are as well defined in a way that excludes entanglements

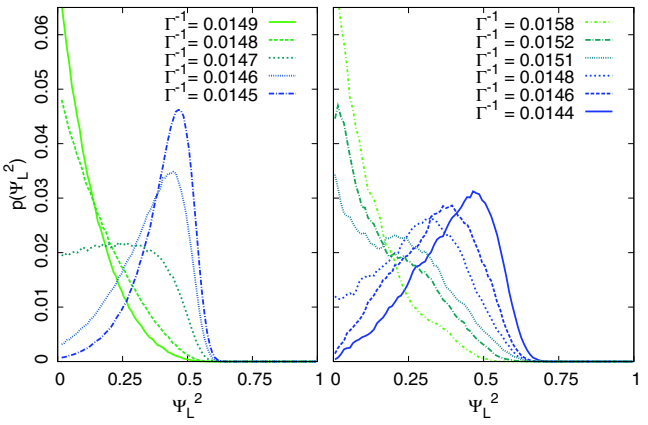

FIG. 10. (Color online) Probability distribution of Ψ_L^2 for simulation (left) and experiment (right) for $L = 1/4$ (stated as a fraction of the total system dimension). During the crossover from isotropic to hexatic fluid, the location of the peak shifts from $\Psi_L^2 = 0$ to intermediate values. The distribution has a single distinct peak, indicating a continuous transition. The pinning fraction is 0.5% in the simulation and 0.48% in the experiment.

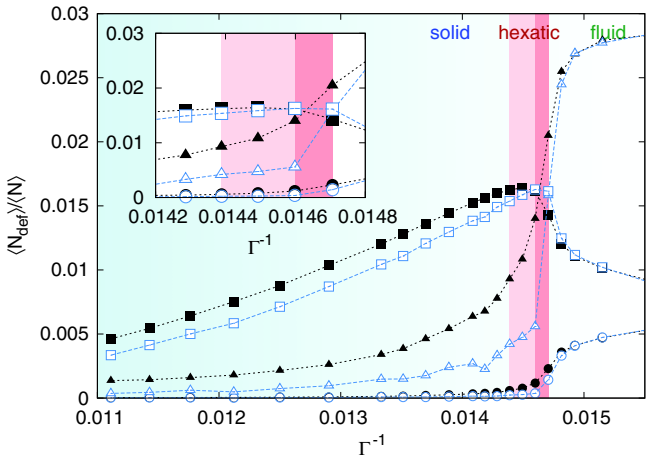

FIG. 11. (Color online) Defect density $\langle N_{\rm def}\rangle/\langle N\rangle$ versus effective temperature. The number of particles forming bound dislocations (squares), isolated dislocations (triangles), or single five- or sevenfold disclinations (circles) is stated as a fraction of the total particle number. Data correspond to computer simulations with pinning fraction 0.1% [open (blue) symbols] and 0.5% (filled black full symbols). Lines are guides for the eye. The common temperature range of the hexatic phase for both pinning fractions is highlighted in red (medium gray). For 0.5% pinning, the widened range of the hexatic phase is shown in light red (light gray). Inset: Closeup on the defect density in the (widened) hexatic phase.

and agglomerations of defects. Therefore, we track adjacent pairs of dislocations with no additional defect particles in the Voronoi neighborhood. Finally, single disclinations are tracked, where five- and sevenfold disclinations are treated alike. Figure 11 depicts the recorded defect densities in the computer simulation for two pinning fractions versus the effective temperature. The densities stated are calculated as the total number of particles involved in topological defects of the given kind, $N_{\rm def}$, divided by the total number of particles N. For example, 1 isolated dislocation among 100 particles yields a density of 0.02, and 1 bound dislocation among 100 particles yields 0.04. In some analogy to findings reported in [14], we observe that not only single disclinations, but also (isolated) dislocations are abundant in the isotropic fluid phase as well. Below the transition temperature to the hexatic regime, the density of both single disclinations and isolated dislocations decays, while the density of bound dislocations rises, indicating the formation of bound dislocation pairs. We find that increasing the fraction of pinned particles from 0.1% to 0.5% leads to a slight systematic increase in all the defect densities, which reflects the fact that pinned particles severly impair translational order. Since, in general, pinned particles are not placed at ideal lattice positions, additional defects have to be introduced in order to accommodate them in a crystal. Furthermore, increasing the fraction of pinned particles has a pronounced effect on the density of isolated dislocations. While for a pinning fraction of 0.1%, the density of isolated dislocations drops sharply at $\Gamma^{-1} = 0.0146$, a comparably high density of isolated dislocations is maintained over a broader temperature interval for a pinning fraction of 0.5%. Corresponding to previous findings, this temperature

range coincides with the widened range of the hexatic phase reported in [37]. Thus, the increased density of isolated dislocations at higher pinning fractions reflects our previous finding of a broadened hexatic phase on the level of topologic defects.

VII. CONCLUSIONS

We have presented a detailed analysis of the formation and dynamics of orientational clusters and the development of topological defects in the context of the disorder-induced melting scenario in two dimensions. Our results are obtained for superparamagnetic colloids whose repulsion strength can be tuned by an external magnetic field. The colloids are confined at a water-substrate interface where quenched disorder is realized by substrate-induced particle pinning. In addition, corresponding computer simulations of 2D parallel dipoles have been performed. We find that the formation of orientational clusters is intrinsically adapted for the two-stage melting scenario and strongly dependent on the strength of quenched disorder. While the solid is characterized by single cluster formation and large cluster sizes, the cluster density and the number of particles outside of clusters increase sharply in the hexatic phase and saturate in the isotropic fluid. The average cluster size decreases continuously towards the hexatic-isotropic transition and drops to 0 in the isotropic fluid. Throughout the melting process (especially at the solid-hexatic transition), quenched disorder favors the formation of multiple clusters and, equivalently, reduces the average cluster size, but simultaneously the number of particles which do not belong to a cluster increases. This reduces the orientational correlation in space and time due to cluster fluctuations and is directly reflected in the local probability analysis where we detected a reduced cluster formation in the proximity of pinned particles in the solid phase, while clusters are preferentially formed close to pinned particles in the isotropic fluid. In this context, the widening of the hexatic phase due to quenched disorder is directly coupled to the distinct (disorder-dependent) characteristics of orientational cluster formation. The development of topological defects shows a similar effect; especially the creation of isolated dislocations is strongly increased by quenched disorder at the solid-hexatic transition.

Future works should address the effect of long-range quenched potentials, which were originally discussed by Nelson [26], and short-range disorder, e.g., fluctuations of quenched external potentials on the scale of particle diameters [32]. This could be explored via various kinds of external potentials on different length scales, from strong pinning via light fields [41] to weak attractive interactions on precisely structured substrates. Alternatively, density functional theory [42–44] or the phase-field crystal model [45] could be a starting point to describe the hexatic phase [46–48], which could, in principle, be formulated also for quenched disorder [49,50]. The behavior of an externally disturbed system under nonequilibrium conditions, e.g., temperature quenches, should be of interest: Concerning the competition between critical fluctuations and first-order characteristics, complex nonequilibrium relaxation dynamics might be induced by quenched disorder. In the absence of disorder, such systems were studied in both one-component [25] and two-component [24] systems and revealed interesting properties. Last, but not least, other types of disorder should be explored systematically, including rough disordered substrates and disorder which is not quenched on the time scale of the measurements.

ACKNOWLEDGMENTS

We thank T. Neuhaus and C. V. Achim for helpful discussions. This work was supported by the DFG within the SFB TR6 (Projects C2, C,3 and C4) and by the HHU graduate school POROSYS.

[1] J. M. Kosterlitz and D. J. Thouless, J. Phys. C **5**, L124 (1972).
[2] J. M. Kosterlitz and D. J. Thouless, J. Phys. C **6**, 1181 (1973).
[3] B. I. Halperin and D. R. Nelson, Phys. Rev. Lett. **41**, 121 (1978).
[4] D. R. Nelson and B. I. Halperin, Phys. Rev. B **19**, 2457 (1979).
[5] A. P. Young, Phys. Rev. B **19**, 1855 (1979).
[6] N. D. Mermin, Phys. Rev. **176**, 250 (1968).
[7] S. T. Chui, Phys. Rev. B **28**, 178 (1983).
[8] M. Glaser and N. Clark, Adv. Chem. Phys. **83**, 543 (1993).
[9] K. J. Strandburg, Rev. Mod. Phys. **60**, 161 (1988).
[10] Y. Saito, Phys. Rev. Lett. **48**, 1114 (1982).
[11] H. Weber, D. Marx, and K. Binder, Phys. Rev. B **51**, 14636 (1995).
[12] E. P. Bernard and W. Krauth, Phys. Rev. Lett. **107**, 155704 (2011).
[13] A. H. Marcus and S. A. Rice, Phys. Rev. Lett. **77**, 2577 (1996).
[14] Y. Han, N. Y. Ha, A. M. Alsayed, and A. G. Yodh, Phys. Rev. E **77**, 041406 (2008).
[15] S. Prestipino, F. Saija, and P. V. Giaquinta, Phys. Rev. Lett. **106**, 235701 (2011).
[16] Y. Peng, Z. Wang, A. M. Alsayed, A. G. Yodh, and Y. Han, Phys. Rev. Lett. **104**, 205703 (2010).
[17] S. Z. Lin, B. Zheng, and S. Trimper, Phys. Rev. E **73**, 066106 (2006).
[18] N. Gribova, A. Arnold, T. Schilling, and C. Holm, J. Chem. Phys. **135**, 054514 (2011).
[19] R. E. Kusner, J. A. Mann, J. Kerins, and A. J. Dahm, Phys. Rev. Lett. **73**, 3113 (1994).
[20] K. Zahn and G. Maret, Phys. Rev. Lett. **85**, 3656 (2000).
[21] H. H. von Grünberg, P. Keim, K. Zahn, and G. Maret, Phys. Rev. Lett. **93**, 255703 (2004).
[22] P. Keim, G. Maret, and H. H. von Grünberg, Phys. Rev. E **75**, 031402 (2007).
[23] P. Dillmann, G. Maret, and P. Keim, J. Phys.: Condens. Matter **20**, 404216 (2008).
[24] L. Assoud, F. Ebert, P. Keim, R. Messina, G. Maret, and H. Löwen, Phys. Rev. Lett. **102**, 238301 (2009).
[25] P. Dillmann, G. Maret, and P. Keim, Phase transition in two dimensions far from thermal equilibrium, arXiv:1303.6821.

[26] D. R. Nelson, Phys. Rev. B **27**, 2902 (1983).
[27] S. Sachdev and D. R. Nelson, J. Phys. C-Solid State Physics **17**, 5473 (1984).
[28] M.-C. Cha and H. A. Fertig, Phys. Rev. Lett. **74**, 4867 (1995).
[29] S. Herrera-Velarde and H. H. von Grünberg, Soft Matter **5**, 391 (2009).
[30] R. E. Kusner, J. A. Mann, and A. J. Dahm, Phys. Rev. B **49**, 9190 (1994).
[31] A. Pertsinidis and X. S. Ling, Phys. Rev. Lett. **100**, 028303 (2008).
[32] D. Carpentier and P. Le Doussal, Phys. Rev. Lett. **81**, 1881 (1998).
[33] P. Yunker, Z. Zhang, and A. G. Yodh, Phys. Rev. Lett. **104**, 015701 (2010).
[34] T. Kawasaki and H. Tanaka, J. Phys.: Condens. Matter **23**, 194121 (2011).
[35] J. Schockmel, E. Mersch, N. Vandewalle, and G. Lumay, Phys. Rev. E **87**, 062201 (2013).
[36] P. Hartmann, A. Douglass, J. C. Reyes, L. S. Matthews, T. W. Hyde, A. Kovacs, and Z. Donko, Phys. Rev. Lett. **105**, 115004 (2010).
[37] S. Deutschländer, T. Horn, H. Löwen, G. Maret, and P. Keim, Phys. Rev. Lett. **111**, 098301 (2013).
[38] In Ref. [37], this expression was erroneously given without a prefactor $1/4\pi$.
[39] F. Ebert, P. Dillmann, G. Maret, and P. Keim, Rev. Sci. Instrum. **80**, 083902 (2009).
[40] K. Binder, Rep. Prog. Phys. **60**, 487 (1997).
[41] T. O. E. Skinner, S. K. Schnyder, D. G. A. L. Aarts, J. Horbach, and R. P. A. Dullens, arXiv:1302.2896 (2013).
[42] Y. Singh, Phys. Rep. **207**, 351 (1991).
[43] H. Löwen, Phys. Rep. **237**, 249 (1994).
[44] S. van Teeffelen, N. Hoffmann, C. N. Likos, and H. Löwen, Europhys. Lett. **75**, 583 (2006).
[45] H. Emmerich, H. Löwen, R. Wittkowski, T. Gruhn, G. I. Tóth, G. Tegze, and L. Gránásy, Adv. Phys. **61**, 665 (2012).
[46] V. N. Ryzhov and E. E. Tareyeva, Phys. Rev. B **51**, 8789 (1995).
[47] V. N. Ryzhov and E. E. Tareyeva, Physica A **314**, 396 (2002).
[48] A. Jaiswal, S. L. Singh, and Y. Singh, Phys. Rev. E **87**, 012309 (2013).
[49] M. Schmidt, Phys. Rev. E **66**, 041108 (2002).
[50] P. P. F. Wessels, M. Schmidt, and H. Löwen, Phys. Rev. Lett. **94**, 078303 (2005).

2) Fluctuations of orientational order and clustering in a two-dimensional colloidal system under quenched disorder	
Journal	Physical Review E
Impact Factor	2.326
Authorship	1st author
Contribution	40%
	Computer simulations and data analysis

Eur. Phys. J. Special Topics **222**, 2961–2972 (2013)

DOI: 10.1140/epjst/e2013-02069-8

THE EUROPEAN PHYSICAL JOURNAL SPECIAL TOPICS

Review

Two-dimensional colloidal mixtures in magnetic and gravitational fields

H. Löwen, T. Horn, T. Neuhaus, and B. ten Hagen

Institut für Theoretische Physik II: Weiche Materie, Heinrich-Heine-Universität Düsseldorf, 40225 Düsseldorf, Germany

Received 6 September 2013 / Received in final form 17 September 2013
Published online 25 November 2013

Abstract. This mini-review is concerned with two-dimensional colloidal mixtures exposed to various kinds of external fields. By a magnetic field perpendicular to the plane, dipole moments are induced in paramagnetic particles which give rise to repulsive interactions leading to complex crystalline alloys in the composition-asymmetry diagram. A quench in the magnetic field induces complex crystal nucleation scenarios. If exposed to a gravitational field, these mixtures exhibit a brazil–nut effect and show a boundary layering which is explained in terms of a depletion bubble picture. The latter persists for time-dependent gravity ("colloidal shaking"). Finally, we summarize crystallization effects when the second species is frozen in a disordered matrix which provides obstacles for the crystallizing component.

1 Introduction

When colloids are confined to interfaces [1–3], almost perfect two-dimensional systems can be realized [4–6]. The key idea is to consider a pending water droplet at a glass plate which is filled with superparamagnetic particles, see also [7]. Due to gravity the particles sediment down until they meet the air-water interface. Since the surface tension of the air-water interface is high, the particles do not penetrate through the interface as this would create additional interfacial area. Consequently, the particles are confined to the interface by a combination of gravity acting downwards and interfacial free energy keeping them upwards. Since the water droplet containing the colloidal particles is macroscopic, its air-water interface is flat on a micron scale typical for an interparticle spacing between the colloids.

This set-up can be combined with an external magnetic field B, which induces magnetic dipole moments in the particles, $m \propto B$. This in turn results in a dipole-dipole interaction between the particles. All dipole moments are along the magnetic field direction. If the external magnetic field is perpendicular to the interface, there is a repulsive interaction between the particles which can be described by a pairwise potential scaling as the inverse cube of the distance [8]. The prefactor scales with the square of the magnetic dipole moment, i.e., with the square of the magnetic field strength B. By tuning the magnetic field B, one can thus readily change the interaction strength. For inverse power-law interactions, this corresponds formally to a change of temperature or density. The experimental set-up is typically combined with

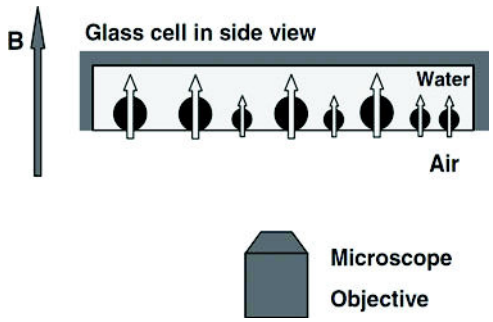

Fig. 1. Schematic view of the set-up: binary mixture of superparamagnetic colloidal particles at an air-water interface in an external magnetic field B perpendicular to the plane. From Ref. [22].

video-microscopy in order to visualize the individual particle trajectories. A schematic view for the set-up in case of a binary suspension is shown in Fig. 1.

In the last decades, progress has been achieved for one-component and two-component systems which is outlined as follows: for one-component systems, the Kosterlitz–Thouless–Halperin–Nelson–Young scenario was confirmed on this strictly two-dimensional system [9]. Moreover, it was verified that Young's modulus approaches 16π at the melting temperature [10] as predicted by the theory. The modulus of orientational stiffness was measured in the hexatic phase at the fluid-hexatic transition and found to be in agreement with theory, too [11]. Since the creation of disclinations and dislocations is crucial for the melting scenario, the pair interaction of dislocations has been determined in these two-dimensional crystals [12]. Finally, the crystal phonon dispersion relations [13] have been determined and found to be in full quantitative agreement with theoretical calculations [14]. For the crystallization behavior [15], dynamical density functional theory was developed and applied to magnetic particles [16,17].

If the external magnetic field is tilted relative to the surface normal, anisotropic dipole-dipole interactions between the particles result. The zero-temperature phase diagram was calculated by lattice sums [8] revealing a wealth of anisotropic stable solid lattices in agreement with experimental data. The Lindemann parameters in the anisotropic crystals were determined in good agreement between experiment and theory [18]. The melting of the anisotropic crystals is again mediated by defects [19] as in the isotropic case and the resulting intermediate phase can be called "smectic-like".

Two-component (binary) systems with big and small magnetic dipole moments represent ideal glass formers in two spatial dimensions [20]. Several structural and dynamical features of these mixtures have been explored including the long-time self diffusion [21] and the partial clustering of the small particles at moderate interaction strengths [22]. The latter is revealed by an unusual peak in the partial structure factor of the small-small pair correlations.

In this paper, we review more recent progress obtained by theory and simulation for two-dimensional colloidal binary mixtures in magnetic and gravitational fields and compare the results to experimental studies [7]. The mini-review is organized as follows: in Sect. 2 we start with bulk phase behavior of binary dipolar mixtures. Real-space experimental data for the partial pair correlations are compared to simulations for a binary mixture and good agreement is found. Moreover the equilibrium phase diagram is discussed and an ultrafast quench to cool down the system is described. Then effects of confinement are presented briefly, too. In Sect. 3 the combination of a magnetic field and perpendicular in-plane gravity is studied and a colloidal

brazil–nut effect is found and explained in terms of a simple effective Archimedian theory. Finally, in Sect. 4, we consider binary mixtures of mobile and immobile particles and explore the freezing transition in this system with quenched disorder. We conclude in Sect. 5.

2 Crystallization of two-dimensional colloidal mixtures in magnetic fields

A binary mixture of super-paramagnetic colloidal particles pending at an air-water interface is an excellent realization of a 2D classical many-body system [20–23]. An external magnetic field B perpendicular to the interface induces parallel dipole moments m_{A} and m_{B} in particles A and B, respectively, resulting in an effective repulsive interaction which scales as the inverse cube of the distance r within the monolayer. By defining the magnetic susceptibilities per particle A and B as $\chi_{\mathrm{A,B}} = m_{\mathrm{A,B}}/B$, we obtain the pair potential,

$$V_{\alpha\beta}(r) = \chi_\alpha \chi_\beta \frac{B^2}{r^3}. \tag{1}$$

Note that only for low B the induced dipole moment is linearly proportional to the external field, and then χ_α is field-independent. In this case, for a fixed relative composition x_{B} and susceptibility ratio $\tilde{m} \equiv m_{\mathrm{B}}/m_{\mathrm{A}} = \chi_{\mathrm{B}}/\chi_{\mathrm{A}}$, all static quantities depend solely on the coupling parameter [24],

$$\Gamma = \frac{\chi_{\mathrm{A}}^2 B^2}{k_{\mathrm{B}} T \Delta_{\mathrm{A}}^3}, \tag{2}$$

where $k_{\mathrm{B}}T$ is the thermal energy and $\Delta_{\mathrm{A}} = (n_{\mathrm{A}})^{-1/2}$ is the mean distance between particles A [25], with n_{A} denoting the partial number density of A-particles.

2.1 Fluid pair structure

Structural correlations of binary mixtures have been studied in great detail [21,26–28]. Figure 2 shows a recent comparison between experimental and simulation data for the three partial pair correlation functions $g_{\mathrm{AA}}(r)$, $g_{\mathrm{AB}}(r)$, and $g_{\mathrm{BB}}(r)$ [26]. Except for a fine substructure in $g_{\mathrm{BB}}(r)$, there is very good overall agreement. Higher-order structural correlations, e.g., particles with a square-like and triangular-like surrounding have also been studied [26,29]. These building blocks are essential for understanding the onset of glass formation.

2.2 Equilibrium bulk phase diagram

At zero temperature (i.e., for $\Gamma \to \infty$), the state of the binary system is completely determined by the susceptibility ratio $\tilde{m}$ (varying in the range $0 \le \tilde{m} \le 1$) and the relative composition x_{B} of species B (with smaller dipole moment). A wealth of different stable phases occur. The topology of the phase diagram is getting more complex with increasing asymmetry [30], see also [31,32]. For small asymmetries $\tilde{m}$ and intermediate compositions x_{B}, the system splits into triangular A_2B and AB_2 phases. Experiments with colloidal dipolar mixtures, which were performed for a strong asymmetry of $\tilde{m} \simeq 0.1$, confirmed the predicted crystalline structures [28], however, only in the form of small crystalline patches. Recent results were also obtained for the phonon band structure [33] and crystal structures in tilted magnetic fields [34]. For another application to colloid polymer mixtures see [35].

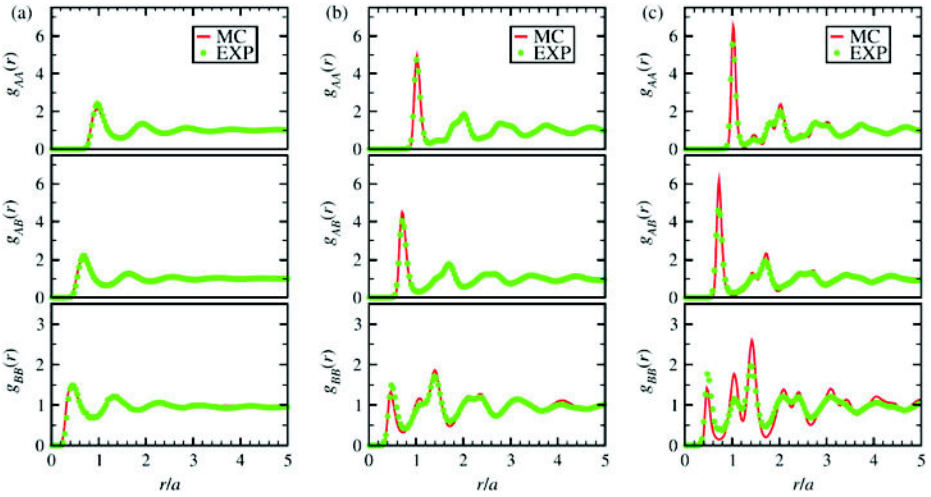

Fig. 2. Partial radial pair distribution functions $g_{AA}(r)$, $g_{BB}(r)$, and $g_{AB}(r)$. Experimental data (EXP) are compared to Monte Carlo simulation results (MC) for three different dimensionless coupling strengths Γ. (a) $\Gamma = 4.9$, (b) $\Gamma = 38.9$, and (c) $\Gamma = 82.9$. The relative composition of B–particles is fixed at $x_B = 0.29$. From Ref. [26].

2.3 Ultrafast quenching

By suddenly increasing the magnetic field, the system can be quenched on a time scale which is much smaller than single particle motion [36]. Since magnetic field strength corresponds formally to an inverse temperature, an ultrafast temperature quench can be realized experimentally, which is very difficult for molecular systems. Analyzing the particle configuration after a rapid quench reveals some local crystalline patches in the glass [28,30]. These patches correspond to the thermodynamic bulk crystal [37], demonstrating an interplay between vitrification and crystallization [38–41]. Experimental snapshots just after the quench and well after the quench are shown in Fig. 3. Within the allotted time, the binary mixture does not find its true ground state but shows patches with local square and triangular order. The fraction of particles with this local order grows with time, see Fig. 3, and there is good agreement between Brownian dynamics simulations and real-space experiments [27].

2.4 Crystallization at system boundaries

Similar quenches for magnetic mixtures were studied by Brownian dynamics simulations near a structured wall [42] which is modeled by fixed particles on an alternating binary equimolar square lattice cut along the (10) direction. This wall favors local crystallites which pick up the square symmetry of the substrate. The equilibrium state is an alternating square lattice which coincides exactly with that imposed by the external wall. After the quench, it is found that the number and structure of crystallites near the walls strongly depend on the wall pattern. Even though local square structures are favored energetically and the equilibrium state is an alternating square lattice, the number of triangular crystallites close to the wall which has outermost fixed small particles is significantly higher than in the unconfined case. This effect is not contained in classical nucleation theory.

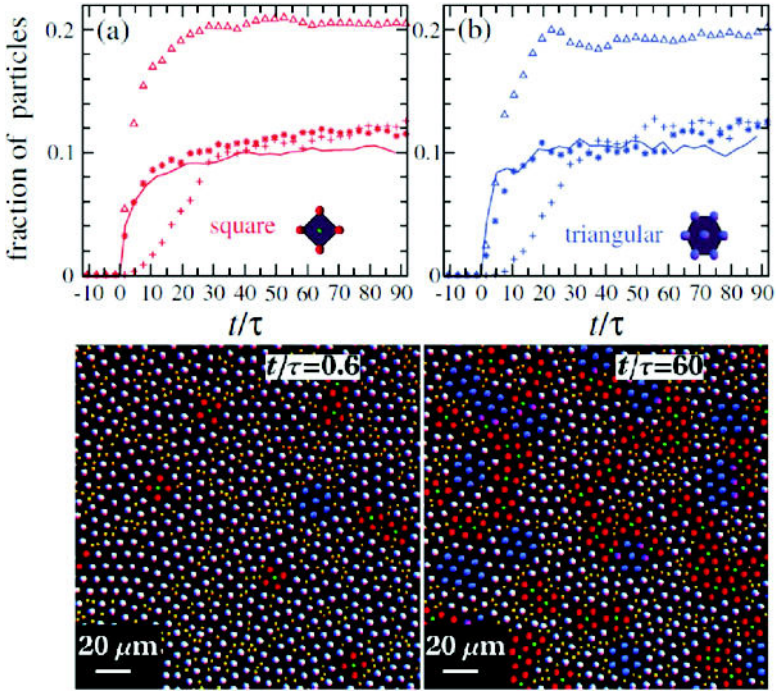

Fig. 3. (a) Fraction of B-particles belonging to a crystalline square surrounding (see inset) and (b) fraction of A-particles belonging to a crystalline triangular surrounding (see inset) versus reduced time after an ultrafast quench. The lines are experimental data while the symbols (*) are data from Brownian dynamics simulations. Two experimental snapshots for a time just after the quench (left configuration) and a later time (right configuration) are shown. Big particles are shown in blue if they belong to a triangular surrounding and in red if they belong to a square surrounding. All other big particles are shown in white. Few big particles belonging to both triangular and square surroundings are shown in pink. The small particles are shown in green if they belong to a square center of big particles, otherwise they appear in yellow. Also included are simulation data for an instantaneous "steepest descent" quench (△) and for a linear increase of the field (+). The relative composition of the small particles is $x_B = 0.4$. For a more detailed explanation of the parameters, see [27]. From Ref. [27].

3 Two-dimensional colloidal mixtures in magnetic fields and under gravity

Exposing the binary magnetic mixture described in Sect. 2 to an in-plane homogeneous gravitational force perpendicular to the magnetic field B leads to interesting newly emerging phenomena. Experimentally, this gravitational force can be realized by tilting the hanging droplet. The two components A, B of the mixture differ in both mass M and magnetic susceptibility χ, where A is chosen as the heavier and more strongly coupled species. Thus, the system is characterized by the dipolar ratio $\tilde{m} = m_B/m_A$ and the mass ratio $\tilde{M} = M_B/M_A$ with $0 \leq \tilde{m}, \tilde{M} \leq 1$. First, the case of a static gravitational field was studied by Monte Carlo computer simulations and mean–field density functional theory. Second, the binary magnetic mixture was examined in the nonequilibrium situation of oscillatory gravity, which is a simple model of colloidal shaking. Thereby, Brownian dynamics simulations and dynamic density functional theory were used to study the dynamic response of the system [43].

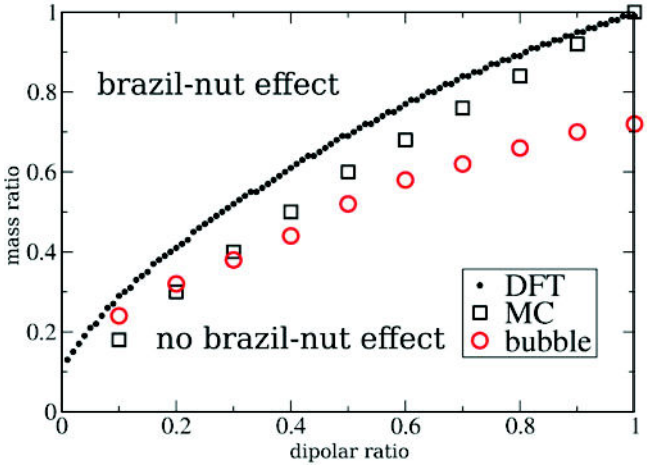

Fig. 4. Separation line between the occurrence of the colloidal brazil–nut effect and the absence of this effect in the parameter space of dipolar ratio $\tilde{m}$ and mass ratio $\tilde{M}$. Monte Carlo simulation data (contoured white squares), density functional data (full black circles) and the transition line implied by the depletion bubble picture (contoured circles) are shown. For other parameters, see Ref. [43]. From Ref. [43].

3.1 Static gravity: Colloidal brazil–nut effect

Monte Carlo (MC) simulations were performed for various mass ratios $0 \leq \tilde{M} \leq 1$, while the dipolar ratio was fixed to $\tilde{m} = 0.1$ according to recent experimental samples [27,28]. Thereby, a very distinct behavior of the sedimenting mixture could be observed. While for very asymmetric masses, the lighter B-particles are on top of the heavier A-particles as expected, the behavior is reversed for intermediate B-particle masses: here, the heavier A-particles are on top of the lighter B-particles. At first glance, this opposite trend is counterintuitive. In some analogy to granulate matter, it is called the (colloidal) *brazil–nut effect* [44].

The mechanism behind this effect can be explained using an intuitive picture: due to their strong repulsive interaction, particles of species A create a depletion zone of less repulsive particles around them reminiscent of a bubble. Applying Archimedes' principle effectively to this bubble, an A-particle can be lifted in a fluid background of B-particles. This "depletion bubble" mechanism results in the brazil–nut effect, where the heavier A-particles float on top of the lighter B-particles.

By systematically scanning the entire parameter space $0 \leq \tilde{m} \leq 1, 0 \leq \tilde{M} \leq 1$, the line separating the brazil–nut effect from the ordinary behavior (no brazil–nut effect) was mapped, see Fig. 4. Density functional theory predictions are in good agreement with the MC simulation results, predicting the same trends and the same slope of the separation line in the parameter space of mass and dipolar ratio. Additionally, the intuitive depletion bubble picture provides a simple theory for the separation line based on an effective buoyancy criterion, which is included in Fig. 4 and reproduces the simulation data pretty well.

The depletion bubble picture also implies a layering of A-particles close to the hard bottom wall of the confining container (at $y = 0$), which is demonstrated by an actual simulation snapshot shown in Fig. 5. This effect is due to an effective attraction of an A-particle towards the hard container bottom wall: if a single A-particle is fixed at a given distance from the bottom wall, its depletion bubble is reduced since the void space is cut by the hard wall, see the sketch in Fig. 6. Since the A-particle is point-like, it can approach the wall very closely. Note that in Fig. 6, particles are

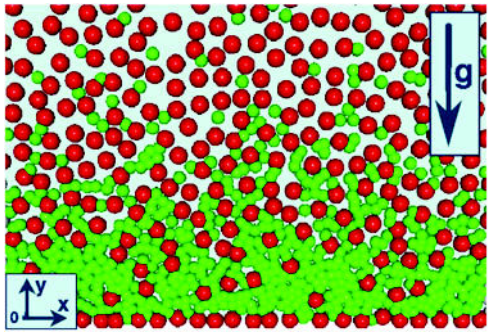

Fig. 5. Simulation snapshot for $\tilde{m} = 0.1$, $\tilde{M} = 0.5$ showing the marked-off bottom layer of heavy A-particles (large red spheres) at $y = 0$ beneath the fluid of light B-particles (small green spheres). The arrow indicates the direction of gravity, $-y$. From Ref. [43].

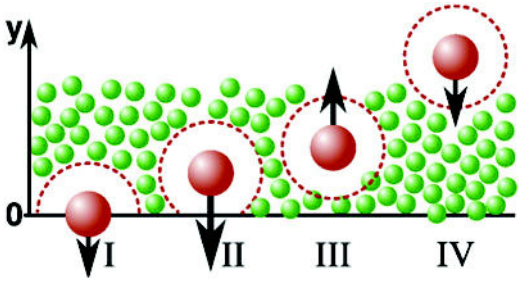

Fig. 6. Schematic illustration of the metastable trapping of A-particles at $y = 0$, leading to the formation of a boundary layer. A-particles are represented by large red spheres, while B-particles are depicted as smaller green spheres. Note that particles are represented as spheres with a finite radius for clarity only while in the computer simulation, point particles are considered. The solid line indicates $y = 0$, while the orientation is analogous to Fig. 5. The depletion zone surrounding A-particles is indicated by a dashed outline. From Ref. [43].

represented as spheres with finite radii for clarity, and the center of the sphere corresponds to the position of the point particle. In the computer simulation, the hard wall is implemented by systematically rejecting particle moves beyond the wall, such that the position of the point particle (i.e., the center of the spheres in Fig. 6) is restricted to $y > 0$. Experimentally, this wall could be realized by a lithographic wall on a substrate or by an array of tweezers. If the A-particle is close to the wall, the void space is half of the full circle in the bulk (situations I and III in Fig. 6). If the height y of the A-particles increases, the depletion bubble area grows, which causes two opposing effects: first, in order to increase the depletion bubble area, work against the osmotic pressure of the fluid B-particles is necessary, which leads to an effective attraction of the particle to the wall. Second, the effective buoyancy of the bubble containing the A-particle leads to a repulsive force with respect to the wall.

3.2 Time-dependent gravity

Furthermore, the binary magnetic mixture was examined under time-dependent gravity, where the gravitational potential was conveniently modeled as a stepwise constant function of time. In particular, the case of a non-zero time-average of the gravity was considered. Brownian dynamics (BD) simulations and dynamic density functional theory (DDFT) were used to study the dynamic response of the system. In an

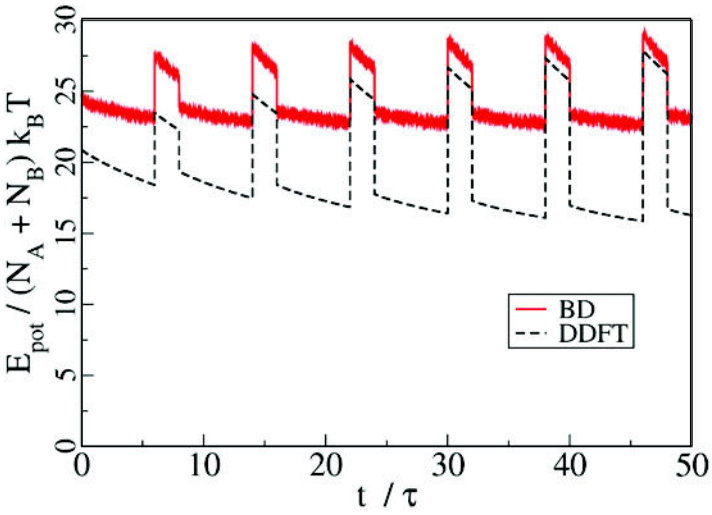

Fig. 7. Total potential energy $E_{\rm pot}/(N_{\rm A}+N_{\rm B})k_BT$ per particle versus reduced time t/τ. The parameters are $\tilde{m}=0.1, \tilde{M}=0.24$. From Ref. [43].

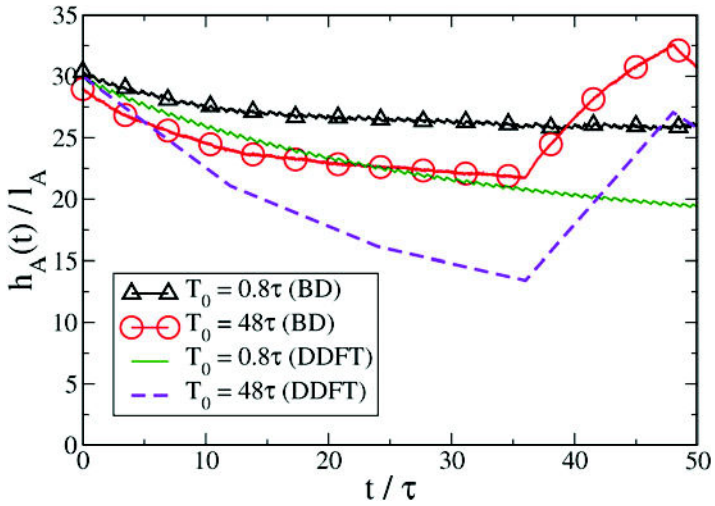

Fig. 8. Time-evolution of the reduced mean A-particle height $h_{\rm A}(t)$ versus reduced time t/τ for different shaking periods T_0. The parameters are $\tilde{m}=0.1, \tilde{M}=0.24$. From Ref. [43].

experimental setup, the case of a time-dependent in-plane gravitational force could be realized by periodically tilting the hanging droplet in opposite directions.

The relaxation of an initially homogeneous (but interacting) fluid of A- and B-particles towards its periodic steady state can be monitored by observing the instantaneous ensemble-averaged total potential energy $E_{\rm pot}$ of the system [27]. This quantity is shown in Fig. 7, indicating that only few oscillations are needed to get into the steady behavior. Due to the homogeneous starting configuration, the energy oscillation amplitude increases with time. DDFT describes all trends correctly and also provides reasonable data for the potential energies and the associated relaxation time.

The dynamical response of the whole system can be probed by examining the time-dependent averaged height of each particle species as shown for species A in Fig. 8. Upon shaking, the boundary layer of the A-particles persists. Comparing the

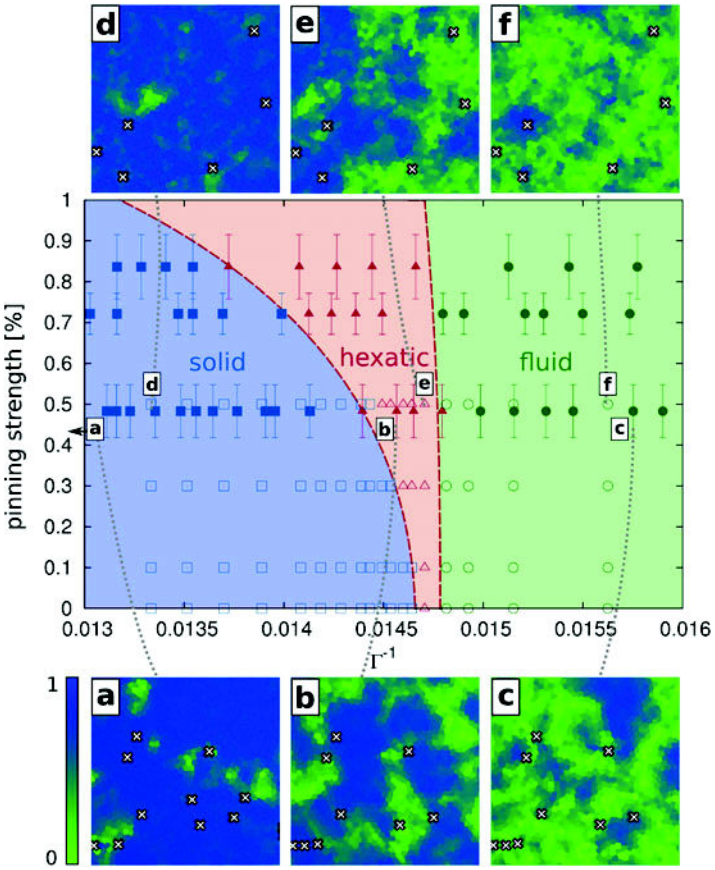

Fig. 9. Phase diagram indicating solid (blue), hexatic (red), and fluid (green) phase in the parameter space of temperature $\propto 1/\Gamma$ and pinning strength, which corresponds to the percentage of immobile particles. Full symbols represent experimental data, while contoured points correspond to simulation results. The snapshots show the orientational order in the experimental (a-c) and simulated system (d-f). Only a small section of the system is shown. Voronoi cells are color-coded based on the value of the time-averaged orientational order parameter $\langle|\psi_6|\rangle_t$ according to the color bar on the left. Crosses indicate the position of immobile particles. From Ref. [45].

computer simulation results to the density profiles predicted by DDFT in more detail, the persistence of the boundary layer is contained by both methods.

4 Quenched disorder: Mixtures of mobile and immobile magnetic colloids

Recently, the influence of quenched disorder on the two-dimensional freezing behavior was studied by using both video-microscopy of superparamagnetic confined colloidal particles and computer simulations of two-dimensional repulsive parallel dipoles [45]. A fraction of the particles was pinned to a substrate providing quenched disorder. Similar to the set-up depicted in Sect. 1, the interaction strength was controlled by an external magnetic field, giving rise to parallel dipolar interactions. In the pure case of a

one component system, the Kosterlitz–Thouless–Halperin–Nelson–Young (KTHNY) [46,47] scenario was unambiguously confirmed [11,48]. It predicts a two-stage melting scenario with an intervening hexatic phase which is separated from the fluid and solid phases by two continuous transitions [49], where the melting process is mediated by the unbinding of thermally activated topological defects. In particular, the emergence of the hexatic phase is related to the dissociation of dislocation pairs into isolated dislocations [50]. These break translational symmetry, leading to a vanishing shear modulus. However, the *orientational* symmetry remains quasi-long-range and the modulus of rotational stiffness, Frank's constant K_A, attains a nonvanishing value.

By systematically increasing the fraction of pinned particles, the freezing process was studied in the presence of disorder. The occurrence of the KTHNY scenario with an intermediate hexatic phase was confirmed even for a system with quenched disorder. The hexatic phase was detected by analyzing the temporal correlation $g_6(t)$ of the bond order parameter [51]. It decays exponentially with time in the fluid and algebraically in the hexatic phase, while it reaches a constant value in the solid. The data obtained by Monte Carlo computer simulation and experiment were mapped to the parameter plane of temperature and pinning strength to obtain a phase diagram (Fig. 9) in which the transition lines for the solid-hexatic and hexatic-fluid transition are resolved. While the fluid-hexatic transition remains largely unaffected by disorder, the hexatic-solid transition shifts towards lower temperatures for increasing disorder resulting in a significantly broadened stability range of the hexatic phase.

Extracting an "effective" K_A, the scaling of the elasticity modulus was recovered in the presence of disorder. Thereby, evidence was found that melting in the presence of disorder is governed by the same defect-mediated process predicted and confirmed for pure systems.

5 Conclusions

In conclusion, binary mixtures of superparamagnetic colloids at a pending air-water interface are excellent model systems to explore freezing and glass formation in two-dimensional systems, also at one-dimensional interfaces and with quenched disorder. It is evident that in the future more complex problems can be solved including the effect of linear shear flow [52] and the correct incorporation of hydrodynamic interactions between the colloidal particles, which affect the non-equilibrium microstructure. The latter was recently incorporated in a strictly two-dimensional system for nonequilibrium band formation in oscillatory-driven mixtures [53]. It is important to note that hydrodynamic interactions in the quasi-two-dimensional monolayer are different from those in a bulk suspension [54], where during sedimentation, the displaced fluid can flow back "above" the particle monolayer. Also, the long-time dynamics of fluid demixing in nonadditive systems would be an interesting system, which has also been explored in a complex plasma [55].

Tilting the plane may lead to brazil–nut effects in equilibrium. But a time-dependent tilt can also result in transient laning of the two particle species. Lane formation was first found in computer simulations [56,57] and more recent simulations in two dimensions have shown that laning is a continuous transition [58]. Moreover, a microscopic theory for laning was constructed based on the Smoluchowski equation [59].

Magnetic particles can be confined to cavities of various shapes [60,61]. It would be interesting to study the freezing and glass transition in finite systems contained in cavities [62,63]. This would provide an interesting link to complex plasmas where particle clusters in harmonic confinement are studied intensely [1]. Another relevant topic is the transport through channels [64].

The particles can also be exposed to a periodic laser-optical field allowing for new crystalline structures in equilibrium [65]. Finally, magnetic particles can be made active [66]. Two-dimensional swimmers were realized in this way and recent theoretical predictions for the trajectory statistics in the bulk [67] were confirmed [68]. Furthermore, self-propelled particles in shear flow [69] and active crystals [70,71] were studied. Recently, the theoretical predictions for circle swimmers were experimentally verified by measuring the trajectories of colloidal particles self-propelled by self-diffusiophoresis triggered by external light fields [72]. Moreover, kinetic clustering of these self-propelled particles was found [73].

We thank P. Keim, G. Maret, F. Ebert, and S. Deutschländer for the fruitful collaboration. This work was supported by the DFG within SFB TR6 (project C3).

References

1. A. Ivlev, H. Löwen, G. Morfill, C.P. Royall, *Complex Plasmas and Colloidal Dispersions: Particle-resolved Studies of Classical Liquids and Solids*, Series in Soft Condensed Matter (World Scientific, 2012), ISBN: 9789814350068
2. H. Löwen, J. Phys.: Condens. Matter **13**, R415 (2001)
3. H. Löwen, J. Phys.: Condens. Matter **21**, 474203 (2009)
4. K. Zahn, J. M. Mendez-Alcaraz, G. Maret, Phys. Rev. Lett. **79**, 175 (1997)
5. K. Zahn, G. Maret, Curr. Opin. Colloid Interface Sci. **4**, 60 (1999)
6. H. Löwen, R. Messina, N. Hoffmann, C.N. Likos, C. Eisenmann, P. Keim, U. Gasser, G. Maret, R. Goldberg, T. Palberg, J. Phys.: Condens. Matter **17**, S3379 (2005)
7. P. Dillmann, G. Maret, P. Keim, Eur. Phys. J. Special Topics **222**(11), 2941 (2013)
8. V.A. Froltsov, R. Blaak, C.N. Likos, H. Löwen, Phys. Rev. E **68**, 061406 (2003)
9. K. Zahn, R. Lenke, G. Maret, Phys. Rev. Lett. **82**, 2721 (1999)
10. H.H. von Grünberg, P. Keim, K. Zahn, G. Maret, Phys. Rev. Lett. **93**, 255703 (2004)
11. P. Keim, G. Maret, H.H. von Grünberg, Phys. Rev. E **75**, 031402 (2007)
12. C. Eisenmann, U. Gasser, P. Keim, G. Maret, H.H. von Grünberg, Phys. Rev. Lett. **95**, 185502 (2005)
13. P. Keim, G. Maret, U. Herz, H.H. von Grünberg, Phys. Rev. Lett. **92**, 215504 (2004)
14. C. Eisenmann, P. Keim, U. Gasser, G. Maret, J. Phys.: Condens. Matter **16**, S4095 (2004)
15. H. Löwen, Phys. Rep. **237**, 249 (1994)
16. S. van Teeffelen, C.N. Likos, H. Löwen, Phys. Rev. Lett. **100**, 108302 (2008)
17. S. van Teeffelen, R. Backofen, A. Voigt, H. Löwen, Phys. Rev. E **79**, 051404 (2009)
18. V.A. Froltsov, C.N. Likos, H. Löwen, C. Eisenmann, U. Gasser, P. Keim, G. Maret, Phys. Rev. E **71**, 031404 (2005)
19. C. Eisenmann, U. Gasser, P. Keim, G. Maret, Phys. Rev. Lett. **93**, 105702 (2004)
20. H. König, R. Hund, K. Zahn, G. Maret, Eur. Phys. J. E **18**, 287 (2005)
21. M. Kollmann, R. Hund, B. Rinn, G. Nägele, K. Zahn, H. König, G. Maret, R. Klein, J.K.G. Dhont, Europhys. Lett. **58**, 919 (2002)
22. N. Hoffmann, F. Ebert, C. N. Likos, H. Löwen, G. Maret, Phys. Rev. Lett. **97**, 078301 (2006)
23. N. Hoffmann, C.N. Likos, H. Löwen, J. Phys.: Condens. Matter **18**, 10193 (2006)
24. J.-P. Hansen, I.R. MacDonald, *Theory of Simple Liquids* (Academic, London, 2006)
25. H. Löwen, E.C. Oğuz, L. Assoud, R. Messina, Adv. Chem. Phys. **148**, 225 (2012)
26. L. Assoud, F. Ebert, P. Keim, R. Messina, G. Maret, H. Löwen, J. Phys.: Condens. Matter **21**, 464114 (2009)
27. L. Assoud, F. Ebert, P. Keim, R. Messina, G. Maret, H. Löwen, Phys. Rev. Lett. **102**, 238301 (2009)
28. F. Ebert, P. Keim, G. Maret, Eur. Phys. J. E **26**, 161 (2008)
29. H. König, Europhys. Lett. **71**, 838 (2005)

30. L. Assoud, R. Messina, H. Löwen, Europhys. Lett. **80**, 48001 (2007)
31. J. Fornleitner, F.F. Lo Verso, G. Kahl, C. N. Likos, Soft Matter **4**, 480 (2008)
32. J. Fornleitner, F. Lo Verso, G. Kahl, C.N. Likos, Langmuir **25**, 7836 (2009)
33. J. Fornleitner, G. Kahl, C.N. Likos, Phys. Rev. E **81**, 060401 (2010)
34. A. Chremos, C.N. Likos, J. Phys. Chem. B **113**, 12316 (2009)
35. B. Lonetti, M. Camargo, J. Stellbrink, C. N. Likos, E. Zaccarelli, L. Willner, P. Lindner, D. Richter, Phys. Rev. Lett. **106**, 228301 (2011)
36. P. Dillmann, G. Maret, P. Keim, J. Phys.: Condens. Matter **20**, 404216 (2008)
37. A. Chowdhury, B.J. Ackerson, N.A. Clark, Phys. Rev. Lett. **55**, 833 (1985)
38. M. Bayer, J.M. Brader, F. Ebert, M. Fuchs, E. Lange, G. Maret, R. Schilling, M. Sperl, J.P. Wittmer, Phys. Rev. E **76**, 011508 (2007)
39. T. Hamanaka, A. Onuki, Phys. Rev. E **75**, 041503 (2007)
40. A. Widmer-Cooper, P. Harrowell, Phys. Rev. Lett. **96**, 185701 (2006)
41. T. Kawasaki, T. Araki, H. Tanaka, Phys. Rev. Lett. **99**, 215701 (2007)
42. L. Assoud, R. Messina, H. Löwen, Mol. Phys. **109**, 1385 (2011)
43. T. Kruppa, T. Neuhaus, R. Messina, H. Löwen, J. Chem. Phys. **136**, 134106 (2012)
44. A. Esztermann, H. Löwen, Europhys. Lett. **68**, 120 (2004)
45. S. Deutschländer, T. Horn, H. Löwen, G. Maret, P. Keim, Phys. Rev. Lett. **111**, 098301 (2013)
46. B. Halperin, D.R. Nelson, Phys. Rev. Lett. **41**, 121 (1978)
47. A.P. Young, Phys. Rev. B **19**, 1855 (1979)
48. K. Zahn, G. Maret, Phys. Rev. Lett. **85**, 3656 (2000)
49. K.J. Strandburg, Rev. Mod. Phys. **60**, 161 (1988)
50. J.M. Kosterlitz, D.J. Thouless, J. Phys. C **6**, 1181 (1973)
51. D.R. Nelson, *Phase Transition and Critical Phenomena* (Academic Press, London, 1983)
52. R. Blaak, S. Auer, D. Frenkel, H. Löwen, Phys. Rev. Lett. **93**, 068303 (2004)
53. A. Wysocki, H. Löwen, J. Phys.: Condens. Matter **23**, 284117 (2011)
54. B. Cichocki, M.L. Ekiel-Jezewska, G. Nägele, E. Wajnryb, Europhys. Lett. **67**, 383 (2004)
55. A. Wysocki, C. Raeth, A.V. Ivlev, R.K. Sütterlin, H.M. Thomas, S.A. Khrapak, S.K. Zhdanov, V.E. Fortov, A.M. Lipaev, V.I. Molotkov, O.F. Petrov, H. Löwen, G.E. Morfill, Phys. Rev. Lett. **105**, 045001 (2010)
56. J. Dzubiella, G.P. Hoffmann, H. Löwen, Phys. Rev. E **65**, 021402 (2002)
57. H. Löwen, Soft Matter **6**, 3133 (2010)
58. T. Glanz, H. Löwen, J. Phys.: Condens. Matter **24**, 464114 (2012)
59. M. Kohl, A.V. Ivlev, P. Brandt, G.E. Morfill, H. Löwen, J. Phys.: Condens. Matter **24**, 464115 (2012)
60. R. Bubeck, P. Leiderer, C. Bechinger, Europhys. Lett. **60**, 474 (2002)
61. K. Mangold, J. Birk, P. Leiderer, C. Bechinger, Phys. Chem. Chem. Phys. **6**, 1623 (2004)
62. Z.T. Nemeth, H. Löwen, J. Phys.: Condens. Matter **10**, 6189 (1998)
63. Z.T. Nemeth, H. Löwen, Phys. Rev. E **59**, 6824 (1999)
64. A. Nikoubashman, C.N. Likos, J. Chem. Phys. **133**, 074901 (2010)
65. T. Neuhaus, M. Marechal, M. Schmiedeberg, H. Löwen, Phys. Rev. Lett. **110**, 118301 (2013)
66. R. Dreyfus, J. Baudry, M.L. Roper, M. Fermigier, H.A. Stone, J. Bibette, Nature **437**, 862 (2005)
67. B. ten Hagen, S. van Teeffelen, H. Löwen, J. Phys.: Condens. Matter **23**, 194119 (2011)
68. X. Zheng, B. ten Hagen, A. Kaiser, M. Wu, H. Cui, Z. Silber-Li, H. Löwen, Phys. Rev. E **88**, 032304 (2013)
69. B. ten Hagen, R. Wittkowski, H. Löwen, Phys. Rev. E **84**, 031105 (2011)
70. A.M. Menzel, H. Löwen, Phys. Rev. Lett. **110**, 055702 (2013)
71. J. Bialké, T. Speck, H. Löwen, Phys. Rev. Lett. **108**, 168301 (2012)
72. F. Kümmel, B. ten Hagen, R. Wittkowski, I. Buttinoni, R. Eichhorn, G. Volpe, H. Löwen, C. Bechinger, Phys. Rev. Lett. **110**, 198302 (2013)
73. I. Buttinoni, J. Bialké, F. Kümmel, H. Löwen, C. Bechinger, T. Speck, Phys. Rev. Lett. **110**, 238301 (2013)

3) Two-dimensional colloidal mixtures in magnetic and gravitational fields	
Journal	The European Physical Journal Special Topics
Impact Factor	1.760
Authorship	2nd author
Contribution	20%
	Computer simulations and data analysis

How does a thermal binary crystal break under shear?

Tobias Horn and Hartmut Löwen

Citation: The Journal of Chemical Physics **141**, 224505 (2014); doi: 10.1063/1.4903274
View online: http://dx.doi.org/10.1063/1.4903274
View Table of Contents: http://scitation.aip.org/content/aip/journal/jcp/141/22?ver=pdfcov
Published by the AIP Publishing

THE JOURNAL OF CHEMICAL PHYSICS **141**, 224505 (2014)

How does a thermal binary crystal break under shear?

Tobias Horn[a] and Hartmut Löwen
Institut für Theoretische Physik II: Weiche Materie, Heinrich-Heine-Universität Düsseldorf, D-40225 Düsseldorf, Germany

(Received 14 October 2014; accepted 21 November 2014; published online 9 December 2014)

When exposed to strong shearing, the particles in a crystal will rearrange and ultimately, the crystal will break by forming large nonaffine defects. Even for the initial stage of this process, only little effort has been devoted to the understanding of the breaking process on the scale of the individual particle size for thermalized mixed crystals. Here, we explore the shear-induced breaking for an equimolar two-dimensional binary model crystal with a high interaction asymmetry between the two different species such that the initial crystal has an intersecting square sublattice of the two constituents. Using Brownian dynamics computer simulations, we show that the combination of shear and thermal fluctuations leads to a characteristic hierarchical breaking scenario where initially, the more strongly coupled particles are thermally distorted, paving the way for the weakly coupled particles to escape from their cage. This in turn leads to mobile defects which may finally merge, proliferating a cascade of defects, which triggers the final breakage of the crystal. This scenario is in marked contrast to the breakage of one-component crystals close to melting. Moreover, we explore the orientational dependence of the initial shear direction relative to the crystal orientation and compare this to the usual melting scenario without shear. Our results are verifiable in real-space experiments of superparamagnetic colloidal mixtures at a pending air-water interface in an external magnetic field where the shear can be induced by an external laser field. [http://dx.doi.org/10.1063/1.4903274]

I. INTRODUCTION

The stability of crystalline solids with respect to mechanical stress is a crucial property for the understanding of effects such as microcrack formation and propagation,[1] which have numerous applications ranging from aeronautic engineering[2,3] to the biomechanics of bone fracture.[4,5] Thereby, shear deformation constitutes an elementary source of strain. Colloids pose an ideal model system for studying distortions on the particle scale[6] and allow to access the microscopic processes governing structural changes via experiment[7–22] and computer simulation.[23–32] For one-component systems, the plastic deformation of a strained solid is well-explored and a connection between mesoscopic deformation and atomistic rearrangements has been established.[33–38] Many real solids, however, are multicomponent materials. Examples include metallic alloys[39–47] and crystalline organic networks.[48,49] Therefore, it is important to study the behavior of mixture crystals under strong shear. Even for the initial stage of the shear-induced breaking process of crystals, only little effort has been devoted so far to understanding the underlying mechanism on the particle-resolved scale for thermalized mixed crystals.

Here, we explore the shear-induced breaking of an equimolar two-dimensional binary model crystal with a high interaction asymmetry between the two different species such that the initial crystal has an intersecting square sublattice of the two constituents. Using Brownian dynamics computer simulations, we show that the combination of shear and thermal fluctuations leads to a characteristic hierarchical breaking scenario. In the strained unit cell, aligned displacements of the more strongly coupled particle species open up pathways for the motion of the weakly interacting particle species, thus enabling the creation of vacancy/interstitial pairs. These pathways correspond to a characteristic distortion of the energy landscape encountered by the weakly coupled species and depend on the crystal orientation with respect to the direction of shear. The microscopic mechanism inducing defect formation under shear can be distinguished from the mechanism governing defect formation when the crystal is heated instead of sheared. Our results imply that the location of spontaneously created defects triggers the mesoscopic deformation of the crystal, i.e., the formation of cracks, which is in striking contrast to the behavior of one-component crystals near melting.[36] Furthermore, the breakage of the thermal binary crystal resembles the plastic deformation of amorphous materials,[50–57] where, due to the absence of distinct topological defects, plastic deformation is mediated by localized patterns of nonaffine motion[52,58–64] and can be traced by the inherent stress signature and spatial correlation of plastic events[65–67] or contact force distributions.[68] Our results are verifiable in real-space experiments of superparamagnetic colloidal mixtures at a pending air-water interface in an external magnetic field,[69–73] where the shear can be induced by an external laser field.

The paper is organized as follows: in Sec. II, we describe the binary model crystal. The simulation technique is depicted in Sec. III. Section IV contains a description of our diagnostics and analysis of defects. In Sec. V, we discuss our results for two different shear directions relative to the crystal

[a]thorn@thphy.uni-duesseldorf.de

orientation. We also compare our findings to the melting of the crystal in the absence of shear and to the shear response of a one-component crystal. Additionally, we discuss similarities to the plastic deformation of amorphous media. We conclude in Sec. VI.

II. MODEL

We study the shear deformation of a two-dimensional colloidal crystal composed of two species of point-like particles denoted as species A and B. The particles interact via the purely repulsive pair potential of parallel dipoles and are characterized by different dipole moments m_A and m_B, where the dipolar ratio m_B/m_A is fixed to 0.1 as in previous studies.[71,74] Thus, particle species A denotes the more strongly coupled particles. The crystal contains equal numbers of the two particle species, i.e., $N = N_A + N_B$ with a fixed relative composition $X = N_A/(N_A + N_B) = 0.5$. In the absence of shear, the binary crystal lattice corresponds to the S(AB) pattern specified in Ref. 75, where each particle species forms a quadratic lattice with spacing $a = 1/\sqrt{n_A}$, with n_A denoting the number density of A particles. The lattices of species A and B are shifted relatively by $0.5a$ along each lattice direction, forming a checkerboard structure, see Fig. 1. As elaborated in Ref. 75, the S(AB) lattice is stable for a composition ratio of $X = 0.5$ and a dipolar ratio of 0.1. This structure is very persistent in two dimensional mixtures and was found for granulates[76] and ionic crystals, as well.[77,78] In previous experiments, two-dimensional suspensions were studied by confining superparamagnetic colloidal particles to the air-water interface of a hanging water droplet[10,71,79,80] or to a planar glass substrate.[21,81,82] Parallely aligned dipole moments are induced by applying an external magnetic field H perpendicular to the plane of confinement.

Conveniently, the pair interaction strength can be expressed by the dimensionless parameter

$$\Gamma = \frac{\mu_0(\chi_A H)^2}{4\pi a^3 k_B T}, \tag{1}$$

where μ_0 is the vacuum permeability, χ_A denotes the magnetic susceptibility of particle species A, k_BT is the thermal energy, and a is the lattice constant as specified above. By altering the magnetic field, the colloidal suspension can be effectively "heated" or "cooled" homogeneously.

Accordingly, the species-dependent pair interaction potential is given in units of k_BT by

$$U_{ij}(r) = \Gamma\, m_i m_j (r)^{-3} \qquad i = A, B, \tag{2}$$

where r denotes the particle separation in units of the lattice constant a. Unless otherwise stated, the interaction strength is set to $\Gamma = 44$ such that crystalline order is maintained in the absence of shear flow.[83]

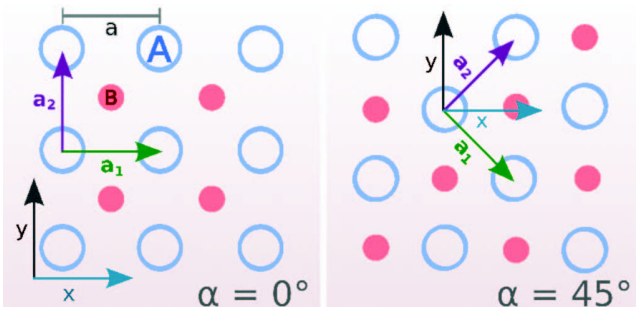

FIG. 1. Schematic representation of the S(AB) lattice with a checkerboard structure of A and B particles. A(B) particles are shown as blue open (red full) circles. The sublattices of both species have a lattice constant a while the two lattices are shifted relatively by $0.5a$ along the lattice vectors $\mathbf{a_1}$, $\mathbf{a_2}$. The direction of shear flow coincides with the x-axis. The angle between $\mathbf{a_1}$ and the x-axis is denoted as α. We consider the cases $\alpha = 0°$ (left) and $\alpha = 45°$ (right).

III. BROWNIAN DYNAMICS SIMULATION

We perform Brownian dynamics (BD) computer simulations of $N = 2048$ pointlike superparamagnetic particles. The ratio of diffusion constants D_B/D_A is fixed to 1.7 corresponding to the physical diameter ratio of comparable experimental samples.[71] The Brownian time of A particles, $\tau_B = a^2/D_A$ is employed as a unit of time, distances are given in units of the lattice constant a. The particles are initially placed on an S(AB) lattice as described in Sec. II, which covers the entire simulation area $L_x \times L_y = 32a \times 32a$. Couette shear flow is imposed in x-direction at a fixed shear rate $\dot\gamma\tau_B = 10^{-3}$ and Lees-Edwards boundary conditions are applied according to the shear flow.[84] The equation of motion governing the particle propagation is given by

$$\begin{aligned} x(t+\delta t) &= x(t) + \frac{D_i}{k_BT}F^{(x)}\delta t + \sqrt{2D_i\delta t}R^{(x)}, \\ &\quad + \dot\gamma(y)\delta t, \\ y(t+\delta t) &= y(t) + \frac{D_i}{k_BT}F^{(y)}\delta t + \sqrt{2D_i\delta t}R^{(y)}, \\ i &= A, B, \end{aligned}$$

where F denotes the force resulting from the particle interaction and $R^{(x)}$, $R^{(y)}$ are randomly distributed numbers with mean 0 and standard deviation 1. The incremental timestep is set to $\delta t/\tau_B = 10^{-5}$. Forces are truncated and shifted according to

$$F_{ij}(r) = \begin{cases} -3\Gamma m_i m_j \left(\frac{1}{r^4} - \frac{1}{r_c^4}\right) & r < r_c \\ 0 & r \geq r_c \end{cases}, \tag{3}$$

where the cutoff is set to $r_c/a = 8$. Simulations are performed over a time range of $t = 200\tau_B$ equaling a total strain window of $\gamma = \dot\gamma t = 0.2$, while configurations are recorded every $10^{-2}\tau_B$. The shear deformation process of the binary S(AB) crystal is analyzed for two different crystal orientations with respect to the direction of shear. In the first setup, the crystal is aligned in such a way that the crystal axis $\mathbf{a_1}$ collapses with the direction of shear, $\alpha = \angle(\mathbf{a_1}, \mathbf{e_x}) = 0°$. In the second setup, the crystal is rotated such that $\alpha = 45°$, see Figure 1. Note that in this setup, we chose $N = 2304$ and $L_x = L_y = 24 \cdot \sqrt{2}a$ in order to accommodate the rotated crystal. Each case is sampled with 64 statistically independent simulation runs. In each run, the initial pure, defect-free crystalline lattice is allowed to relax for $10\tau_B$ before shear is applied. Note that due to the focus on a defect-free initial state, we discard runs in which

topological defects emerge during the initial relaxation phase. This was the case in approximately 8% of the simulation runs.

IV. DIAGNOSTICS AND ANALYSIS OF DEFECTS

In order to track structural distortions over various stages of the deformation process, we devise a cluster criterion, by which topological distortions are detected based on the Voronoi tesselation of a particular configuration. We consider only clusters which are constituted exclusively by A or B particles, respectively. In a perfect S(AB) lattice, every A particle has four A neighbors, each of which shares two B neighbors with the original particle. Neighboring A particles form a cluster if they share less than two neighbors of species B. In the ideal S(AB) lattice, every B particle is enclosed by four neighbors of the opposite species. Neighboring B particles form a cluster if each of them has less than four A neighbors. To grant the proper representation of interstitials, where two B particles occupy the same lattice site, a B particle is also counted as part of the cluster if it has four A neighbors but is within a critical distance to a B particle with less than four A neighbors.[85] For both particle species, clusters are discarded if they contain less than two particles. For clarity, the definition of A and B clusters stated above is exemplified in Fig. 2. The clusters defined by these criteria pose elementary topological distortions of the S(AB) lattice. Specifically, the local appearance of A and B clusters constitutes a primary plastic event which compromises the crystalline structure and may irreversibly distort the crystal by evolving into a stable vacancy/interstitial pair, see Fig. 3.

In order to quantify the lifespan of defects and local distortions, a cluster $\mathcal{C}$ detected in configuration $\mathcal{N} = (\mathbf{r}_1^{\mathbf{A}}, .., \mathbf{r}_{N_A}^{\mathbf{A}}, \mathbf{r}_1^{\mathbf{B}}, .., \mathbf{r}_{N_B}^{\mathbf{B}})$ is considered identical to the cluster $\mathcal{C}'$ detected in the preceding configuration $\mathcal{N}-1$ if at least one of the particles constituting $\mathcal{C}'$ is conserved in $\mathcal{C}$, no other cluster in the current configuration $\mathcal{N}$ contains more particles from $\mathcal{C}'$ than $\mathcal{C}$ and more particles in $\mathcal{C}$ originate from $\mathcal{C}'$ than from any other previous cluster. Thus, we account for fluctuations in the cluster size and composition, cluster recombinations or splits while keeping track of both localized and mobile structural deformations. Since the time interval between two successively recorded configurations is $10^{-2}\tau_B$, this value is set as the lifespan of a cluster which spontaneously emerges and vanishes again in the next configuration recorded.

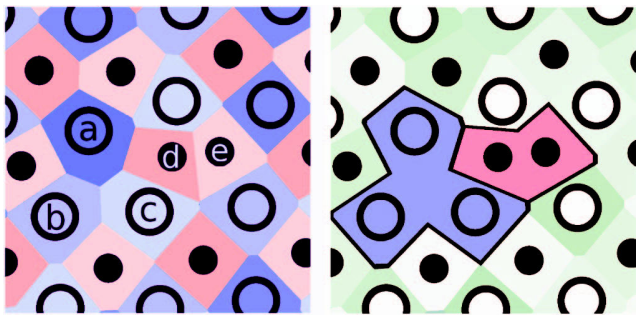

FIG. 2. Computer simulation snapshots exemplifying the definition of clusters based on Voronoi tesselation. A(B) particles are represented by open (full) circles. (Left) Neighboring A particles **a**, **b**, and **c** each share one neighbor of particle species B and thus form a cluster. Also, B particles **d** and **e** form a cluster. Note that particles **e** has less than four neighbors of species A while particle **d** has four A neighbors here but is considered part of the cluster due to the subthreshold distance to cluster particle **e**. Voronoi cells of A(B) particles are colored in shades of blue (red). (Right) Resulting cluster configuration, where Voronoi cells of A(B) particles forming a cluster are colored in blue (red).

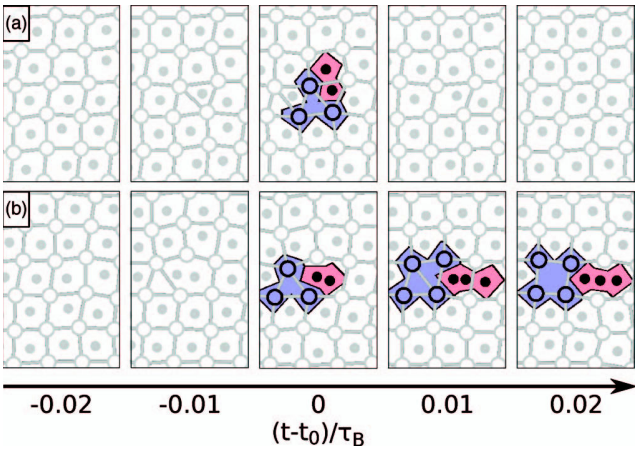

FIG. 3. Computer simulation snapshots illustrating the formation of a temporary (a) and a persistent (b) cluster pair at the time t_0 due to thermal fluctuations. From left to right, each row corresponds to a series of snapshots recorded in intervals of $10^{-2}\tau_B$. The two events shown were recorded in different simulation runs and are uncorrelated. The representation of particles and clusters corresponds to Fig. 2. As a guide to the eye, bonds between adjacent A particles are shown if the separation is less than $1.2a$.

Based on this cluster description, a pattern is established to capture spontaneous attempts to create vacancy/interstitial pairs. These events are detected if they bear the following signature: In configuration $\mathcal{N}$, a cluster $\mathcal{C}_A$ is detected comprising three or more particles of species A. Additionally, a cluster $\mathcal{C}_B$ is detected which is composed of at least two B particles. In the last recorded configuration $\mathcal{N}-1$, $\mathcal{C}_A$ and $\mathcal{C}_B$ did not exist and none of the particles constituting $\mathcal{C}_A$ and $\mathcal{C}_B$ were part of any cluster. Additionally, in configuration $\mathcal{N}-1$, at least one of the B particles in $\mathcal{C}_B$ was a Voronoi neighbor of at least 3 of the A particles forming $\mathcal{C}_A$. This particle is denoted the trigger particle.

The stress induced by the shear flow in x-direction is expressed via the stress tensor component σ_{xy}:[86]

$$\sigma_{xy} = \frac{1}{2}\frac{1}{L_x L_y}\sum_i \sum_{i\neq j} F_{ij}^y(r_{ij}) x_{ij}, \tag{4}$$

where F_{ij}^y denotes the y-component of the dipolar force between particles i and j and r_{ij} (x_{ij}) is the (lateral) distance between the particles in units of the lattice constant a.

V. RESULTS

A. Shear aligned with lattice direction

In the following, we depict the shear deformation process observed for the case $\alpha = 0^\circ$, i.e., for the shear aligned with the lattice direction.

In the *initial stage* of the deformation process, the crystal responds elastically to the applied shear and particle

motion is governed by a uniform affine motion corresponding to the imposed solvent flow. Locally, we observe the formation of short-lived clusters with lifespans of the order $10^{-2}\tau_B$. Particle-scale observations suggest that these events are induced by thermal fluctuations of the A particle species: Deviating from their co-sheared lattice site, single A particles temporarily distort the unit cell symmetry, thus allowing the enclosed B particle to extend its motion into the vacated area and to form a cluster with the B particle of the neighboring unit cell. Simultaneously, the remaining three A particles constituting the original unit cell shift into an unstable triangular arrangement, and a cluster is formed. Starting from a local configuration without any noticeable distortion, these structural disruptions emerge and disappear within a few $10^{-2}\tau_B$. After this time, the original shape of the unit cell is restored. An exemplary sequence of simulation snapshots illustrating a temporary cluster creation due to thermal fluctuations is shown in Fig. 3(a).

The *second stage* of the deformation process is initiated by the creation of a stable pair of clusters with a lifespan of the order τ_B. Qualitatively, the particle motion leading to a persistent defect corresponds to the same pattern depicted above. In addition to the formation of a triangular cluster of A particles, the enclosed B particle is pushed entirely out of the unit cell, enabling the formation of a vacancy/interstitial pair, i.e., a cluster of four A particles which assume a quadratic arrangement around a vacated B lattice site and a cluster including two B particles which occupy the same lattice site (Fig. 3(b)). The B particle cluster created in this process quickly diffuses through the crystal lattice, as the particles constituting the cluster are frequently interchanged. This process is mediated by B particles pushing and replacing each other at the lattice sites touched by the travelling cluster. The diffusive motion of the interstitial cluster does not exhibit a preferential direction and involves frequent reversals of the moving direction, see Fig. 4. Additionally, the travelling interstitial triggers the spontaneous creation of further clusters at the lattice sites it touches. In contrast, location and particle

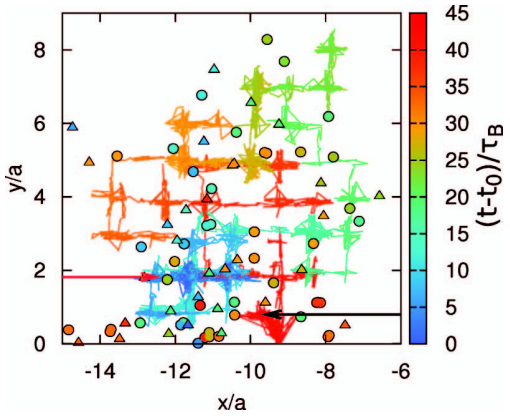

FIG. 4. Trajectory of a single B particle cluster from creation at $t = t_0$ (red arrow) to annihilation at $t = t_1$ (black arrow). The cluster emerges in the second stage of the deformation process, i.e., after a stable vacancy/interstitial pair was formed. The colorcode corresponds to the lifetime of the cluster. Circles (triangles) indicate the location of subsequent $A(B)$ cluster appearances within the lifetime of the travelling cluster.

constellation of the A particle cluster formed in this event are comparably stable.

The *third stage* of the deformation process starts with the formation of a larger cluster of A particles. Being unstable with respect to shear deformation, an elongated cluster of A particles poses a preferential site for a break as it allows for a local rearrangement of the crystal lattice on either side of the cluster. Once such an elongated cluster emerges, it quickly grows into a band spanning the entire system, which enables inhomogeneous, nonaffine particle displacements on the order of the lattice constant. This pattern of motion resembles a shear band[51,87–91] but may also exhibit vortical properties as reported in Refs. 52, 58, and 59. Thus, the crystal is globally rearranged and a less strained state is restored. Intriguingly, particles in the proximity of the break are rearranged during the cluster formation until eventually, the original S(AB) structure can be recovered for most particles, although typically, some topological defects remain. The deformation process depicted here is illustrated by computer simulation snapshots and a map of the cumulative nonaffine displacement in x-direction in Fig. 5. The spontaneous emergence of short-lived clusters can be observed at several positions as indicated by black crosses in Fig. 5 (right). Stable clusters emerge at $t/\tau_B \approx 50$ (white symbols), leading to structural defects which persist over many τ_B. The lifespan of stable clusters can be traced by straight lines in Fig. 5 (right). At $t/\tau_B \approx 100$, we observe a strongly heterogeneous behavior of the cumulative displacement in x-direction with respect to the y-position of particles: Above a certain y-position, particles undergo a pronounced nonaffine displacement in the direction of shear (bright area in Fig. 5 [right]). The nonaffine cumulative x-displacement of particles below this y-position is oppositely directed (dark area in Fig. 5 [right]). This pattern of nonaffine motion reflects the breakage of the crystal and is accompanied by the creation and annihilation of large numbers of clusters as the crystal rearranges. The location of the break coincides with the location of the first set of stable defects. Note that the orientation of the break does not necessarily collapse with the direction of shear. We observe a vertical breakage of the crystal with a similar probability.

Since the emergence of a stable vacancy/interstitial pair in the course of a thermal clustering event crucially influences the macroscopic breakage of the crystal, we thoroughly assess the properties of these events. In order to do so, we evaluate all events up to and including the first event which induces a cluster with a lifetime exceeding $0.5\tau_B$, which corresponds to a total number of 1002 recorded events. Thus, we focus on the onset of deformation in a strained crystalline state with no embedded topological defects, i.e., the *first stage* of the deformation process. We observe that within statistical accuracy, events are homogeneously distributed over the entire system area and no preferential location can be distinguished.

As the absolute strain γ grows, the probability of clustering events increases, see Fig. 6. We derive a measure for the crystal stability with respect to shear by monitoring the integrated probability for the creation of a long-lived cluster up to a given time. This magnitude is almost unity for times larger than $t/\tau_B \approx 80$, corresponding to an absolute strain of $\gamma \approx 0.08$. This reflects the fact that in all of our simulation

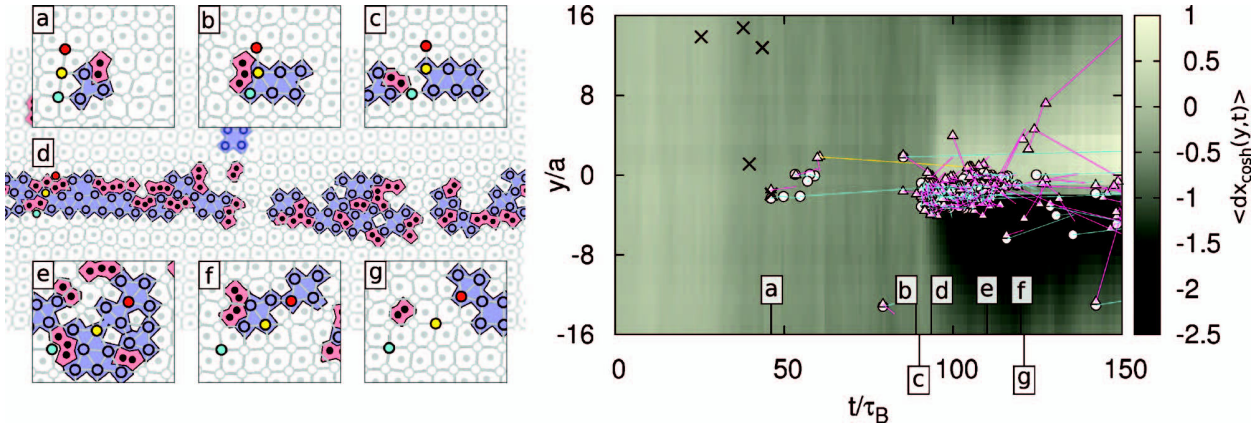

FIG. 5. (Left) Simulation snapshots illustrating the deformation process for the case $\alpha = 0°$. All snapshots originate from the same simulation run. Representation of particles and clusters corresponds to Fig. 2. As a guide to the eye, three individual A particles are shown in red, yellow, and cyan, respectively. (a) Creation of stable cluster pair, (b) extension of an A cluster in x-direction, (c) local rearrangement induced by interplay of A and B clusters, (d) formation of an extended, disordered cluster strip, and (e) crystal rearrangement on either side of the strip. (f) and (g) Restoration of S(AB) structure after nonaffine displacement on either side of strip (note shift of tagged particles). (Right) Map of cumulative displacement in x-direction in the co-sheared frame. The data were averaged over the initial x-coordinate. Colors are specified by the bar on the right. Black crosses indicate time and y-coordinate of short-lived clustering events. The appearance of $A(B)$ clusters with a lifetime $>0.5\tau_B$ is indicated with white full circles (triangles), straight cyan (pink) lines connect sites of creation and annihilation. A yellow line indicates the lifespan of the cluster traced in Fig. 4. Times corresponding to snapshots (a)–(g) in left panel are indicated on the time axis.

runs, a stable cluster has emerged up to this time, initiating the *second stage* of the crystal deformation.

On a microscopic level, the collective particle motion leading to clustering exhibits a vast variety of patterns. In order to assess the common microscopic mechanism governing these events, we monitor the average distribution of particles at the site of an event at three different times: $10^{-1}\tau_B$ before the event, $10^{-2}\tau_B$ before the event, and at the time of the event. The resulting density distributions of A and B particles are shown in Fig. 7. It is apparent from these distributions that events are permitted by a specific distortion of the unit cell, which originates from a superposition of two independent deformations. First, the unit cell is strained due to a shear deformation along the x-direction, which collapses with the lattice vector $\mathbf{a}_1$. Second, the unit cell is distorted by a further shear deformation of the A particles along the second lattice direction, $\mathbf{a}_2$. This corresponds to a collective sliding motion of the A particles on one side of the unit cell along the second crystal axis, while the remaining A particles collectively move into the opposite direction.

Following this observation, we derive the average A particle positions from the density distributions depicted in

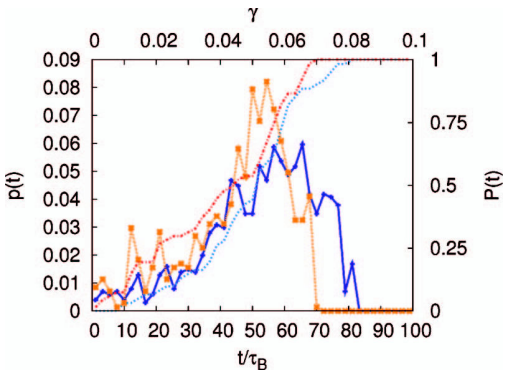

FIG. 6. Relative probability $p(t)$ for an event to occur at time t for $\alpha = 0°$ (blue solid line) and $\alpha = 45°$ (yellow dashed line). The cumulative probability $P(t)$ for the appearance of stable defect up to the time t is included for $\alpha = 0°$ (light blue dashed line) and $\alpha = 45°$ (red dashed line). For comparison, the absolute strain is given at the upper horizontal axis. The evaluation is based on a total number of 1002 (706) recorded events for $\alpha = 0°$ (45°).

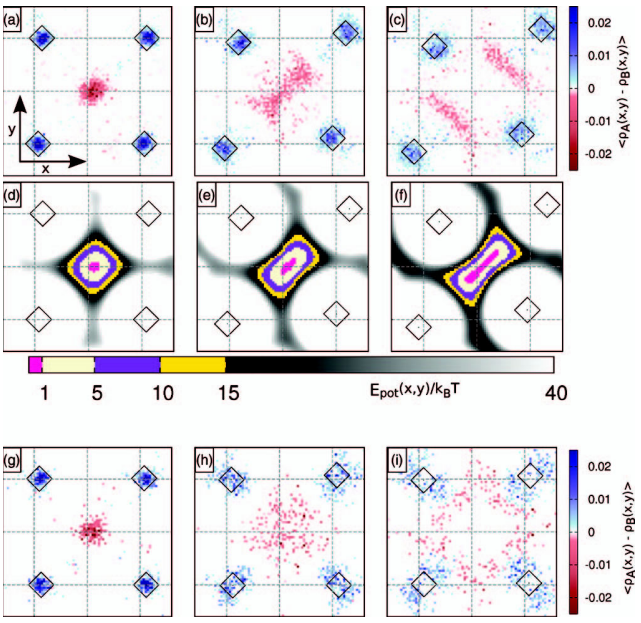

FIG. 7. $\alpha = 0°$. (a)–(c) Averaged densities $\langle\rho_A\rangle$, $\langle\rho_B\rangle$ of A and B particles at the site of an event at t_0 for times (a) $t - t_0 = -0.1\tau_B$, (b) $t - t_0 = -0.01\tau_B$, (c) $t - t_0 = 0$. Colors correspond to $\langle\rho_A(x, y)\rangle - \langle\rho_B(x, y)\rangle$ and are specified by the bar on the right. Diamonds indicate the average position of A particles. (d)–(f) Potential energy of a B particle in the vicinity of A-particles located at the average positions in situations (a)–(c). Colors are specified by the bar at the bottom. Potential energy is given with respect to the mean position of the B particle. (g)–(i) Averaged densities preceding a cluster creation when the crystal is heated to $\Gamma = 37$ and no shear flow is imposed ($\dot{\gamma}\tau_B = 0$).

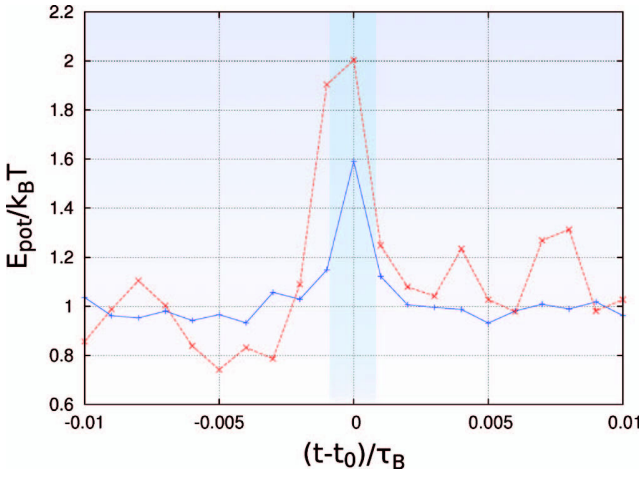

FIG. 8. Potential energy of the trigger particle with respect to the closest energy minimum for an event at $t = t_0$ (highlighted region) for $\alpha = 0°$. The blue solid curve corresponds to the average over all temporary events while the red dashed curve represents the average over all persistent events.

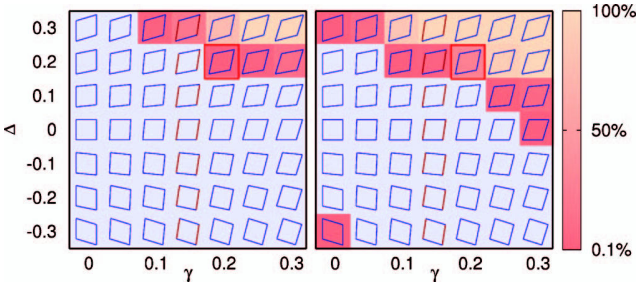

FIG. 9. Reference simulation for $\alpha = 0°$, where a B particle is initially trapped in a distorted unit cell formed by four A particles, see text. The distortion is specified by γ (shear deformation) and Δ (deflection along the lattice vector $\mathbf{a_2}$, highlighted in dark red in the central column). Resulting unit cells are shown and fields are colorcoded according to the escape probability of a B particle within a runtime of $1\,\tau_B$ (left) or $1000\,\tau_B$ (right), based on 1000 samples per parameter combination. Escape probabilities below 0.1% are shown in light blue. The parameter combination matching the average particle positions in Fig. 7(c) is framed in red.

Fig. 7 (top) and map the potential energy landscape encountered by a single B particle in the vicinity of four A particles at the specified positions, see Fig. 7 (middle). In the reference state at $10^{-1}\tau_B$ before the event, the average unit cell is only slightly sheared. There is a nearly quadratic energy well in the center of the unit cell to which the B particle is confined. Due to the subsequent deformation of the unit cell, the size of this potential energy well is reduced as it assumes a thin, tilted shape. Consequently, the B particle is confined to a diagonally elongated region at $10^{-2}\tau_B$ before the event. In the following timestep, only a narrow potential energy well remains inside the unit cell due to the further distortion of the unit cell. After the previous diagonal deflection of the B particle, it is now pushed away from the center as the local energy minimum is displaced along four possible pathways.

From this shifted position, the B particle may escape the unit cell due to thermal motion. To verify the thermal activation of this event, we calculate the potential energy of the B particle with respect to the nearest potential energy minimum. Indeed, the occurrence of an event is accompanied by a distinct peak of the potential energy on the order of $\approx 2k_BT$. Furthermore, we observe that the creation of a persistent cluster is related to a significantly larger peak in the potential energy of the trigger particle than the creation of a temporary cluster, see Fig. 8.

Thus, the investigation of particle density profiles at the location of events implies an intuitive picture for the formation of clusters from the strained crystalline state, which is permitted by two independent deformations of the unit cell: The global shear deformation and an aligned sliding motion of A particles along the lattice direction $\mathbf{a_2}$, which does not collapse with the direction of shear. In order to verify this explanation, we perform a set of reference simulations in which a single B particle is placed in a distorted unit cell of four A particles. The distortion of the unit cell is expressed by the two independent parameters γ and Δ: The parameter γ corresponds to the unit cell strain in the direction of shear, while Δ quantifies the aligned deflection of the A particles along the lattice direction $\mathbf{a_2}$, see Fig. 9. For each parameter combination, the B particle trajectory is tracked for $1\tau_B$ while the A particles remain pinned to their distorted lattice positions. Each parameter combination is sampled with 1000 runs. Afterwards, we determine the ratio of runs in which the B particle escaped the unit cell. Our results are shown in Fig. 9. We find that, starting from a strained state, an additional deflection of the A particles indeed leads to an increased probability for the B particle to escape the unit cell. The parameter combination of γ and Δ which best matches the average particle positions derived from the A particle density distribution is highlighted in Fig. 9. In fact, this point in the $\gamma - \Delta$ plane coincides with the crossover from zero to a finite value of the escape probability of the B particle. This crossover is persistent if we extend the runtime of the simulation to $1000\tau_B$, as shown in Fig. 9.

B. Shear unaligned with lattice direction

In order to assess the dependence of the shear response on the direction of shear flow with respect to the crystal orientation, we repeat the analysis for the case $\alpha = 45°$.

In comparison to $\alpha = 0°$, we notice a more pronounced increase of the event probability with increasing strain. Likewise, the integrated probability for the creation of a stable cluster up to a given time reaches unity at a time $t/\tau_B \approx 70$ ($\gamma \approx 0.07$), see Fig. 6. This points to a reduced stability of the crystal with respect to shear deformation when the unit cell is rotated with respect to the direction of shear.

Furthermore, we analyze the particle interplay leading to an event for $\alpha = 45°$. Our results are shown in Fig. 10. As opposed to the previous case, the averaged density distributions do not point to a single deformation mode but rather depict the superposition of two distinct deformation modes, which correspond to sliding motions of the A particles along either lattice vector, $\mathbf{a_1}$ or $\mathbf{a_2}$. Since neither of the two lattice directions collapses with the direction of shear, sliding motions along both directions distort the unit cell in an equivalent way. To support this interpretation, shifted unit cells are included in Fig. 10, which are deformed according to either of the two

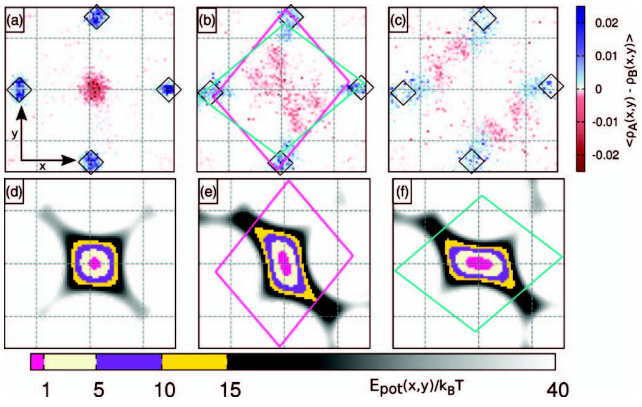

FIG. 10. $\alpha = 45°$. (a)–(c) Averaged local densities $\langle\rho_A\rangle$, $\langle\rho_B\rangle$ of A and B particles at the site of an event at t_0 for times (a) $t - t_0 = -0.1\tau_B$, (b) $t - t_0 = -0.01\tau_B$, (c) $t - t_0 = 0$. Colors correspond to $\langle\rho_A(x, y)\rangle - \langle\rho_B(x, y)\rangle$ and are specified by the bar on the right. Diamonds indicate the average position of A particles. For clarity, two distinct deformations of the unit cell are included in panel (b). (d) Potential energy of a B particle in the vicinity of A-particles located at the average positions in situation (a). Panels (e) and (f) correspond to the unit cell outlines shown in (b). Colors are specified by the bar at the bottom. Potential energy is given with respect to the mean position of the B particle.

modes. The potential energy landscape exhibits two pathways for the B particle for each deformation mode. The superposition of these pathways can be recovered in the average density distribution of B particles, which exhibits a cross-shaped maximum at $10^{-2}\tau_B$ before the event.

As with the case $\alpha = 0°$, we perform additional simulations to sample the escape probability of a single B particle enclosed in a distorted unit cell, where the distortion is expressed by the parameters γ and Δ, see Fig. 11. The parameter combinations corresponding to the distorted unit cells shown in Fig. 10 are highlighted in the diagram and are close to the crossover to a finite escape probability.

C. Comparison with different deformation scenarios

We compare the pattern of defect formation observed in the sheared binary crystal to the creation of defects when the

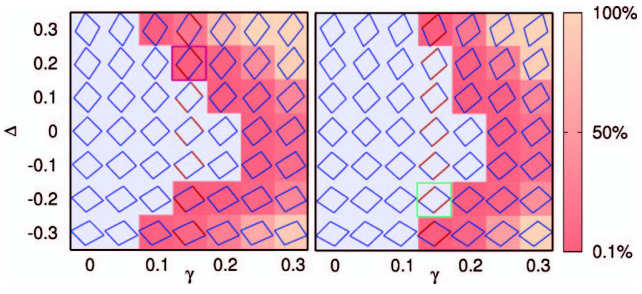

FIG. 11. Escape probability of a B particle from a distorted unit cell for $\alpha = 45°$. The distortion is specified by γ (shear deformation) and Δ (deflection along the lattice vectors $\mathbf{a_1}$ [left] or $\mathbf{a_2}$ [right], highlighted in dark red in the central column). Resulting unit cells are shown and fields are colorcoded according to the escape probability of a B particle within a runtime of $1\,\tau_B$, based on 1000 samples per parameter combination. Escape probabilities below 0.1% are shown in light blue. The parameter combinations matching the cells shown in Fig. 7(b) are framed.

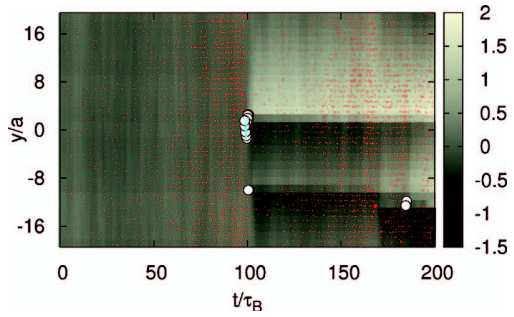

FIG. 12. Typical deformation process for the one-component crystal under shear. Colorcode corresponds to cumulative displacement in x-direction in the co-sheared frame. White circles indicate clusters with a lifetime above $0.1\tau_B$, straight cyan lines connect sites of creation and annihilation. Short-lived clusters with a lifetime below $0.1\tau_B$ are indicated by red dots.

crystal is heated to $\Gamma = 37$ and no shear flow is imposed ($\dot\gamma = 0$). Our results are included in Fig. 7 and indicate a qualitatively different mechanism with respect to the individual particle motion. Here, the crystalline structure cannot be attributed to an aligned deflection of the A-particles but rather stems from a diffusion of the particles away from the unit cell center.

Furthermore, we qualitatively compare the deformation process of the sheared binary crystal to the shear deformation of a one-component crystal near melting. The crystal is constituted by $N = 2304$ dipolar particles of species A which are arranged in a triangular lattice spanning the simulation area $L_x \times L_y = 48a \times 41.57a$. The inverse temperature is set to $\Gamma = 20$ and the shear rate is fixed at $\dot\gamma = 10^{-3}$ as before. For the one-component crystal, the structural rearrangement needed to release the strain is enabled by the spontaneous creation of (isolated) dislocation pairs along the tearing direction. As opposed to the binary crystal, these topological defects can be spontaneously created to accommodate rearrangements of the adjacent particles. Thus, the onset of plasticity is not determined by the presence of persistent topological defects, as is the case with the binary crystal. Similarly, the defects are quickly annihilated once the crystal rearranged into a less strained configuration. Thus, the defects observed

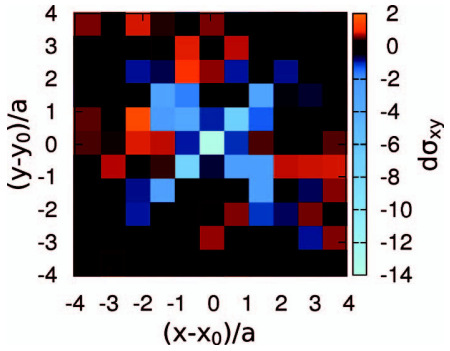

FIG. 13. Averaged stress signature of events recorded for $\alpha = 0°$ and $\alpha = 45°$. The colorcode corresponds to the stress increase with respect to the previous configuration for particles at a given distance to the trigger particle at x_0,y_0. The fourfold pattern qualitatively corresponds to recent findings for polydisperse hard spheres under shear[66] and flowing emulsions near jamming.[67]

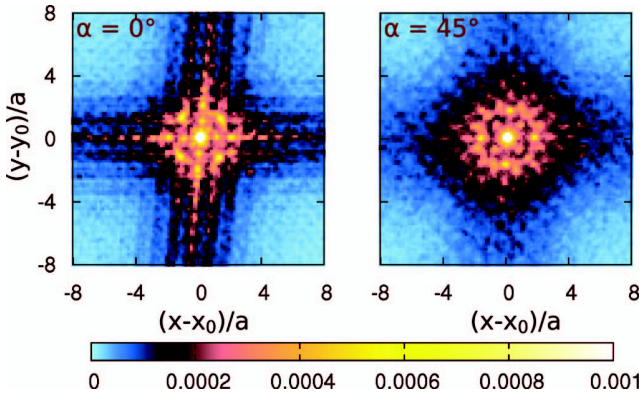

FIG. 14. Spatial correlation of A cluster appearances for $\alpha = 0°$ (left) and $\alpha = 45°$ (right). The colorcode corresponds to the probability for a cluster to emerge at a particular relative position $x - x_0$, $y - y_0$ with respect to a previous cluster creation at x_0, y_0. Colors are specified by the bar at the bottom.

in the sheared one-component crystal are mostly short-lived with a lifetime well below $0.1\tau_B$ and the deformation of the crystal does not entail an extended amorphous region. We observe that defects appear more frequently than in the strained binary crystal. For a qualitative comparison, we devise a simplified cluster criterion for the one-component crystal, where neighboring particles form a cluster if they each have either five or seven nearest neighbors, thus distorting the sixfold symmetry of the ideal lattice. Thereby, we cover isolated and bound dislocations as well as entangled chains. Figure 12 depicts the creation and annihilation of clusters.

Recent studies on the plastic deformation of amorphous media have explicitly demonstrated a characteristic stress signature and spatial correlation of plastic events,[65–67,92] corresponding to earlier theoretical predictions.[93] Encouraged by these findings, we assess the local stress signature of cluster creation events, which play the role of plastic events in the breaking of the S(AB) crystal. Intriguingly, our results are in qualitative agreement with the stress signature observed in an amorphous system of polydisperse hard spheres under shear[66] and in flowing emulsions near jamming,[67] see Fig. 13. Additionally, we probe the spatial correlation of cluster appearances and recover a non-vanishing spatial correlation along two distinct directions, which are aligned parallel and perpendicular to the direction of shear flow, respectively, see Fig. 14. This finding is in agreement with the observation that the S(AB) crystal may develop cracks in the lateral or vertical direction, as discussed above. A similar spatial correlation of defect creation sites was not observed for the reference case of a sheared one-component crystal.

VI. CONCLUSIONS

We have analyzed the shear-induced breaking of a thermal binary model crystal on the particle-scale level using Brownian dynamics computer simulations. Thus, we have established that the macroscopic breakage of the crystal originates in the spontaneous creation of defects in the initially defect-free crystal. The defects are visualized by a cluster criterion. Our observations suggest that the emergence of defects is induced by a characteristic hierarchical interplay of the two particle species. In the strained crystal, aligned fluctuations of the more strongly interacting A particles along the strained lattice directions distort the potential energy landscape and induce plastic events, where the B particles are pushed out of the unit cell. The likelihood of these events is increased if the shear direction is not aligned with the crystal orientation. Further plastic events are triggered by vacancy diffusion until eventually, small clusters merge into an extended disordered region and initiate the macroscopic breakage of the crystal, during which pronounced nonaffine displacements are observed. This breaking scenario is in distinct contrast to the shear response of a one-component crystal near melting, where stress is released via the spontaneous creation and annihilation of dislocation pairs without spatially extended or persistent regions of structural disorder. Furthermore, on a microscopic level, the breaking of the binary crystal under shear can be clearly distinguished from the melting of the crystal in the absence of shear.

Our observations suggest that various properties which are intrinsic to the plasticity of amorphous materials can be found in the breaking of a binary crystal, where the escape of B particles from their cages induces a local loss of structure and allows for nonaffine rearrangements in the manner of an amorphous material. These properties include a fourfold stress signature of plastic events and a distinct, anisotropic spatial correlation of plastic events with respect to the shear direction. Thus, our results shed new light on the study of solid plasticity, where crystalline and amorphous solids pose qualitatively different scenarios. Our results imply that in the case of a multicomponent crystal — even in the simple case of a binary crystal — this qualitative difference does not fully apply due to a local amorphization of the crystal in the breaking zone.

Our predictions can be verified in binary suspensions of superparamagnetic colloidal particles at a pending air-water interface in an external magnetic field.[10,79,80,94] The shear can be imposed by a laser beam. For the future, one should explore more situations of shear-induced breaking. In particular, the case of small damping will be interesting as this is relevant for the melting of a dusty plasma crystal under shear (have a look at our book for references). Moreover, more interaction asymmetries, composition ratios and model potentials need to be explored. Last, the case of three spatial dimensions would be interesting where a wealth of binary colloidal crystals are possible.[95]

ACKNOWLEDGMENTS

We thank J. F. Brady, S. Mandal, J. Horbach, and P. Chaudhuri for valuable advice. We thank C. V. Achim for providing a computer code. This work was supported by the SFF from the HHU.

[1]F. Brau, "Tearing of thin sheets: Cracks interacting through an elastic ridge," e-print arXiv:1409.0450 (unpublished).
[2]N. D. Alexopoulos, E. Miklis, A. Stylianos, and D. P. Myriounis, Int. J. Fatigue **56**, 95 (2013).
[3]S.-B. Shim, K. Ahn, J. C. Seferis, A. J. Berg, and W. Hudson, J. Adv. Mater. **26**, 48 (1995).

[4]X. Guo, L. C. Liang, and S. A. Goldstein, J. Biomech. Eng. **120**, 112 (1998).
[5]A. R. Najafi, A. R. Arshi, M. R. Eslami, S. Fariborz, and M. H. Moeninzadeh, J. Biomech. **40**, 2788 (2007).
[6]A. V. Ivlev, H. Löwen, G. E. Morfill, and C. P. Royall, *Complex Plasmas and Colloidal Dispersions: Particle-Resolved Studies of Classical Liquids and Solids*, Series in Soft Condensed Matter: Volume 5 (World Scientific, 2012).
[7]J. Baumgartl, R. P. A. Dullens, M. Dijkstra, R. Roth, and C. Bechinger, Phys. Rev. Lett. **98**, 198303 (2007).
[8]D. Heinrich, A. R. Goñi, A. Smessaert, S. H. L. Klapp, L. M. C. Cerioni, T. M. Osán, D. J. Pusiol, and C. Thomsen, Phys. Rev. Lett. **106**, 208301 (2011).
[9]B. J. Ackerson and N. A. Clark, Phys. Rev. Lett. **46**, 123 (1981).
[10]P. Keim, G. Maret, and H. H. von Grünberg, Phys. Rev. E **75**, 031402 (2007).
[11]R. P. A. Dullens and C. Bechinger, Phys. Rev. Lett. **107**, 138301 (2011).
[12]S. J. Gerbode, U. Agarwal, D. C. Ong, C. M. Liddell, F. Escobedo, and I. Cohen, Phys. Rev. Lett. **105**, 078301 (2010).
[13]J. M. McMullan and N. J. Wagner, Soft Matter **6**, 5443 (2010).
[14]R. Pasquino, F. Snijker, N. Grizzuti, and J. Vermant, Langmuir **26**, 3016 (2010).
[15]E. Villanova-Vidal, T. Palberg, H. J. Schöpe, and H. Löwen, Philos. Mag. **89**, 1695 (2009).
[16]J. Zanghellini, P. Keim, and H. H. von Grünberg, J. Phys.: Condens. Matter **17**, S3579 (2005).
[17]M. Medebach and T. Palberg, Collods Surf. A **222**, 175 (2003).
[18]J. Kaldasch, J. Laven, and H. N. Stein, J. Rheol. **42**, 1285 (1998).
[19]T. Palberg and K. Streicher, Nature **367**, 51 (1994).
[20]P. Schall, D. A. Weitz, and F. Spaepen, Science **318**, 1895 (2007).
[21]S. Deutschländer, K. Franzrahe, B. Heinze, P. Henseler, P. Keim, N. Schwierz, U. Siems, P. Virnau, D. Wilms, K. Binder, G. Maret, and P. Nielaba, Eur. Phys. J.: Spec. Top. **222**, 2973 (2013).
[22]P. Henseler, A. Erbe, M. Koeppl, P. Leiderer, and P. Nielaba, Phys. Rev. E **81**, 041402 (2010).
[23]S. Butler and P. Harrowell, J. Chem. Phys. **103**, 4653 (1995).
[24]D. Wilms, P. Virnau, and K. Binder, Mol. Phys. **111**, 3418 (2013).
[25]D. Wilms, P. Virnau, S. Sengupta, and K. Binder, Phys. Rev. E **85**, 061406 (2012).
[26]S. Jäger, H. Stark, and S. H. L. Klapp, J. Phys.: Condens. Matter **25**, 195104 (2013).
[27]F. Smallenburg, L. Filion, M. Marechal, and M. Dijkstra, Proc. Natl. Acad. Sci. U.S.A. **109**, 17886 (2012).
[28]C. Kreuter, U. Siems, P. Nielaba, P. Leiderer, and A. Erbe, Eur. Phys. J.: Spec. Top. **222**, 2923 (2013).
[29]K. Franzrahe, P. Nielaba, A. Ricci, K. Binder, S. Sengupta, P. Keim, and G. Maret, J. Phys.: Condens. Matter **20**, 404218 (2008).
[30]T. A. Vezirov and S. H. L. Klapp, Phys. Rev. E **88**, 052307 (2013).
[31]T. Kruppa, T. Neuhaus, R. Messina, and H. Löwen, J. Chem. Phys. **136**, 134106 (2012).
[32]D. Derks, Y. L. Wu, A. van Blaaderen, and A. Imhof, Soft Matter **5**, 1060 (2009).
[33]M.-C. Miguel, A. Vespignani, S. Zapperl, J. Weiss, and J.-R. Grasso, Nature **410**, 667 (2001).
[34]D. M. Dimiduk, C. Woodward, R. LeSar, and M. D. Uchic, Science **312**, 1188 (2006).
[35]V. Bulatov, F. Abraham, L. Kubin, B. Devincre, and S. Yip, Nature **391**, 669 (1998).
[36]B. van der Meer, W. Qi, R. Fokkink, J. van der Gucht, M. Dijkstra, and J. Sprakel, Proc. Natl. Acad. Sci. USA **111**, 15356 (2014).
[37]H. Shiba and A. Onuki, Phys. Rev. E **81**, 051501 (2010).
[38]T. Hamanaka, H. Shiba, and A. Onuki, Phys. Rev. E **77**, 042501 (2008).
[39]V. Fallah, J. Stolle, N. Ofori-Opoku, S. Esmaeili, and N. Provatas, Phys. Rev. B **86**, 134112 (2012).
[40]V. Fallah, A. Korinek, N. Ofori-Opoku, N. Provatas, and S. Esmaeili, Acta Mater. **61**, 6372 (2013).
[41]L. Rougier, A. Jacot, C.-A. Gandin, P. Di Napoli, P.-Y. Théry, D. Ponsen, and V. Jaquet, Acta Mater. **61**, 6396 (2013).
[42]F. Sun, J. Y. Zhang, M. Marteleur, T. Gloriant, P. Vermaut, D. Laillé, P. Castany, C. Curfs, P. J. Jacues, and F. Prima, Acta Mater. **61**, 6406 (2013).
[43]S. M. Hafez Haghighat, R. Schäublin, and D. Raabe, Acta Mater. **64**, 24 (2014).
[44]Y. Mishin, J. A. Warren, R. F. Sekerka, and W. J. Boettinger, Phys. Rev. B. **88**, 184303 (2013).
[45]H. Matsumoto, Y. Koizumi, T. Ohashi, B.-S. Lee, Y. Li, and A. Chiba, Acta Mater. **64**, 1 (2014).
[46]T. Iwai, J. Phys. Soc. Jpn. **68**, 3717 (1999).
[47]H.-C. Yu, D.-H. Yeon, A. Van der Ven, and K. Thornton, Acta Mater. **55**, 6690 (2007).
[48]D. J. K. Ross and R. M. Bustin, Mar. Pet. Geol. **26**, 916 (2009).
[49]H. Muto, K. N. Nunome, K. Toriyama, and M. Iwasaki, J. Phys. Chem. **93**, 4898 (1989).
[50]F. Varnik, L. Bocquet, and J.-L. Barrat, J. Chem. Phys. **120**, 2788 (2004).
[51]Y. Shi and M. L. Falk, Phys. Rev. Lett. **95**, 095502 (2005).
[52]C. E. Maloney and A. Lemaître, Phys. Rev. E **74**, 016118 (2006).
[53]J. Zausch, J. Horbach, M. Laurati, S. U. Egelhaaf, J. M. Brader, T. Voigtmann, and M. Fuchs, J. Phys.: Condens. Matter **20**, 404210 (2008).
[54]J. Zausch and J. Horbach, Europhys. Lett. **88**, 60001 (2009).
[55]T. Sentjabrskaja, E. Babaliari, J. Hendricks, M. Laurati, G. Petekidis, and S. U. Egelhaaf, Soft Matter **9**, 4524 (2013).
[56]G. Picard, A. Ajdari, F. Lequeux, and L. Bocquet, Phys. Rev. E **71**, 010501 (2005).
[57]J.-C. Baret, D. Vandembroucq, and S. Roux, Phys. Rev. Lett. **89**, 195506 (2002).
[58]K. Maeda and S. Takeuchi, Philos. Mag. A **44**, 643 (1981).
[59]A. Tanguy, F. Leonforte, and J.-L. Barrat, Eur. Phys. J. E **20**, 355 (2006).
[60]M. L. Falk and J. S. Langer, Phys. Rev. E **57**, 7192 (1998).
[61]C. Yang and L. I, Phys. Rev. E **89**, 041102(R) (2014).
[62]E. Tondl, M. Ramsay, P. Harrowell, and A. Widmer-Cooper, J. Chem. Phys. **140**, 104503 (2014).
[63]D. Chen, K. W. Desmond, and E. R. Weeks, Soft Matter **8**, 10486 (2012).
[64]K. W. Desmond, P. J. Young, D. Chen, and E. R. Weeks, Soft Matter **9**, 3424 (2013).
[65]F. Varnik, S. Mandal, V. Chikkadi, D. Denisov, P. Olsson, D. Vågberg, D. Raabe, and P. Schall, Phys. Rev. E **89**, 040301 (2014).
[66]S. Mandal, private communication (2014).
[67]K. W. Desmond and E. R. Weeks, "Experimental measurements of stress redistribution in flowing emulsions," e-print arXiv:1306.0269 (unpublished).
[68]J. Boberski, M. R. Shaebani, and D. E. Wolf, Europhys. Lett. **108**, 44002 (2014).
[69]M. Kollmann, R. Hund, B. Rinn, G. Nägele, K. Zahn, H. König, G. Maret, R. Klein, and J. K. G. Dhont, Europhys. Lett. **58**, 919 (2002).
[70]N. Hoffmann, F. Ebert, C. N. Likos, H. Löwen, G. Maret, R. Klein, and J. K. G. Dhont, Phys. Rev. Lett. **97**, 078301 (2006).
[71]L. Assoud, F. Ebert, P. Keim, R. Messina, G. Maret, and H. Löwen, Phys. Rev. Lett. **102**, 238301 (2009).
[72]L. Assoud, F. Ebert, P. Keim, R. Messina, G. Maret, and H. Löwen, J. Phys.: Condens. Matter. **21**, 464114 (2009).
[73]M. Mukherjee, P. Mishra, and H. Löwen, J. Phys.: Condens. Matter **26**, 465101 (2014).
[74]L. Assoud, R. Messina, and H. Löwen, Mol. Phys. **109**, 1385 (2011).
[75]L. Assoud, R. Messina, and H. Löwen, Europhys. Lett. **80**, 48001 (2007).
[76]G. K. Kaufman, M. Reches, S. W. Thomas, J. Feng, B. F. Shaw, and G. M. Whitesides, Appl. Phys. Lett. **94**, 044102 (2009).
[77]L. Assoud, R. Messina, and H. Löwen, Europhys. Lett. **89**, 36001 (2010).
[78]L. Assoud, R. Messina, and H. Löwen, J. Chem. Phys. **129**, 164511 (2008).
[79]K. Zahn, R. Lenke, and G. Maret, Phys. Rev. Lett. **82**, 2721 (1999).
[80]K. Zahn and G. Maret, Phys. Rev. Lett. **85**, 3656 (2000).
[81]S. Deutschländer, T. Horn, H. Löwen, G. Maret, and P. Keim, Phys. Rev. Lett. **111**, 098301 (2013).
[82]T. Horn, S. Deutschländer, H. Löwen, G. Maret, and P. Keim, Phys. Rev. E **88**, 062305 (2013).
[83]The value $\Gamma = 44$ was established as the liquid-solid coexistence value of the model system at hand in a previous simulation study by the authors.
[84]A. W. Lees and S. F. Edwards, J. Phys. C: Solid State Phys. **5**, 1921 (1972).
[85]The critical distance is set to $0.62a$ but may be varied without qualitatively affecting our results.
[86]D. M. Heyes, P. J. Mitchell, P. B. Visscher, and J. R. Melrose, J. Chem. Soc. Faraday Trans. **90**, 1133 (1994).
[87]F. Varnik, L. Bocquet, J.-L. Barrat, and L. Berthier, Phys. Rev. Lett. **90**, 095702 (2003).
[88]J. Park, Y. Shibutani, M. Wakeda, and S. Ogata, Mater. Trans. **48**, 1001 (2007).
[89]P. Schall and M. van Hecke, Annu. Rev. Fluid Mech. **42**, 67 (2010).

[90]R. L. Moorcroft, M. E. Cates, and S. M. Fielding, Phys. Rev. Lett. **106**, 055502 (2011).
[91]P. Chaudhuri, L. Berthier, and L. Bocquet, Phys. Rev. E **85**, 021503 (2012).
[92]S. Mandal, V. Chikkadi, B. Nienhuis, D. Raabe, P. Schall, and F. Varnik, Phys. Rev. E **88**, 022129 (2013).
[93]A. S. Argon, Acta Metall. **27**, 47 (1979).
[94]H. H. von Grünberg, P. Keim, K. Zahn, and G. Maret, Phys. Rev. Lett. **93**, 255703 (2004).
[95]P. Bartlett, R. H. Ottewill, and P. N. Pusey, Phys. Rev. Lett. **68**, 3801 (1992).

4) How does a thermal binary crystal break under shear?	
Journal	The Journal of Chemical Physics
Impact Factor	3.122
Authorship	1st author
Contribution	90%
	Computer simulations and data analysis

Acknowledgment

At this point, I wish to express my gratitude to those individuals who have contributed to this dissertation through their personal support and council. In particular, sincere thanks go to my doctoral adviser Prof. Dr. Hartmut Löwen, who provided invaluable guidance and advice throughout my doctoral research. I wish to thank Prof. Dr. Jürgen Horbach, who, acting as second examiner of this dissertation, followed my research attentively and contributed pivotal insight on numerous occasions. I also wish to express my thanks for the valueable comments and advice I received from Dr. Michael Schmiedeberg, as well as for his willingness to provide mentorship during my doctorate.
To a substantial degree, the results presented in this work reflect the fruitful collaboration I enjoyed with Sven Deutschländer, Dr. Peter Keim and Prof. Dr. Georg Maret at the University of Konstanz. My special thanks go to them.
I wish to thank Prof. Dr. John F. Brady for providing most helpful advice on Brownian dynamics computer simulations. Furthermore, I thank Dr. Pinaki Chaudhuri as well as Dr. Suvendu Mandal for offering their insights on sheared amorphous suspensions.
I wish to thank my colleagues at the *Insitute of Theoretical Physics II: Soft Matter* for their helpfulness and their contribution to my work through thoughtful remarks and suggestions. In particular, I like to thank Dr. Cristian V. Achim, Dr. Erdal C. Oğuz, Dr. Tim Neuhaus and Aleksandar Mijailović for helpful discussions and comments on my research. I thank Dr. Andreas Kaiser, Urs Zimmermann and Jörg Bartnick for sharing thoughts and hints on the pitfalls of technology we encountered during our work. For his suggestions concerning the design of computer programs and his sustained technical support, I wish to thank Joachim Wenk. For their lasting support in resolving buerocratic barriers, I like to thank Brigitte Schumann-Kemp and Karin Wildhagen.

All of my colleagues I wish to thank for the bonds of friendship that have formed over the past years. For their lasting companionship during our studies, my profound thanks go to Borge ten Hagen, Julian Bialké and Matthias Kohl.

I wish to express my thanks and gratitude to my wife Johanna, who lovingly accompanied me, shared in the joys and challenges I encountered during the time of my dissertation and supplied me with the strength to succeed.

Eidesstattliche Versicherung

Ich versichere an Eides Statt, dass die Dissertation von mir selbständig und ohne unzulässige fremde Hilfe unter Beachtung der Grundsätze zur Sicherung guter wissenschaftlicher Praxis an der Heinrich-Heine-Universität Düsseldorf erstellt worden ist.

Düsseldorf,